Hypersonic Control Effectors

Jack Hillyer

Supervisor: Dr L Doherty
Prof. M McGilvray
Prof M Bacic

Department of Engineering
University of Oxford

This dissertation is submitted for the degree of
Doctor of Philosophy

Wolfson College

July 2025

Acknowledgements

First and foremost, I would like to thank my supervisors: Dr Luke Doherty, Prof Matthew McGilvray and Prof Marko Bacic. Luke, even your perfectionist nature should be happy with the quality of supervision you've provided - you have truly been incredible. Thank you for all the patience you've shown me, the trust you have demonstrated and for forcing me to pull my head out of the engineering and focus on the science - without you, I certainly could not have completed a DPhil. Matt, thanks for always being keen to discuss the research direction, for sorting the funding for the DPhil, and for putting up with me doing my utmost to wind you up. Marko, thanks for all of the advice during control board development and your input regarding dynamic aerodynamics.

Thanks also to DSTL for funding this PhD and to Trevor Birch for his technical contributions to the work. Additionally, thank you to AWE Plc for measurement of the cone mass properties and for technical advice.

Moving on to the incredible Hypersonics tunnel team over the past few years: Tristan Crumpton, Christopher Wheeler and Christopher Hambidge. Tristan - thanks for all the support, innuendo, and most significantly - some excellent pumping. You have an absolute gift for making stressful test campaigns a joy, whether it's with a joke, an anecdote or just your non-stop enthusiasm, you always knew how to keep us all going. Wheels - it's been an absolute pleasure to work with you, thanks for all of the witty remarks, setting up Schlieren for me and driving me up the wall with your coding (amongst countless other things). Finally Hambidge, thanks for everything - consistent support across the DPhil, the great chats at the pub and for always keeping me and the lab to a high standard. Thanks in particular for dropping everything to operate HDT and ensure my final campaign was smooth - this thesis would be significantly worse if not for you.

To my friends within the hypersonics group: thank you all for the good times. First and foremost, Big Will - Jack wouldn't have made it very far without Big Will - thanks for your endless patience, all the tea breaks and for being the best sidequest partner I could have asked for. Alex - Morning! - thanks for all the laughs and for generally making the grad office/control room a great place to be. Joe, in our first year, you shook my hand and told me "we're going to make it", and I'm glad to say as I write this now that you were right.

Thanks for the constant affirmations, hugs and good times across the DPhil. Raggy, thanks for all of the emotional support during tough times and for tolerating/supporting my silliness - I've really enjoyed how our friendship has developed. Andy - thanks for all of the guidance you gave over the course of the DPhil, and particularly for coming in to the lab to give me advice on hammer hits the day after you got back from holiday. Hassan, thank you for your excellent tutoring in my undergrad and ultimately starting me down this path. To the other members of the lab across the years - Seb, Pete, Rowland, Marc, Imran, Eric H, Suria, PK, Anthony, Omar, Maïlys, Andrew C, Laurent, Oli, Liam P, Baby Tom - thank you all for making the lab such an enjoyable place to be.

I'd also like to thank the incredible admin staff here at Southwell - Anna Erillo, Alex Weaving and Kathryn Scott. Thank you all for your sheer competence and for generally being willing to go to war for all of us - whether that's with suppliers or the engineering department itself! Most importantly though, thanks for all the times we partied together - our "feral" nights at the cow and creek and the staff party at the Ashmolean are some of my fondest memories of the DPhil.

Thanks also to the technical staff at Southwell - Jason, Greg, Leo, Dave, Duncan, Andreea, Gabriel, Craig, Roger - thank you for the incredible work you all did and continue to do. Thanks in particular to Hal Surtell for his excellent work on the various iterations of the PALM pipework across the DPhil.

To my friends outside the lab - thanks for the endless support. Bingham - your monthly phone calls have kept me sane, thanks for all the emotional support. Gouck, thanks for always being the funniest person in the room and for being such a joy to be around - you truly are an incredible friend. To Bruford[1]: thanks for all of your advice on my many electronics problems, for always being a supportive and fantastic friend and for your contributions to the greatest work playlist ever created. Pedro - thanks for all of the good times these last few years, I will always laugh when I think back to our attempt at a beef wellington! Maria, thanks for always supporting me and listening to my complaints. To the friends from 113 - Corrie, Kiah, Tina, Tis, Sam, Nathan, Emily - thanks for the good times and for making covid lockdown(s) bearable, even if I am convinced that some of you are criminally insane.

Finally, I'd like to thank my family. To my parents, Lynda and Peter, thank you for the endless love and support you have given me, I truly couldn't have done any of this without you. To my sisters Laura and Jessica, thank you for always listening. Finally to my brother Dr James Hillyer, the man who inspired me to do a DPhil, thank you for always being there for me, whether that's to give advice, go for a beer or to help me move house, I've always been able to depend on you.

[1]We love the battery!

Abstract

In the design of any flight vehicle, preliminary concepts are assessed based on key performance indices. For hypersonic vehicles (except re-entry capsules), two of the most important indices are manoeuvrability and controllability, both of which are functions of the control effectiveness - how much control moment the control effectors can produce. The most common control effectors in the continuum regime are aerodynamic control surfaces, but shock waves and potential flow separation regions arising from their deflection exacerbate the extreme aerothermal loading characteristic of hypersonic flight. Ablative materials, which chemically react with the flow to absorb its energy, are commonly employed as protection for the control effectors, though this comes at the expense of outer mold line changes, typically manifesting as regression of leading edges (blunting) and development of surface roughness. Despite the common use of ablatives, and several flight demonstrations of control effector shape change, there has been no study investigating the effect of shape change on control effectiveness.

Control authority measurements in ground test facilities typically consist of a static model with the control effector at a fixed flap deflection and resultant forces measured with a force balance. These are typically performed with a resolution of 5 degrees in flap deflection, and control authority is linearly interpolated between test points. However, as demonstrated by the first flight failure of the X43-A, too coarse a resolution in flap deflection can miss non-linearities in control moment. Finer resolutions are not often used as a consequence of the costs associated with running ground tests.

This thesis seeks to improve the state-of-the-art for control effectiveness studies in hypersonic Ludwieg tunnels and investigate the effect of shape change on the control effectiveness of all moving wings. Improvements to the state-of-the-art, defined here as the number of test points (control effector deflections, attitudes) characterised in a single run, require test durations that are typically only achievable for hypersonic aerodynamic studies in blowdown facilities or large scale Ludwieg tunnels. For smaller scale Ludwieg tunnels, the available test time can be increased to match those in larger scale facilities by implementation of Extended Ludwieg Mode (ELM), a quasi-steady blowdown mode that produces constantly decreasing nozzle supply conditions. This thesis develops a new, steady blowdown mode of

operation, Plenum Augmented Ludwieg Mode (PALM), which requires the facility to feature a plenum and fast acting valve between the high pressure reservoir and the facility nozzle. At the expense of unit Reynolds number capability, operation in PALM allows for smaller scale facilities to match (or potentially exceed) the test times offered by large scale facilities operating in traditional Ludwieg mode without compromising on test flow steadiness. Both ELM and PALM have been demonstrated to increase the available test time in the Oxford High Density Tunnel (HDT) by a factor of 10, with increases by a factor of 25 possible with improved vacuum capability.

Improvements to the state-of-the-art for control effectiveness measurements are achieved using this extended test duration to 1) investigate the effect of nozzle supply pressure rise time on force balance natural frequency excitation and assess the suitability of a 6 Degree of Freedom Inertial Measurement Unit for acceleration compensation, 2) characterise multiple control effector deflections in a single test and 3) develop a free-to-roll model for continuous, low uncertainty, resolution of control effectiveness as a function of roll position. It is demonstrated that for Ludwieg Tunnels, addition of a plenum between the fast acting valve and the nozzle throat can reduce the magnitude of the startup loads models are subject to, and that the duration of the nozzle startup period, not the overall rise time of the facility nozzle supply trace, dictates which natural frequencies are excited. It is also demonstrated that 6 Degree of Freedom Inertial Measurement Unit's can be used for acceleration compensation, including use of differentiated gyroscope measurements for moment compensation. Excellent agreement was shown between tests performed with a constant wing deflection and those with multiple wing setpoints during the test. The free-to-roll technique leverages the inherently low aerodynamic damping characteristic of hypersonic vehicles, in combination with low reduced angular rates, to provide a low uncertainty measurement of the static aerodynamics in isolation of dynamic phenomena. This technique was validated against force balance data at zero degrees angle of attack and has demonstrated the ability to characterise multiple roll positions in a single test at angle of attack.

Finally, this thesis investigates the effect of shape change on control effectiveness. Experimental results from testing of a 150 mm base diameter, 10 degree half angle cone with all moving wings in the Oxford HDT, are presented. Two nosetips, with bluntness ratios of 1.7% and 17%, were tested, along with 6 variations of wing shape. At zero degrees angle of attack, it was found that increased nosetip bluntness ratio decreases the control effectiveness provided by all moving wings, owing to the increased thickness of the entropy layer and associated low total pressure zone. It was found that blunting of the leading edge of the all moving wing also resulted in a reduction in control effectiveness, though this effect was negligible in comparison with the effect of nosetip blunting. Similar trends were shown

at 6 degree angle of attack, though the reduction in control effectiveness resulting from nosetip blunting was reduced. The remaining 4 all moving wing geometries were tested in conjunction with the 17% bluntness ratio nosetip, 3 simulating varying degrees of trailing edge burnthrough and another simulating the effect of leading edge burnthrough. For all of the trailing edge burnthrough cases, the control effectiveness was found to be lower than that expected if control moment were simply proportional to wing area. This was attributed to a pressure relieving effect as a consequence of adding burnthrough, whereby the total pressure distribution on the remaining wing is decreased relative to the total pressure on the non-damaged wing. In the case of leading edge burnthrough, the measured control effectiveness was greater than that expected if control effectiveness proportional to wing area, which was attributed to the total pressure distribution on the non-damaged wing, which may exhibit a region of low total pressure in the removed section as a consequence of its proximity to the curved shock produced by the blunt wing leading edge.

Table of contents

List of figures

List of tables

Nomenclature

Roman Symbols

a	Speed of Sound
A_n	Nozzle throat area
A_v	Fast acting valve area
a_x	Acceleration in the body x axis
b	Vehicle span
c	Bearing Friction coefficient
C_{AC}	Calibration matrix relating the inertial forces to accelerometer readings
C_{l_0}	Body rolling moment derivative
C_{l_β}	Static lateral stability derivative
$C_{l_{\delta_n}}$	Roll control derivative(s)
$C_{l_{\dot{\beta}}}$	Quasi-steady derivative
$C_{l_{Body}}$	Aerodynamic Rolling Moment coefficent at zero attitude and no control effector deflections
$C_{l_{Control}}$	Control Effectiveness
$C_{l_{Dynamic}}$	Aerodynamic Rolling Moment coefficent from dynamic phenomena
C_{l_p}	Roll damping
C_{l_r}	Cross Derivative
C_l	Rolling Moment Coefficient

C_{M_0}	Body pitching moment derivative
C_{M_α}	Static pitch stability derivative
$C_{M_{\delta_n}}$	Pitch control derivative(s)
$C_{M_{\dot{\alpha}}}$	Quasi-steady derivative
C_{M_q}	Pitch damping derivative
C_{M_v}	Mach Tuck derivative
C_M	Pitching Moment Coefficient
D_{AC}	Acceleration Compensated Drag
D_{UC}	Uncompensated Drag
g	Acceleration due to gravity
L	Rolling Moment
L_{Barrel}	Length of the Ludwieg tunnel barrel
L_{AC}	Acceleration Compensated Rolling Moment
L_{aero}	Aerodynamic Rolling Moment
L_{CoG}	Rolling moment from CoG offset
$L_{Friction}$	Bearing Friction
L_{offset}	Reported rolling moment arising from zero bias of the strain gauges
$L_{Reaction}$	Rolling moment from actuator reaction moment
l_{ref}	Reference Length
L_{UC}	Uncompensated Rolling Moment
M	Pitching Moment
M_t	Mach number inside Ludwieg tube
p	Roll rate
q	Pitch rate

r	Yaw rate
Re	Reynolds Number
Re_u	Unit Reynolds Number
S_{ref}	Reference Area
t_{op}	Opening time of the fast acting valve
t_{wr}	Time taken for rarefaction wave to return to nozzle throat
V	Velocity
d	Diameter
J	Inertia about the cone axis
P	Pressure
q	Dynamic pressure
T	Temperature

Greek Symbols

α	Angle of attack
α_ϕ	Ratio between nozzle throat and facility valve, $\frac{A_n}{A_v}$
β	Angle of sideslip
β	Sideslip angle
$\ddot{\phi}$	Angular acceleration about the cone axis
γ	Ratio of Specific Heats
μ	Dynamic viscosity
Ω	Frequency of oscillations
ω	Angular velocity
ρ	Density
θ_c	Cone half angle

Subscripts

$fill$	Facility Fill Conditions
0	Stagnation conditions

Acronyms / Abbreviations

ACS	Aerodynamic Control Surfaces
AEDC	Arnold Engineering Development Centre
AHRS	Attitude Heading Reference System
ANDLM6QT	AFOSR Notre Dame Large Mach-6 Quiet Tunnel
BAM6QT	Boeing/AFOSR Mach-6 Quiet Tunnel
CFD	Computational Fluid Dynamics
CoG	Centre of Gravity
CUBRC	Calspan-University of Buffalo Research Centre
DAQ	Data Acquisition System
DLR	Deutsches Zentrum für Luft-und Raumfahrt
ELM	Extended Ludwieg Mode
GALCIT	California Institute of Technology LT
GDT	Gas Dynamics Tunnel
H2K	Hypersonic Wind Tunnel Cologne
HDT	High Density Tunnel
HLB	Hypersonic Ludwieg Tube Braunschweig
HTFD	Hypersonic Test Facility Delft
IMU	Inertial Measurement Unit
JAXA	Japan Aerospace Exploration Agency
JCEAP	Joint Computational/Experimental Aerodynamics Program

KULT	Konkuk University LT
LAPCAT	Long-Term Advanced Propulsion Concepts and Technologies
LICH	Light Isentropic Compression Heating
MEMS	Microelectromechanical Systems
NASA	National Aeronautics and Space Administration
PALM	Plenum Augmented Ludwieg Mode
PSD	Power Spectral Density
SHEFEX	Sharp Edged Flight Experiment
TH2	Hypersonic Shock Tunnel (Aachen)
TPS	Thermal Protection System
TUSQ	Tunnel University of Southern Queensland
VKF	Von Karman Facility
VKI	Von Karman Institute

Chapter 1

Introduction

1.1 Overview

The equations of motion for flight vehicles, yielded from application of Newtons second law, are typically expressed as a Taylor series expansion of perturbations of non-dimensionalised flight states about an equilibrium position, with partial derivative terms being replaced by aerodynamic coefficients. Broadly speaking, coefficients can be broken into two types: static - those associated only with vehicle shape and attitude - and dynamic - those that are dependent on the time history of the vehicles motion. Determination of any coefficient is typically achieved with 3 methods: 1) Computationally [1–5] 2) Ground tests in wind tunnels [6–8] and 3) Flight tests [9–11]. Computational techniques are both the fastest and the cheapest methods, but do not necessarily model all of the phenomena of flight and consequently often require wind tunnel validation data. Ground testing in wind tunnels typically involves subscale models, with freestream conditions scaled to match flight relevant non-dimensional parameters. These have the ability to replicate most aerodynamic phenomena, but there is commonly a compromise in experimental design in terms of model scale, model inertias or freestream flow conditions. Flight testing is ultimately the most representative way to determine aerodynamic coefficients, but is often prohibitively expensive and suffers from difficulties in maintaining constant test conditions, complicating the data reduction. For these reasons, building aerodynamic databases has historically been achieved through extensive subscale ground testing, with the trend turning towards computational techniques as their physical fidelity has grown. Though computational methods have been repeatedly predicted to one day completely replace wind tunnel testing, this reality has yet to come to pass and ground testing remains the foundation of flight vehicle development.

Currently undergoing a resurgence of interest is the development of hypersonic flight vehicles. Commonly defined as speeds in excess of five times the speed of sound, hypersonics

is more accurately defined as speeds at which certain phenomena become too influential to ignore. These effects range from viscous effects (shock boundary layer interaction, shock-shock interaction, viscous interaction, etc) to fully reacting, non-equilibrium flow, and all serve to increase the unknowns in the aerothermal environment surrounding the vehicle. As one would expect, the challenges of the hypersonic regime extend to the simulation of this complex aerothermal environment using ground test facilities. Hypersonic flows are of such energy that enthalpy matched, continuous hypersonic wind tunnels are not feasible due to high structural and thermal loads and the total power required (on the order of GigaWatts) [12]. Consequently, hypersonic ground testing must be performed in an array of facilities, each with their own limitations [13]. Blowdown facilities, which can produce test durations on the order of minutes, do exist but require significant infrastructure (making them costly to build and operate) and are typically limited in enthalpy[1]. Consequently, the most common types of hypersonic wind tunnels are impulse facilities, whose extremely short test duration (ranging from tens of microseconds to hundreds of milliseconds, dependent on flow enthalpy) allow them to avoid the containment issues that impede the design of continuous facilities. Impulse facilities are typically categorised by the enthalpy of the test flow they are able to produce (high or low), and consequently which aspects of the hypersonic flow environment they are able to simulate. For example, high enthalpy facilities offer the ability to replicate higher flight enthalpies (Mach number > 7), but the rapid expansion of a high-temperature equilibrium gas can lead to frozen species present in the test flow that aren't representative of flight. Low enthalpy impulse facilities generally produce cold, perfect gas flows, allowing for simulation of flight Reynolds number and Mach number, but not high temperature gas effects. The ability to essentially switch on/off certain flow phenomena by appropriate choice of facility is an important tool in breaking down the combined effects of a complex, interacting flowfield in order to investigate the fundamental physics of the problem.

Perhaps the defining characteristic of hypersonic flight is the extremely high aerothermal loading vehicles are subject to, with post-shock static temperatures potentially being on the order of thousands of Kelvin. In order for a vehicle to survive these loads, it must be equipped with an adequate Thermal Protection System (TPS), which can either be passive (e.g. ablatives) or active (e.g. transpiration cooling). At higher flight speeds, regions of the vehicle subject to highest aerothermal loading are typically protected by ablative materials. Ablatives chemically react with the high enthalpy flow surrounding the vehicle, absorbing energy and protecting the vehicle beneath. However, a consequence of these reactions is that the outer mold line of the vehicle changes over the duration of the flight, through

[1]The highest enthalpy blowdowns are AEDC tunnel 9, and the NASA Langley 8 foot High Temperature Tunnel, which can both reproduce up to Mach 7 flight enthalpies

either regression of leading edges (blunting), development of roughness patterns in the vehicle aeroshell, or both. Both of these changes can significantly affect the aerodynamic characteristics of the vehicle.

One of the regions subject to the extremes of the aerothermal loading (and hence often equipped with ablatives) are the vehicles control effectors, which typically take the form of Aerodynamic Control Surfaces (ACS) in the continuum regime. Deflection of ACS creates a shock wave upstream of the control surface, and the interaction of this shock with the gross vehicle flowfield (boundary layer, vehicle bow shock) creates an extremely complex flow environment which can result in non-linearities in their control effectiveness - that is, how much control moment they are able to produce. Control effectiveness is one of the key parameters identified in the building of aerodynamic databases as it directly affects the vehicles controllability and manoeuvrability. However, as will be demonstrated in Chapter 2, there have been extremely limited studies of how the shape change arising from ablation affects the resultant control effectiveness.

1.2 Research Motivation

On October 27th, 2005, Deutsches Zentrum für Luft-und Raumfahrt (DLR) launched the SHarp Edged Flight EXperiment (SHEFEX) [14], a flight experiment consisting of a highly faceted body designed to replicate as many configuration details of space vehicles as possible. This was launched on a two stage sounding rocket, with the second stage remaining attached during descent to provide stability and control with its ACS. Pre-flight, steady state Computational Fluid Dynamics (CFD) of the re-entry vehicle was performed in order to identify hotspots arising from shock-shock and shock-boundary layer interactions. Of particular interest to this thesis is the resultant thermal loads from the shock-shock interaction between the control fin shock and the tail can shock, shown in Fig. 1.1a, which predicts a hotspot on the order of 1500 K at the root of the control effector[2]. Additionally, upon descent, at altitudes of approximately 25 km and Mach number of approximately 6.3, an onboard camera imaging the ACS showed thermal degradation, manifesting as a sine-shape deformation and glowing of the leading edges, as shown in Fig. 1.1b. This flight experiment therefore clearly demonstrates the harsh aerothermal environment that control effectors are subject to, and how this can result in shape change.

On the 2nd June, 2001 the first test flight of the X-43A - a demonstrator for air breathing hypersonic engines - failed during the transonic phase of boost when an elevon in the launch vehicle was overstressed. A post flight Mishap Investigation Board identified three

[2]This is likely an over-prediction owing to the short flight duration and use of steady state CFD

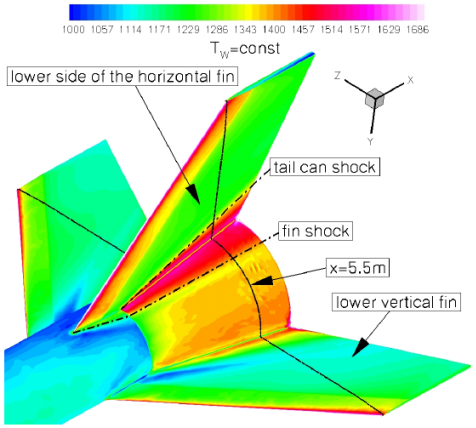

(a) CFD predictions highlighting heating regions arising from shock-shock interaction

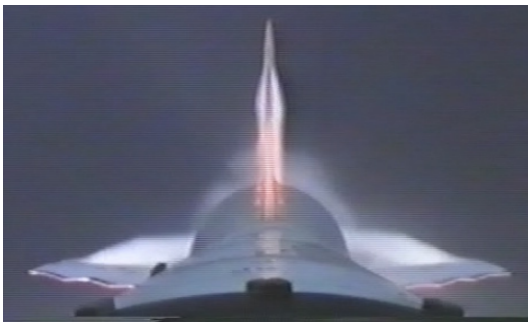

(b) Thermal degradation captured by onboard camera

Fig. 1.1 SHEFEX ACS aerothermal environment [14]

major causes of the flight failure, including inaccuracies in the aerodynamic modelling. A key contributor to these inaccuracies was a misinterpretation of wind tunnel data due to insufficient test points - control effectiveness studies had been performed with a resolution of 5 degree flap deflections and control effectiveness was linearly interpolated between them. Post-failure wind tunnel tests performed with a lower resolution of 2.5 degrees revealed a non-linearity in control effectiveness had been missed. This demonstrates the need for an extensive aerodynamic database, and points to a shortcoming in current test techniques (across the speed regimes) whereby costs associated with ground testing impose coarse resolutions of control effector deflections.

1.3 Control Effectiveness Studies

Control effectiveness studies generally consist of an experimental model with fixed control effector deflections and resultant forces measured with a force balance. These are typically performed in blowdown facilities [6–8, 15], where the available test time permits multiple attitudes to be characterised in a single run using a pitch-pause methodology. Pauses in model movement enable the flowfield to stabilise and hence permits determination of the static aerodynamic coefficients in the absence of dynamic effects. Choice of resolution is generally dictated by the costs associated with ground testing [6], and hence to improve the resolution of control effectiveness studies either: 1) further improvements to the range of attitudes/configurations characterised in a single run (e.g. models with movable control effectors) or 2) a reduction in the cost-per-run of a control effectiveness study must be made.

Noting that blowdown tunnels are generally expensive to operate relative to low enthalpy impulse facilities such as Ludwieg tunnels [16], point 2 can be achieved by improving the testing methodologies currently available in those facilities. This is particularly relevant if multiple variations of shape changed control effector/vehicle are desired to be characterised.

To date, those control effectiveness studies performed in low enthalpy impulse facilities have been either fully static, with only a single attitude and control effector deflection characterised in a run [17–19], or fully dynamic (no pauses) [20, 21]. Static tests allow direct measurement of the static coefficients, but naturally require an extensive number of tests to characterise a vehicle. Whilst fully dynamic tests have the ability to attain a continuous resolution of control effectiveness with control deflection and attitude, care must be taken during experimental design in order to ensure that dynamic phenomena are either not influencing the measurements or can be isolated from static coefficients, particularly if the reduced angular rates in the experiment are not representative of flight. The only dynamic studies of control effectiveness to date have presented the total moments created, without any information about the scaling of the reduced angular rates, and consequently have not identified the static aerodynamic coefficients. There are therefore two ways to improve the control effectiveness testing methodologies in Ludwieg tunnels, both of which centre about improving the amount of characterisation that can be attained from a single test: 1) implementation of deflection-pause techniques, allowing multiple control effector deflections to be characterised in a single test and 2) development of a dynamic test technique that allows isolation of static coefficients. Both of these improvements are dependent on the test time the facility can produce, with dynamic test techniques typically requiring a minimum of 200 ms [22].

1.4 Ludwieg Tunnels

The most common type of low enthalpy hypersonic impulse facility is the Ludwieg tunnel due to its ability to provide steady hypersonic flow conditions at a relatively low cost. These facilities can match flight Mach and Reynolds number, but their biggest limitation, (besides their low enthalpy nature) is the test time they are able to produce. Generally speaking, the test time produced is proportional to facility length, with facilities across the world producing test times between 50-350 ms when operating in standard Ludwieg Mode. For the Oxford High Density Tunnel (HDT), the experimental facility used in this thesis, the available test time in Ludwieg Mode is limited to 35-50 ms. Clearly, if the aforementioned improvements to control effectiveness studies are to be made, the test time available in the HDT needs to increased.

1.5 Research Questions

The overarching research questions for this thesis are twofold:

1. **How can control effectiveness studies be improved?**
2. **How does shape change of the vehicle nosetip and all moving wings impact control effectiveness?**

In order to address these questions, this thesis will:

1. **Increase the test time available in Ludwieg Tunnels.** This will be achieved by the implementation of two new modes of operation in the Oxford High Density Tunnel: Extended Ludwieg Mode (ELM) and Plenum Augmented Ludwieg Mode (PALM). ELM is a quasi-steady mode of operation, in which the steadiness of a LM plateau is sacrificed for a significant extension of test time. PALM is a steady mode of operation, in which the overall unit Reynolds number capability of the facility is traded for steady test time capability. Both modes are achieved through modification of the way in which the facility plug valve opens.
2. **Improve the state of the art for control effectiveness measurements in Ludwieg Tunnels**. This will be achieved by leveraging the extended test duration developed in point 1 to characterise multiple control effector deflections in a single test and develop a free-to-roll model for continuous, low uncertainty, resolution of control effectiveness as a function of roll position. The free-to-roll technique will leverage the inherently low aerodynamic damping characteristic of hypersonic vehicles, in combination with low reduced angular rates, to provide a low uncertainty measurement of the static aerodynamics in isolation of dynamic phenomena. This will be validated against force balance data to demonstrate that static coefficients are being obtained.
3. **Investigate the effect of control effector shape change on resultant control effectiveness**. As demonstrated by SHEFEX, the extremely harsh aerothermal environment experienced by a hypersonic vehicle can have a significant effect on the outer mold line of the vehicle. This study will use a 10 degree half angle cone fitted with all moving wings to investigate the effect of blunting of the vehicle nose tip and all moving wings on the control effectiveness. Additionally, varying degrees of leading and trailing edge root burnthrough of the all moving wings will be investigated.

1.6 Thesis Structure

The work in this thesis is divided into 6 chapters. Submitted in an integrated format, three of these chapters (Chapters 3-5) are stand-alone journal articles. To summarise, the chapters in this thesis are:

1. **Chapter 2: Literature Review** This chapter provides a literature review of force measurement techniques, with a focus on how techniques change with decreasing test durations, and control effectiveness studies. Finally, a summary of Ludwieg tunnels around the world and their performance is given.

2. **Chapter 3: Blowdown Operation of Ludwieg Tunnels** This chapter details the development of Extended Ludwieg Mode (ELM), and Plenum Augmented Ludwieg Mode (PALM) in the Oxford High Density Tunnel.

3. **Chapter 4: Control Effectiveness studies in Ludwieg Tunnels** This chapter presents the improvements to the state of the art for control effectiveness studies in Ludwieg Tunnels.

4. **Chapter 5: Effect of shape change on control authority**. This chapter explores the influence of shape change on the control authority provided by all moving wings. Shape changes investigated are blunting of vehicle nosetip, blunting of control effector leading edges, and finally leading and trailing edge root burnthrough of the control effector.

5. **Chapter 6: Conclusion and Recommendations for Future Work** A conclusion of the work presented in this thesis and recommendations for future work are made.

Chapter 2

Literature Review

This chapter presents a review of the literature relevant to this thesis. It begins with some background knowledge relating to aerodynamic coefficients and ground testing, before summarising force measurement techniques and reviewing control effectiveness studies. Finally, it concludes with a brief section on the facility used, and upgrades required, for this work.

2.1 Background

Before reviewing any aerodynamic ground testing literature, it is important to review some aspects of aerodynamics. Since this thesis focuses on aerodynamic control, this discussion will be limited to the expressions for aerodynamic pitching and rolling moment, given in Eq. 2.1 and Eq. 2.2, respectively:

$$M = \frac{1}{2}\rho V^2 S_{ref} l_{ref} C_M \qquad (2.1)$$

$$L = \frac{1}{2}\rho V^2 S_{ref} l_{ref} C_l \qquad (2.2)$$

Where M and L are the pitching moment and rolling moment respectively, ρ is the freestream density, V is the flight velocity, S_{ref} is a reference area, l_{ref} a reference length (often vehicle length for pitch, and span for roll), and C_M and C_l are the pitching and rolling moment coefficients respectively. The aerodynamic coefficients can be broken down into static - those that depend only on vehicle shape and attitude - and dynamic - those that depend on the time history of vehicle motion. These are typically expressed as perturbations of non-dimensionalised flight states about an equilibrium condition as per Eq. 2.3 and Eq. 2.4:

$$C_M = \underbrace{C_{M_0} + C_{M_\alpha}\alpha + \sum_{n=1}^{n} C_{M_{\delta_n}}\delta_n}_{Static} + \underbrace{C_{M_v}\frac{\Delta v}{V} + C_{M_q}\frac{ql}{2V} + C_{M_{\dot{\alpha}}}\frac{\dot{\alpha}l}{2V}}_{Dynamic} \tag{2.3}$$

$$C_l = \underbrace{C_{l_0} + C_{l_\beta}\beta + \sum_{n=1}^{n} C_{l_{\delta_n}}\delta_n}_{Static} + \underbrace{C_{l_p}\frac{pb}{2V} + C_{l_{\dot{\beta}}}\frac{\dot{\beta}b}{2V} + C_{l_r}\frac{rb}{2V}}_{Dynamic} \tag{2.4}$$

A breakdown of these equations is given in Table 2.1, and a figure to aid interpretation in Fig. 2.1. Note that the definition of control derivatives are slightly different in form to those predominantly used in the literature (in which control effector contributions are expressed in the more conventional form of δ_e for elevators, δ_r for rudders, and δ_a for ailerons), in an effort to generalise the equations, recognising that not only do control effectors take different forms in the hypersonic regime (elevon, rudderon, body flaps, canards, etc), they also - as their names suggest - begin to control multiple attitude channels owing to the greater cross coupling between the attitude channels.

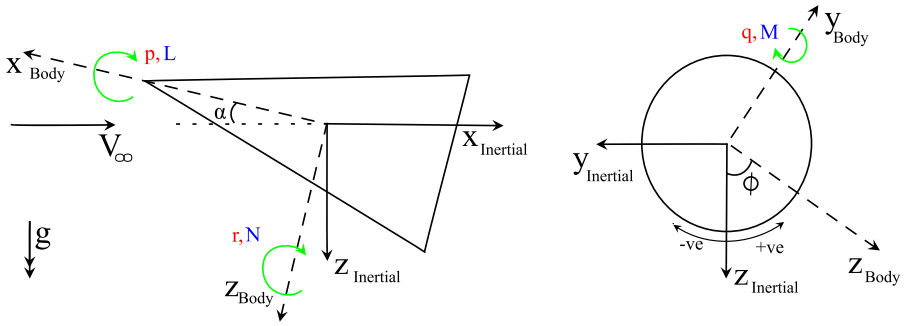

Fig. 2.1 Diagram of flight axes, with the flight angles (black), angular rates (red) and Moments (blue) annotated. Angle of sideslip omitted.

With the background of the aerodynamic coefficients established, it is now important to review the conditions for similarity between experiment and flight in order to understand what effects are being simulated in the experiment and consequently how to extrapolate experimental data to flight. An overview of scaling parameters is given in Wolowicz [23] and summarised in Table 2.2 for application to rigid model testing in cold flow hypersonic facilities such as Ludwieg tunnels. It can be seen that the base similitude requirements for both static and dynamic coefficients are Reynolds number and Mach number scaling, and that dynamic coefficients additionally require scaling of the reduced angular rates. Scaling of Mach number and Reynolds number are relatively trivial to achieve in most hypersonic facilities, but scaling of reduced angular rates is generally regarded as much more difficult

Table 2.1 Breakdown of terms in the pitching and rolling moment coefficient equations

Coefficient	Name	Comment
α	Angle of attack	Angle between the body x axis and the effective wind
β	Sideslip angle	Angle between the body y axis and the effective wind
V	Freestream velocity	-
b	Vehicle span	-
p	roll rate	Angular rate about body x axis
q	pitch rate	Angular rate about body y axis
r	yaw rate	Angular rate about body z axis
C_{M_0}	Body pitching moment derivative	Pitching moment coefficient when all other derivatives are zero
C_{M_α}	Static pitch stability derivative	Stable if negative
$C_{M_{\delta_n}}$	Pitch control derivative(s)	-
C_{M_v}	Mach Tuck derivative	-
C_{M_q}	Pitch damping derivative	Dynamic damping derivatives. Often not possible to separate
$C_{M_{\dot{\alpha}}}$	Quasi-steady derivative	
C_{l_0}	Body rolling moment derivative	Rolling moment coefficient when all other derivatives are zero
C_{l_β}	Static lateral stability derivative	Stable (effective dihedral) if negative
$C_{l_{\delta_n}}$	Roll control derivative(s)	-
C_{l_p}	Roll damping	-
$C_{l_{\dot{\beta}}}$	Quasi-steady derivative	-
C_{l_r}	Cross Derivative	-

owing to the difficulties of properly scaling inertia between the flight vehicle and experimental model [24].

2.2 Force Measurement Techniques

Before reviewing literature on experimental hypersonic control effectiveness studies, which are a subset of force measurements performed during aerodynamic characterisation, it is important to first review the force measurement techniques themselves. Bernstein [25] can be viewed as the seminal paper on force measurement techniques in hypersonic facilities, and any reader looking for information/discussion on force measurement techniques is encouraged to start there. This section of the literature review has been split into static and

Table 2.2 Summary of the most critical scaling parameters between flight and wind tunnel testing for hypersonic aerodynamics in the absence of high temperature/real gas effects and aeroelasticity.

Parameter	Definition	Statics	Dynamics	Oscillations	Comments
Reynolds Number	$\frac{\rho V l}{\mu}$	Yes	Yes	Yes	Ratio of inertia to viscous forces
Mach Number	$\frac{V}{a}$	Yes	Yes	Yes	Compressibility effects
Reduced Angular Velocity	$\frac{\omega l}{V}$	No	Yes	No	Applies to angular rates of flight vehicle (p, q, r).
Strouhal Number	$\frac{\Omega l}{V}$	No	No	Yes	Applies to unsteady oscillatory perturbations of the flight vehicle.
Froude Number	$\frac{V^2}{lg}$	Yes and No	Yes and No	No	Buoyancy forces - only applicable to free-flight, often not possible to match in subscale tests. Affects predictions of trim angle and manoeuvrers

dynamic techniques, where the name of each indicates the model motion during the test, rather than the aerodynamic coefficients being identified.

2.2.1 Static Techniques

The ubiquitous force measurement technique across the speed regimes is use of a statically calibrated force balance. These are typically used in facilities with run times sufficient for any vibrations associated with tunnel startup/model injection to damp out before measurements are taken; only possible in the hypersonic regime within blowdown facilities. The majority of hypersonic facilities are impulsive in nature, which, as noted by Bernstein [25], creates 2 key difficulties for attaining low uncertainty measurements: 1) large aerodynamic loads during startup (up to an order of magnitude higher than the loads in the test [26]) requiring high load ratings for the force balance and 2) short test durations preventing damping out of vibrations induced by startup and resulting in an oscillatory force signal. It is possible to reduce the magnitude of the vibrations through careful design of the force balance to maximise stiffness and hence natural frequency, but, given that the strain gauges measure displacements, this can

come at the expense of signal. Additionally, it is the natural frequencies of the overall force measurement system, including the force balance, the model and its supporting structures, that are of primary importance, not just the natural frequencies of the force balance itself. This is well demonstrated by Jessen and Grönig [27], who present the design of a 6-axis force balance for use in the Aachen shock tunnel TH2. The minimum acceptable natural frequency was decided to be 1 kHz, allowing for 3 to 5 full cycles of oscillations/vibrations across the test time and enabling extraction of force data via averaging. Though the force balance itself achieved a lowest natural frequency of 2.4 kHz, addition of the model reduced the natural frequency to 1 kHz - the predefined lower limit - and mounting of the model in its supporting structure further reduced the natural frequencies to below 200 Hz. Störkmann [28] presents experimental results using the Jessen and Grönig force balance installed in a 15° half angle cone. The results for the lift coefficient are shown in Fig. 2.2, demonstrating a clear oscillatory ringing with period of approximately 5 ms. Fortunately, for this test condition, there was sufficient test time for 3 oscillations and hence averaging was able to be used to extract the force coefficients. Further force balance studies employing the minimum 3-5 oscillation periods to set minimum natural frequencies are Juhany [29] and Yunfeng [30].

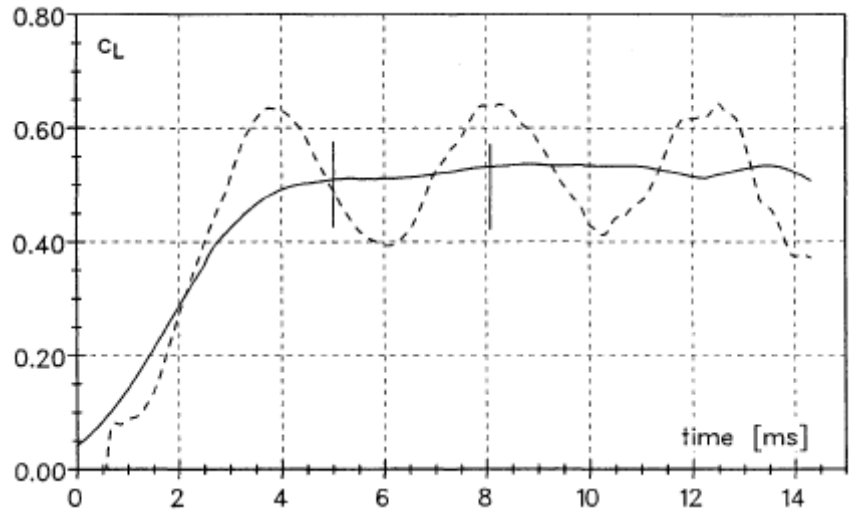

Fig. 2.2 Uncompensated (dashed) and moving average filtered (solid) lift coefficient for the Jessen and Grönig force balance installed in a 15 degree half angle cone. Taken from Störkmann [28]

Evidently, even with force balances specifically designed to maximise the natural frequency, testing in impulse facilities often produces force measurements that are oscillatory in nature. To account for this, and enable testing in shorter duration flows, Martin [31] developed acceleration compensation, where accelerometer data is used to remove the contri-

butions from vibrations. This technique has been employed with success in multiple papers [31–36], all of which utilise linear accelerometers to measure the vibrational accelerations. Bernstein [25] notes the importance of accelerometer location in the model: ideally, the accelerometers should be as close as possible to the force balance to maximise the likelihood that the acceleration reading is in phase with the force signal. However, moment compensation in particular requires accelerometers to be placed at model extremities in order to attain sufficient signal.

Störkmann [28] demonstrated two types of acceleration compensation: sting based and model based, where the name of each indicates the location of the accelerometers. Sting based compensation removes contributions from sting vibrations, whilst model based removes oscillations arising from the elasticity of the balance. The inertial compensation methodology is the same between the two methods, with the aerodynamic forces, F_{aero}, being related to the measurements, $F_{measured}$, and accelerations, $a_{measured}$, by Eq. 2.5:

$$F_{aero} = F_{measured} - C_{AC} * a_{measured} \tag{2.5}$$

Where C_{AC} is a calibration matrix relating the inertial forces to accelerometer readings. Störkmann determined the values of the terms inside the C_{AC} matrix with a fusible link dynamic calibration for the sting based compensation. However for the model based compensation, where C_{AC} becomes the model inertia matrix, the aerodynamic coefficients were assumed to be constant across a portion of the test (i.e. measured forces directly follow facility nozzle supply conditions), and values for C_{AC} were determined based on a least squares methodology. This has the advantage of not needing precise knowledge of the inertia matrix, but the results attained are dependent on the duration of the window used during the least squares fit. Sting based compensation for the lift coefficient from Störkmann is shown in Fig. 2.3a, demonstrating an elimination of the oscillations in the raw data. A comparison of model and sting based compensation is shown in Fig. 2.3b, which shows the dependency of the model based compensation on the windowing duration. It can be seen that sting based acceleration produces a lower estimate of normal force coefficient than model based, which is attributed to the accelerometers in the model not detecting a low frequency acceleration induced by tunnel startup.

Whilst acceleration compensation can be used to reduce the required test time for force measurements, this can still be insufficient for some hypersonic impulse faculties with sub-millisecond test durations (e.g. shock tunnels, expansion tunnels) and consequently the force balance must be dynamically calibrated. Though dynamic calibration can be applied to force balances of typical construction [37, 38], it is also possible to design a force balance system for dynamic calibrations. This work began at the University of Queensland in 1991, where

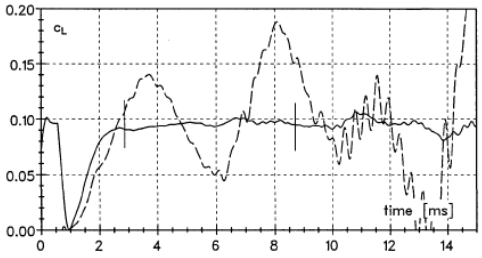

(a) Raw (dashed) vs acceleration compensated (solid) lift coefficient with sting based acceleration compensation

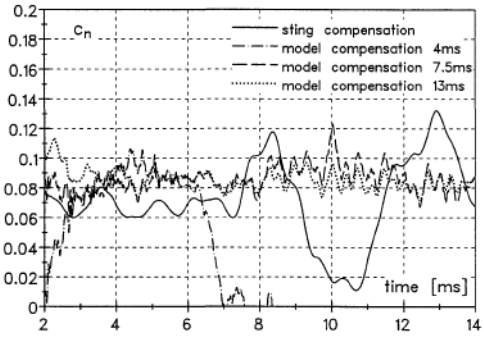

(b) Influence of averaging window duration for determination of C_{AC}

Fig. 2.3 Acceleration compensated force measurements from Störkmann

Sanderson and Simmons [39] developed the first Stress Wave Force Balance, capable of measuring forces in tests of 1 ms duration. This balance, shown in Fig. 2.4a consisted of an aerodynamically shielded, 1.63m long brass sting with strain gauges mounted 200 mm downstream of the model. The novel aspect of this design is the one-dimensionalisation of the stress wave, with the output of the strain gauges being unaffected until the return of the stress wave to the instrumentation location. A comparison of the raw (indicated) drag and the dynamically calibrated drag (deconvoluted) is shown in Fig. 2.4b, with drag predicted from measurements of the test section pitot pressure overlaid. It can be seen that dynamic calibration has changed the form of the trace significantly, producing a trace that follows the pitot pressure and closely matches the theoretical predictions. It is worth noting that although high quality force data can be attained with SWFB techniques, there are difficulties associated with performing the dynamic calibrations (which can be extremely labour intensive) and forming the impulse response of the force measurement system. This technique is an active work of research at the University of Queensland, being extended to multi-component force balances [40, 41] and down to test durations on the order of tens of microseconds [42–44]. For a more thorough review of stress wave force balances and their calibration, see [45].

2.2.2 Dynamic Techniques

Walchner (1964) [46] presents results of dynamic stability testing in a Mach 14 blowdown tunnel, investigating the dynamic derivatives in pitch, $C_{m_q} + C_{m_{\dot{\alpha}}}$. These were free oscillation experiments, consisting of a 5.6 degree half angle cone connected to a sting by an elastic flexure which allowed the model to oscillate in pitch. Three flexures were used, all of beryllium copper construction, allowing testing at reduced frequencies of 0.0014 or 0.0013.

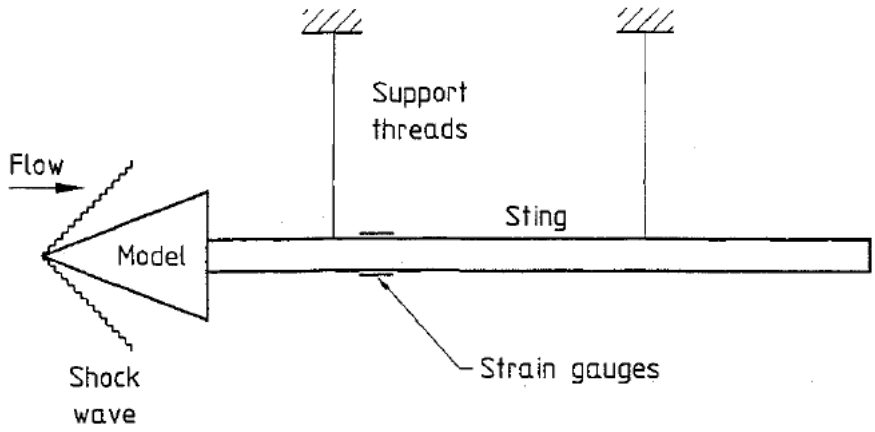

(a) Schematic of the Stress Wave Force Balance.

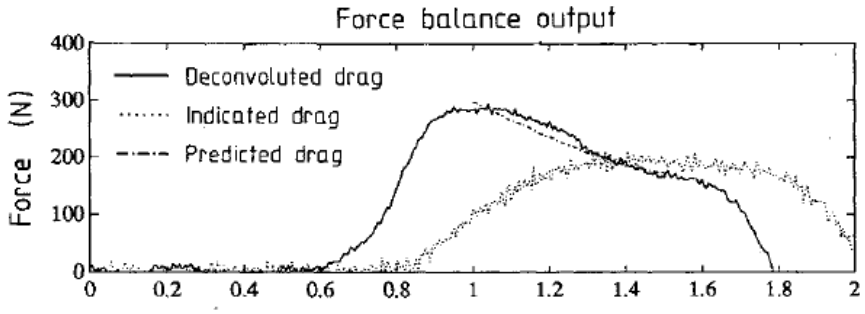

(b) Comparison of raw (indicated, dotted) vs dynamically calibrated (deconvoluted, solid) drag and predicted (chain)

Fig. 2.4 Sanderson's Stress Wave Force Balance [39]

Oscillation amplitudes were recorded using a high speed camera, and wind off tare runs were performed under vacuum ($\approx$ 135 Pa) before and after each test in order to characterise the spring constants and structural damping of the flexures, though it is not clear how motion was excited in the wind-off case. Values for the dynamic stability derivatives, $C_{m_q} + C_{m_{\dot{\alpha}}}$, and static stability derivative, C_{m_α}, were attained from a least squares fit of angular data to the linearised one degree of freedom differential equation for small amplitude oscillations. Good agreement for C_{m_α} with theoretical predictions was demonstrated, though no comparison of dynamic derivatives was possible due to a lack of contemporary experiments or theoretical predictions for this geometry. Stetson [47] presents a further comparison between measurements using the free oscillation setup and those obtained from static tests performed with a conventional static strain gauge balance for a biconic re-entry configuration. Values for the normal force coefficient, C_N, the pitching moment coefficient, C_m, the static stability derivative, C_{m_α}, and the centre of pressure location, X_{CP} were compared. For the

dynamic techniques, C_{m_α} was attained as per Walchner [46], and C_m was attained from integration of C_{m_α} data, whilst C_N was attained from integration of C_{N_α} data generated from experiments with different pivot points in the model. Naturally, the dynamic derivatives were not able to be attained from the static testing. The static data provided a direct measurement of C_N and C_m, whilst C_{m_α} was obtained via a differentiation of the C_m vs α curve. For both tests, the centre of pressure was calculated as per Eq 2.6:

$$\frac{X_{CP}}{L} = \frac{X_{CG}}{L} - \frac{C_m}{C_N} \tag{2.6}$$

Excellent agreement between the two techniques was shown for all coefficients, but of particular interest are the uncertainties associated with each technique, shown for centre of pressure location in Fig. 2.5b. It can be seen that the uncertainty associated with static techniques is at a maximum for low angles of attack, owing to the balance uncertainty dominating the measurement, but decreases with increasing angle of attack (and therefore force signal). This is converse to the dynamic uncertainty, which is low at zero angle of attack but gradually increases with increasing angle of attack, with the increase attributed to unsteady flowfield effects.

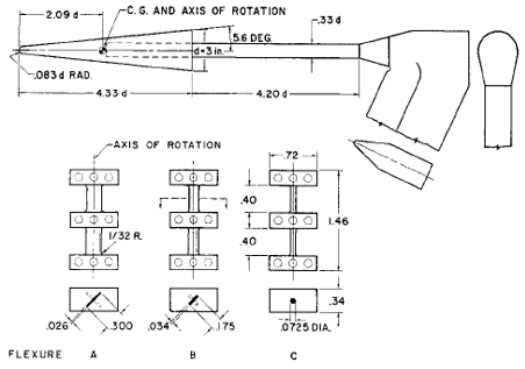

(a) Cone and flexures used for pitch dynamic stability testing [46]. All dimensions in inches

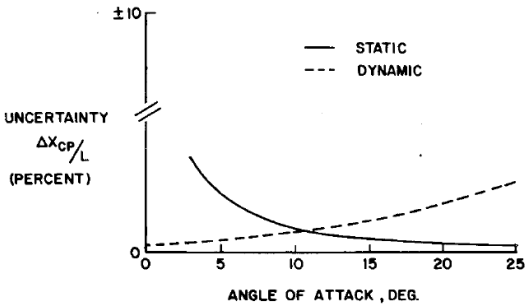

(b) Uncertainty comparison between dynamic free oscillation studies and static experiments [47]

Fig. 2.5 Dynamic free oscillation studies

Walchner (1969) [48] investigated the roll damping derivative for a 10 degree half angle cone using the spin decay technique. A single degree of freedom (roll) gas bearing was used to support the model, and an initial spin rate set by an electronic motor connected to the model by a clutch mechanism. Roll rate was measured using permanent magnets in the model and a pickup coil on the sting. The wind-on rate of deceleration was compared with a wind-off tare run, performed under vacuum (test section pressure $\approx$ 270 Pa) at the same spin rate and gas bearing supply pressure (both factors which affect gas bearing friction),

to separate contributions from the aerodynamic roll damping and bearing friction. Mach numbers of 12.7 and 14.2 at angles of attack between $\pm 8^{\circ}$ and reduced roll rates between 0.003 and 0.021 were tested. Excellent agreement between the measured roll damping and theoretical predictions based on Quinn [49] was observed. At zero degrees angle of attack, the roll damping was observed to decrease with nose blunting, but this effect was reduced with increased angle of attack. Finally, no dependency on roll rate/reduced frequency was observed for roll damping across the angular rates tested.

Regan [50] extended the spin decay methodology to pitch and yaw damping. In this case, the experimental model featured a three degree of freedom gas bearing which permitted restrained motion in pitch and yaw (approximately 7 degrees) and unrestrained motion in roll. At the start of the test, the model was constrained in pitch and yaw and spun by an integral turbine through which pressurised air was ejected. Once the desired roll rate was achieved, the turbine was disengaged from the model, allowing unrestrained motion. A disturbance was then imparted to the model with a kicking air jet impinging internally and the resultant oscillations measured with an orthogonal camera setup. This setup permitted measurement of both the pitch and yaw static stability derivatives and damping derivatives. Regan used this to investigate the dynamic stability of a 7 degree half angle cone with an ablating nosetip. The nosetip, made from Camphor (a low temperature ablative), was initially spherically blunt but ablated to a biconic structure over the course of the approximately 30 s tests. Regan found that the ablating model exhibited periods of dynamic stability and dynamic instability, though was not able to provide a "convincing argument" to explain this phenomenon.

The final dynamic test technique to be discussed is free-flight, in which the model is released into the core flow and is free to move in 6 degrees of freedom. Free-flight is in active use at the University of Oxford [51, 52, 21, 53], DLR [54–56], University of Southern Queensland [57–61], Von Karman Institute (VKI) [62–64], University of Maryland [65, 66], and Japan Aerospace Exploration Agency (JAXA) [67–69], but this review will focus on the works performed at the University of Oxford. To summarise the others, free-flight testing at JAXA and DLR has primarily been of large, high inertia models in extremely short test durations (order of milliseconds), resulting in very small model displacements and purely static aerodynamics being attained, whilst the work at VKI and Maryland primarily focus on satellite demise. The work at the University of Southern Queensland is closest in scope to the works discussed subsequently, mostly focusing on static aerodynamic coefficient identification. For a thorough review of the free-flight techniques employed in these institutions, please see Hyslop (2023) [21].

Hyslop (2024) [53] presents a comparison between the "static" free-flight technique and force balance measurements for a 7 degree half angle cone at Mach 5 in the Oxford

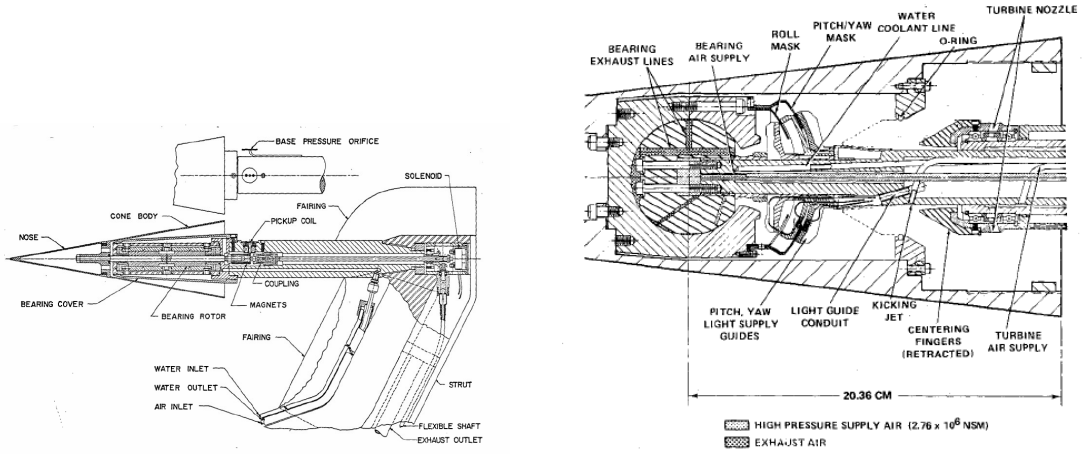

(a) Experimental model used by Walchner [48] for roll spin decay tests

(b) 3 degree of freedom gas bearing and pneumatic oscillation excitation mechanism used by Regan [50] for pitch and yaw oscillation decay tests

Fig. 2.6 Experimental models used for spin and oscillation decay tests

High Density Tunnel. Despite obviously exhibiting significant model motion over the course of the test, the free-flight experiments are termed static as the model was ballasted such that the centre of gravity was coincident with the centre of pressure, resulting in minimal aerodynamic moments and angular rates and allowing resolution of the static aerodynamic coefficients in isolation of dynamic effects. Model motion was measured with an onboard Microelectromechanical Systems (MEMS) Inertial Measurement Unit (IMU) and off-board image tracking. The force balance was both statically and dynamically calibrated, with the latter being performed with an impulse hammer. The unfiltered force traces are shown in Fig. 2.7 demonstrating excellent agreement between the three techniques. As expected the static force balance measurement features high frequency oscillations, which the dynamic calibration is largely able to remove. Finally the free-flight data is non-oscillatory and follows the facility nozzle supply pressure trace as expected. Uncertainty analysis performed by Hyslop showed that although dynamic calibration of the force balance reduces uncertainty relative to the statically calibrated case, free-flight offers significantly lower uncertainties than either.

Hyslop (2023) [21] presents a comparison between “static” free-flight and free-pitching free-flight. For free-pitching free-flight, the model was ballasted to be statically stable, but reduced angular rates were not scaled - preventing dynamic coefficients from being attained. A comparison between the techniques for lift and drag is shown in Fig. 2.8. Excellent agreement between static and dynamic tests was found for lift, but there is an offset which

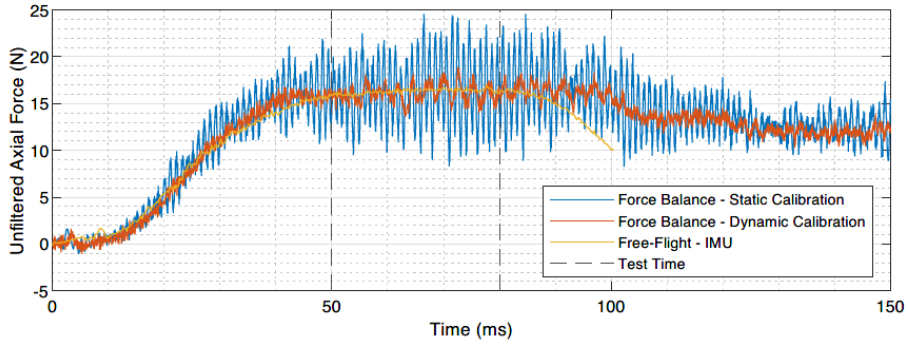

Fig. 2.7 Comparison of static free flight and statically and dynamically calibrated force balance measurements.

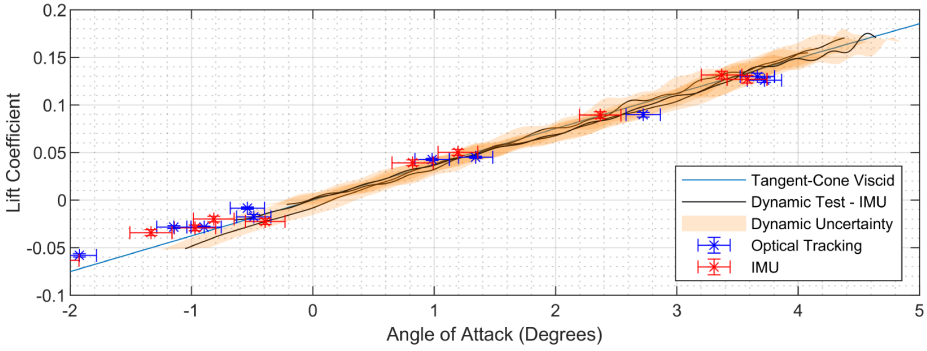

(a) Lift Measurements

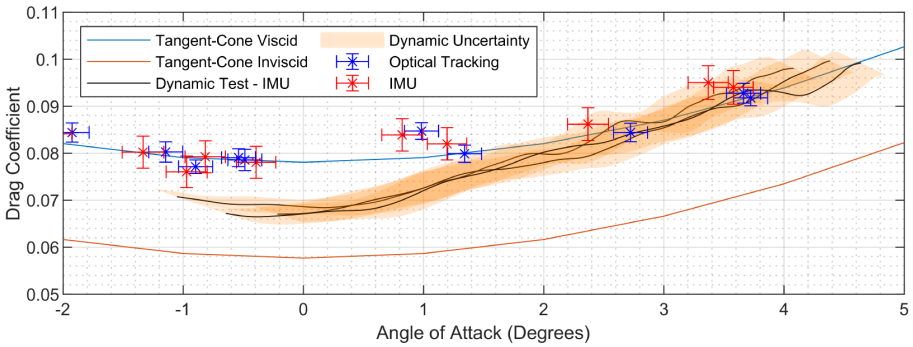

(b) Drag measurements.

Fig. 2.8 Comparison of static free flight data and pitching free-flight data from Hyslop [21]

increases with decreasing angle of attack for the drag. Hyslop attributed this offset in measured drag to either dynamic effects (i.e. base pressure not stabilised) or misalignment in yaw. It can also be seen that the measured lift and drag data is slightly oscillatory in the pitching free-flight tests, which was a result of flexibility in the IMU mounting structure internal to the model. The lift data from this work demonstrates the feasibility of extracting static aerodynamic coefficients from tests with dynamic model motion in the absence of

appropriate dynamic scaling, though the drag data shows that care must be taken to understand the sensitivity of the force measurements of interest to dynamic effects.

2.2.3 Summary

In summary, this section has reviewed the force measurement techniques used in hypersonic facilities. It has highlighted the difficulties in measurement of static coefficients imposed by short test duration and highlighted some techniques for improving the quality of force data attained. Additionally, it has demonstrated the feasibility of attaining static aerodynamic coefficients from dynamic tests, though care should be taken to understand the sensitivity of those measurements to the model dynamics. A summary of the test techniques, including the test times over which they have been demonstrated, is given in Table 2.3.

Table 2.3 Summary of force measurement techniques reviewed, the test times required/demonstrated across hypersonic facilities, and some advantages and disadvantages.

SFB = Static Force Balance, ACFB = Acceleration Compensated Force Balance, DCFB = Dynamically Calibrated Force Balance, t_{char} = characteristic time of measurement system.

Measurement Technique	Required Test Time	Advantage	Disadvantage
SFB	$\geq 3-5*t_{char}$	Simple	Force measurement is often oscillatory
ACFB	$\geq$ 1 ms	Can remove oscillatory content	Accelerometer locations can be compromised due to model geometry
DCFB	50 μs - 1 ms	Works for shortest test times	Dynamic calibrations difficult to perform
Free-flight	1 - 50 ms	Low uncertainty relative to force balance techniques	Model can leave core flow during test, no onboard control capability (to date)
Dynamic techniques	$\geq$ 100 ms	Allows static and dynamic derivatives to be attained	Complicated model design

2.3 Control Effectiveness studies

Having reviewed the force measurement techniques available in hypersonic facilities, there is now sufficient understanding to review control effectiveness studies themselves. This section presents an overview of the literature on control effectiveness studies for Aerodynamic Control Surfaces (ACS) in the hypersonic regime. As control effectiveness is a quantity directly affected by the interaction of flow over the ACS and the gross vehicle flowfield, these studies are typically performed at a vehicle level rather than fundamental studies on flat plates. However, use of simple, canonical geometries is still useful for technique improvement and CFD validation, so this subsection begins with canonical geometries before moving onto literature relating to complex vehicles.

2.3.1 Canonical Geometries

Oberkampf [15] gives experimental results for force and moment coefficients for the Joint Computational/Experimental Aerodynamics Program (JCEAP) geometry - a 10 degree half angle cone with a flap mounted on a slice parallel to the axis of the vehicle. As the name of the program suggests, its primary purpose was to improve the synergy between computational and experimental programs by producing a high quality experimental dataset, with rigorous uncertainty analysis, for validation of computational codes. Experiments were conducted in a blowdown-to-vacuum hypersonic wind tunnel at a Mach number of 8. Forces and moments were measured with a 6 component, temperature compensated force balance mounted inside the model, located such that the centre of pressure lay between the gauges. Static flap deflections of 0, 10, 20 and 30 degrees were used. Axial force was corrected for base pressure using measurements of base pressure made at 5 radial locations. Oberkampf attributed the uncertainty in the experiments to two main influences: 1) instrumentation uncertainty and 2) freestream non-uniformity, where the first is essentially the contributions to the uncertainty of everything except freestream non-uniformity (e.g. strain gauge hysteresis, thermal sensitivity shift, freestream alignment, etc). Repeat runs with identical model setups at the same location were used in assessment of the instrumentation uncertainty, whilst contributions arising from flowfield non-uniformity were determined from a statistical analysis of repeat runs with the model at different locations in the test section. Multiple axial stations were used, and radial non-uniformity was assessed with pairs of run with mirror symmetry - that is, one run at positive angle of attack and 0 degrees roll, and an analogous run at negative angle of attack and 180 degrees roll. A summary of the uncertainties for each measurement is shown in Table 2.4, and shows that for C_n, C_m and x_{cp}, the uncertainty is dominated by the flowfield

Table 2.4 Breakdown of uncertainties from Oberkampf [15] (reproduced). $\hat{\sigma}$ is the absolute uncertainty in the measurements, and % highlights the percentage contribution from each uncertainty type to the total uncertainty

Uncertainty	C_n		C_m		x_{cp}/L		C_a	
	$\hat{\sigma}$	%	$\hat{\sigma}$	%	$\hat{\sigma}$	%	$\hat{\sigma}$	%
Instrument	0.47×10^{-3}	20	0.41×10^{-3}	19	0.41×10^{-3}	9	0.43×10^{-3}	63
Flow	0.94×10^{-3}	80	0.85×10^{-3}	81	1.32×10^{-3}	91	0.32×10^{-3}	37
Total	1.05×10^{-3}	100	0.94×10^{-3}	100	1.39×10^{-3}	100	0.54×10^{-3}	100

non-uniformity. This was not the case for C_a, which Oberkampf attributed to instrumentation inaccuracies in removing base drag from total axial force.

Walker [70] presents the accompanying computational results to Oberkampf's experiments, generated using a Parabolized Navier-Stokes (PNS) code in combination with a time iterative Navier-Stokes solver in the separated/reverse flow regions. It was found that whilst agreement for the non-deflected case was very good, increasing flap deflections increased the disagreement between the computational and experimental results, with computations of the 20 and 30 degree deflections "seriously in error", owing to the difficulties associated in numerically predicting the shock/boundary layer/separated flow interactions.

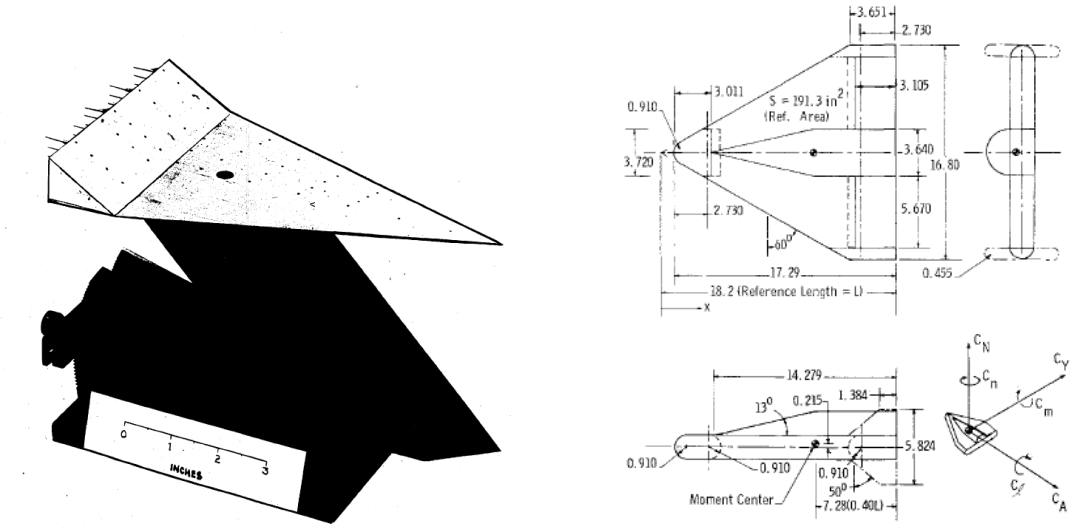

(a) Delta wing vehicle tested by Rao [17]

(b) Pyramidal liftigin body tested by Kaufman [71]

Fig. 2.9 Experimental models used in control effectiveness studies

Rao [17] presents experimental measurements of control effectiveness on trailing edge flaps on two delta wing vehicles (70° and 76° sweepback), shown in Fig. 2.9a. Experiments

were performed in the Imperial College gun tunnel at a freestream Mach number of 8.2, and forces were measured with a three-component force balance. It was found that the separation arising from deflection of the trailing edge flaps induced boundary layer transition, with transition occurring further upstream for the 76° delta wing for all incidences, producing a consistently smaller separation length and increased control effectiveness from the flaps. For 30 degree flap deflections, Rao found that the loads acting on the flap were dominated by the impingement of the expansion fan formed by interaction of the flap and delta wing shocks.

Kaufman [71] presents similar findings for a delta-wing-body and a pyramidal lifting body with highly swept delta wings with trailing edge flaps, shown in Fig. 2.9b. As expected, Kaufman found that the flaps were effective in providing control moments across all angles of attack tested, with greater effectiveness when deflected into the incident flow. Kaufman defined the moment reference centre at 60% virtual root chord, and noted that the reduction of control authority with separation produced a strong pitch-up moment for these configurations.

Spearman [72] presents experimental and computational results for the control effectiveness of different controls on a blunt ogive cone-cylinder body at Mach numbers of 2 to 6.8. Two geometries with ACS were tested: wings with trailing edge flaps and all moving wings placed fore of a flare at the cylinder base. It was found that the trailing edge flaps were ineffective at producing normal force or pitching moment at Mach 6.8, but the all moving wings could still effect normal force increments despite losing some pitch control effectiveness.

Kontis [19] investigates the effects of strakes, jets and flares on the overall aerodynamics of a power law body and an elliptical cone, though this review will be limited to the results attained for the elliptical cone with and without stakes. The experiments consisted of an angle of attack sweep with no strake deflection, with forces measured with a 3 component force balance and surface flow visualised with an oil dot flow technique. As shown in Fig. 2.10, it was found that addition of strakes reduced the crossflow between the windward and leeward rays, increasing the slope of the $C_L - \alpha$ curve.

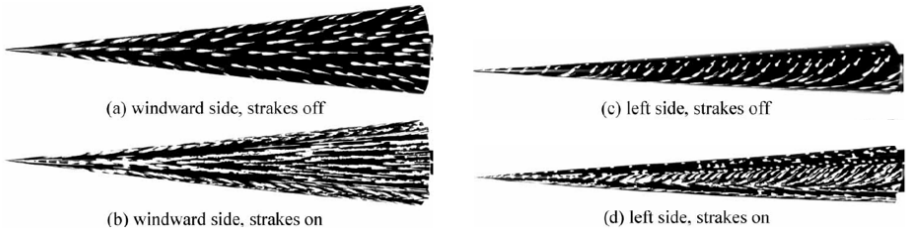

Fig. 2.10 Oil flow visualisation demonstrating reduced cross flow with addition of strakes to an elliptical cone [19]

2.3.2 Vehicle studies

The use of multiple ground test facilities in an attempt to characterise the full reality of hypersonic flight is well demonstrated by the development of the X-33. Murphy [7] presents an overview of the X-33 hypersonic aerodynamic characteristics, generated from wind tunnel testing in 4 facilities at NASA Langley Research Centre: 1) the 20-inch Mach 6 air tunnel, 2) the 31-inch Mach 10 air tunnel, 3) the 20-inch Mach 6 CF_4 tunnel and 4) the 22-inch Mach 20 Helium tunnel. Comparison of data arising from the two air tunnels (1 and 2), allowed for the effect of Mach number to be investigated, whilst the CF_4 tunnel was used to evaluate the significance of high temperature gas effects. Finally, the Helium tunnel was primarily used for assessment of initial prototypes owing to its unheated nature[1] permitting the use of rapidly prototyped wood and resin models. All 4 tunnels were blowdown facilities, with the CF_4 tunnel offering the shortest test times of approximately 24 seconds, and the other facilities producing test times on the order of minutes. Consequently, multiple angles of attack were able to be characterised in a single test run. All testing was performed in a pitch-pause manner, rather than a continuous sweep, with pauses lasting 3-5 s. The majority of data was attained with a single control surface deflected (i.e. body flap or aileron), with the principle of superposition being used to obtain the effective control authority with symmetric or asymmetric deflection. No testing was performed with both body flaps and elevons deflected due to time and resource constraints. It was shown that real gas effects were more significant than Mach number for longitudinal stability, with data from the CF_4 tunnel actually showing an increase in stability relative to data from the Mach 6 air tunnel - converse to the behaviour observed in the classical example of real gas effects for the space shuttle orbiter (in flight and the CF_4 tunnel). The results from the control effectiveness study, shown in Fig. 2.11a, are largely as expected, with effectiveness increasing with flap deflection and the vehicle showing sufficient trim moment capability with only 10° body flap deflection. However, control effectiveness for the body flaps becomes non-linear with angle of attack as a consequence of the interaction between the body flap shock and the vehicle bow shock, confirmed by CFD presented in Hollis [5] and shown in Fig. 2.11b. The shock-shock interaction resulted in a reduction in control effectiveness at higher angles of attack. The elevon control effectiveness exhibits much less non-linearity, though does display a reduction in effectiveness at higher angles of attack and flap deflections, attributed to flow separation upstream of the hinge line.

Holland [6] presents an overview of the experimental aerodynamics test program used in development of the X-43A vehicle (aka Hyper-X), with a particular emphasis on the

[1] Liquefaction was avoided through use of Helium as the test gas, which has a saturation temperature of approximately 2 K at the static pressures in the jet.

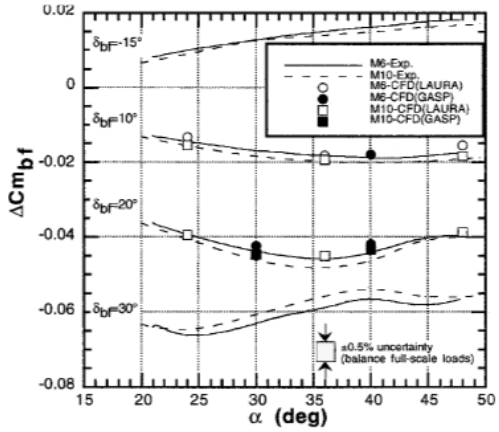

(a) Non-linear body flap trim moment from Murphy [7]

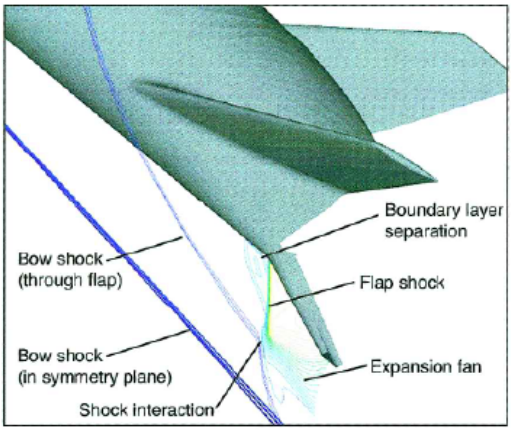

(b) CFD prediction of shock-shock interaction causing non-linearity [5]

Fig. 2.11 X-33 body flap trim moment non-linearities

control effectiveness across the flight envelope. Again, an exhaustive experimental campaign was performed - consisting of over 5800 wind tunnel runs using 15 models in 9 wind tunnels. Costs were minimised by designing models to be used in multiple facilities - often requiring a decrease in scale and creating challenges in resolving control surface interactions. Hypersonic tests were performed in 3 facilities: 1) the 20 inch Mach 6 air tunnel, 2) the 31 inch Mach 10 tunnel and 3) AEDC Von Karman Facility (VKF) Tunnel B at Mach 6, though no information on the Reynolds number in any of the tests is given. All tests were performed with fixed control effector deflections and utilised a 6 axis force balance. Whilst no details on the experimental procedure itself is given, it is expected that these were performed in a pitch-pause manner as the X-33 above[2]. The X-43 features two horizontal all moving wings functioning as elevons and two rudders for providing control. Before discussing the control effectiveness results, the nomenclature used in Fig. 2.12 must be discussed. These are presented in terms of elevator, aileron and rudder deflections, rather than wing positions themselves. Aileron deflections are defined by asymmetric deflection about a nominal elevator deflection (i.e. +5° aileron about 7.5° elevator position would actually consist of the left elevon at 5° and the right at 10°). It can be seen from Fig. 2.12a that the resultant aileron roll effectiveness is strongly dependent on elevator position, with a 70% increase in roll authority about the 7.5 degree nominal elevator deflection relative to the 0° nominal deflection. It can also be seen that control authority becomes non-linear with angle of attack for angles of attack greater than 4 degrees, though no explanation is given in the

[2]Especially given both tests utilised the 20 inch Mach 6 air tunnel

paper[3]. Holland also found that elevator effectiveness was dependent on rudder deflection, increasing with rudder deflection angles. Fig. 2.12b shows that the control authority provided by the rudders was found to decrease with angle of attack, as the hypersonic shadowing effect becomes more prevalent, with an almost complete lack of control effectiveness at an angle of attack of 10 degrees. Finally, it was also found that sideslip had minimal effect on control effectiveness[4].

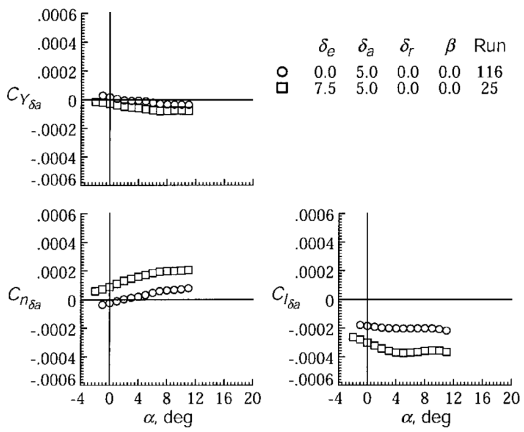

(a) Effect of elevator position on aileron control effectiveness

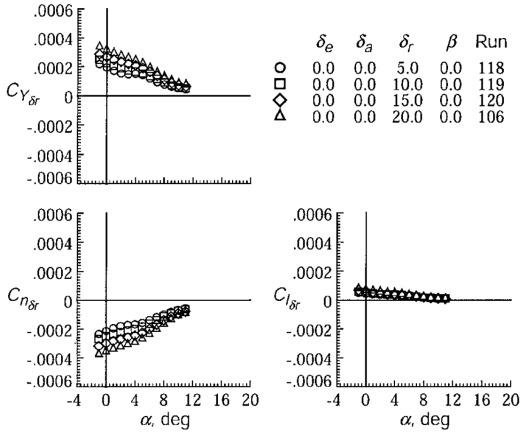

(b) Rudder control effectiveness

Fig. 2.12 Control effectiveness at Mach 6 for the X-43A [6]. Note: Aileron deflections are defined by asymmetric wing deflection about a nominal elevator deflection (i.e. +5° aileron about 7.5° elevator position would actually consist of the left wing at 5° and the right at 10°)

Gruhn [8] presents aerodynamic measurements of the Long-Term Advanced Propulsion Concepts and Technologies (LAPCAT) II small scale Mach 8 vehicle, performed in the Hypersonic Wind Tunnel Cologne (H2K) blowdown facility with a 6 axis DLR made force balance. Tests were performed at constant sideslip in a continual pitch manner. LAPCAT II is equipped with canards, ailerons and rudders. The experimental model was found to have a strong pitch down tendency, and at angles of attack $\leq -1°$, the combined canards and elevons were found to have insufficient control authority for trim, leading to a recommendation for increased control surface deflection and a change in centre of gravity location. Finally, the rudder was found to have sufficient control effectiveness to stabilise the laterally unstable vehicle, thought his naturally induced rolling moments. The elevons and canards were found to have sufficient control effectiveness to counteract the induced roll.

Van Hoffen [20] presents 1 Degree-of-Freedom pitch and roll experiments with an actuated canard slender body vehicle performed in Tunnel University South Queensland

[3]This should not be confused with the non-linearity in the transonic regime that caused the flight failure

[4]Consequently sideslip sensitivity was not included in the hypersonic aerodynamic database

(TUSQ). For these experiments, TUSQ was operated in Mach 4.5 atmospheric draft mode, permitting test times of up to 500 ms. The model utilised custom actuators to control the canards, and was attached to the sting by bearings. The angular rates of the model was measured with an onboard 6 axis IMU, and gyroscope readings differentiated to attain angular acceleration data. Experimental data is compared to steady state CFD, performed using Cart3D, in order to extract the static coefficients and hence control authority of the canards. Excellent agreement is shown between experimental data and the CFD data for "steady state", though, as shown in Fig. 2.13, there are significant differences in highly transient regions. This difference was attributed to either reaction moments associated with actuator deflections or unsteady aerodynamic effects. Though Van Hoffen notes the importance of Mach and Reynolds number scaling, no mention of reduced angular rates and whether dynamic derivatives can be reduced from the unsteady aerodynamic effects measured in the experiments is given.

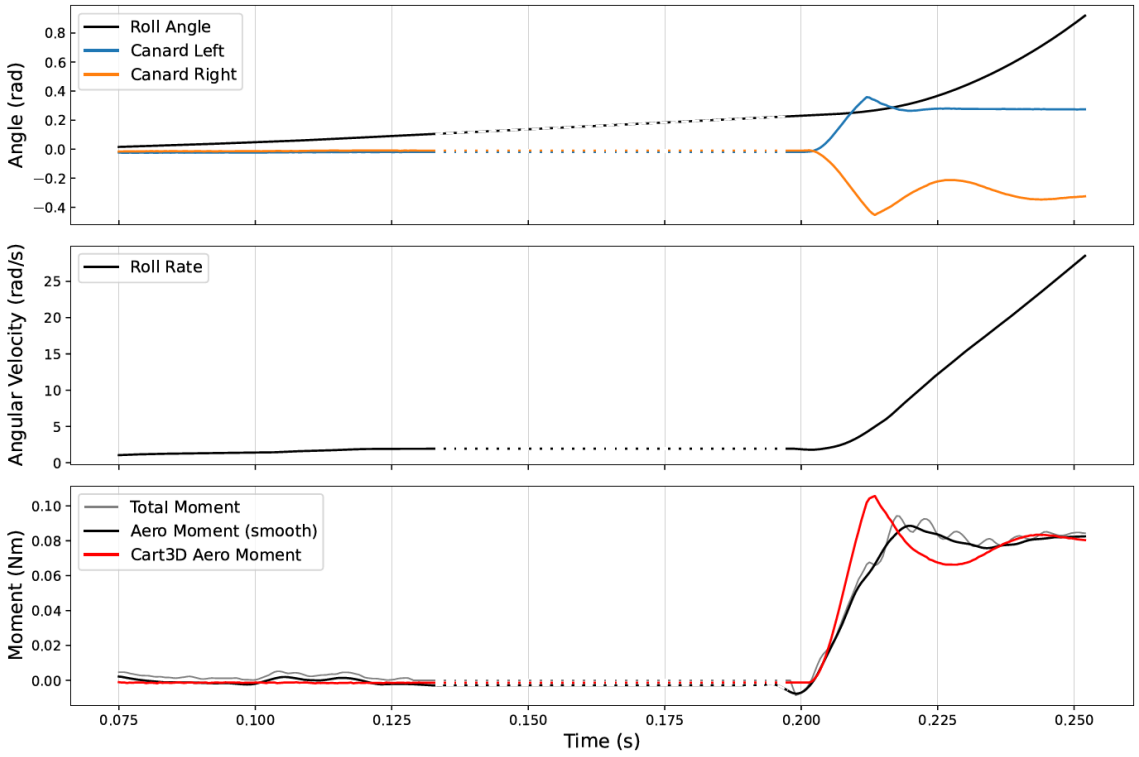

Fig. 2.13 Control effectiveness measured in dynamic experiments compared with steady state CFD for a canard controlled slender body model [20].

2.3.3 Shape Change

Existing literature on the effect of shape change has primarily been focused on how nose bluntness affects boundary layer transition [73–79], or vehicle stability and dynamics [80, 50, 81, 50, 47]; very little exists on the effect of shape change on control authority. Holden [82] presents a review of experiments performed in the LENS I reflected shock tube at Calspan-University of Buffalo Research Centre (CUBRC) investigating the effect of surface roughness and blowing on hypersonic vehicles. Included in the review is a brief section on the resultant effects on control effectiveness, the results of which are shown in Fig. 2.14. Unfortunately the details on the experimental setup are relatively sparse, but Holden states that both blowing and surface roughness work to thicken the boundary layer ahead of the flaps and significantly reduce the resultant control authority.

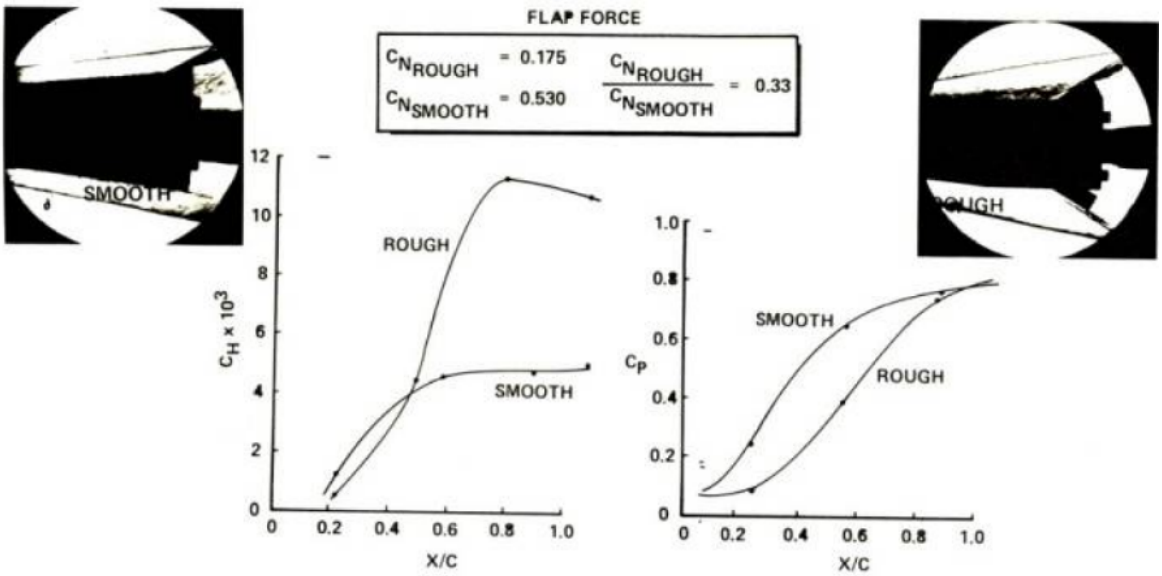

Fig. 2.14 Experimental results of the effect of surface roughness and blowing on flap heating and control effectiveness [82]

2.3.4 Summary

A summary of the reviewed papers is provided in Table 2.5. It can be seen that the majority of control effectiveness studies have been performed in blowdown facilities, where the flow duration permits multiple attitudes to be characterised in a single run, often in a pitch-pause methodology. Studies performed in impulse facilities are commonly static in nature, though dynamic techniques have been recently developed. It can be seen that for non-static control effectiveness tests to be performed, test durations on the order of 500 ms are required.

Table 2.5 Summary of control effectiveness studies reviewed

BD = Blowdown, Cont = Continuous, GT = Gun Tunnel, LPT = Light Piston Tunnel

AMW = All Moving Wing, BF = Body Flap, TEF = Trailing Edge Flap

Paper	Tunnel	M	Re_u $\times 10^6$ m^{-1}	Test Time	Geometry	Control Effector	Test Type
Rao	GT	8.2	6.69	5 ms	Delta Wing	flap	Static
Kontis	GT	8.2	9.2	5 ms	Elliptical cone	Strakes	Static
Van Hoffen	LPT[5]	4.5	3.26	500 ms	Slender body	Canards	1DOF (pitch/roll)
Oberkampf	BD	7.84	6.8	30 - 60 s	10 degree cone with slice	flap	Pitch-Pause
Spearman	BD	6.8	10.2	70 s	Blunt ogive cone-cylinder	AMW, TEF	Not mentioned
Murphy	4 off BD	6, 10, 20	1.2-22.5	$\geq$ 24 s	X33	BF, elevon	Pitch-Pause
Gruhn	BD	5	7.9	$\leq$ 30 s	LAPCAT II	Canard, aileron, rudder	Continuous pitch sweep
Holland	2 off BD	6	-	minutes	X-43A	AMW, rudder	Pitch Pause
Kaufman	Cont	8	3.6-10.8	-	Pyramidal lifting body	flap	flap deflection sweep

2.4 Ludwieg Tunnels

A wide variety of hypersonic wind tunnels exist around the world with test times varying between sub-microsecond in the highest enthalpy shock tunnel facilities to minutes in blowdown facilities. Perhaps the most common type of hypersonic facility is the Ludwieg Tunnel, first proposed by Hubert Ludwieg in the 1950's [83] as a method of cheaply producing steady hypersonic conditions. A summary of active Ludwieg Tunnels known to the author is given in Table 2.6. Several observations can be made from the table: 1) available test time ranges between 40-500 ms (though the lengths of each facility are not given, test time is closely linked with facility length), 2) there is an approximately even split between facilities that use diaphragms and fast acting valves for isolation of high pressure from vacuum prior to a shot, 3) the majority of tunnels are only operable in Ludwieg Mode and 4) of the tunnels listed, only 4 are configurable in a dual throat arrangement, and all of those feature a fast acting valve. Of the dual throat facilities, two of these (HLB and HTFD) use the dual throat to expand the Mach number range of the facility (more detail in Chapter 3), whilst Huazhong uses the dual throat nature to reduce the disturbances present in the freestream. The remaining facility, the Oxford HDT, is unique in the design of its fast acting valve in that the area through the valve is linear with the piston displacement. This allows the mass flow rate through the valve to be controlled and consequently enables the implementation of Extended Ludwieg Mode and Plenum Augmented Ludwieg Mode, as proposed by Jones[6] [85]. Both ELM and PALM will be discussed in greater detail in chapter 3, but to summarise they are both blowdown modes, offering over an order of magnitude increase in test time. For ELM this comes at the expense of test steadiness and PALM at the expense of total pressure and unit Reynolds capability. Testing in either ELM or PALM will provide sufficient test time for non-static control effectiveness studies to be performed (i.e. pitch-pause, control deflection sweep or fully dynamic) in the HDT.

[6]Jones did not propose a name for PALM. Rather the acronym was defined in Hillyer [84]

Table 2.6 Summary of Hypersonic Ludwieg Tunnels Around the World. Adapted from [86]

Name	Mode(s)	M	Re_u, $\times 10^6$ m^{-1}	Test Time, ms	Valve/Diaphragm	Throat
AFOSR Notre Dame Large Mach-6 Quiet Tunnel[7] (ANDLM6QT) [87]	LM	6	11	150	Fast acting valve	Single
Air Force Research Labs M6 [88]	LM, ELM	6.1	2.3-30.1	200	Diaphragm	Single
Boeing/AFOSR Mach-6 Quiet Tunnel (BAM6QT) [89]	LM	6	3.4 - 13.6	200	Downstream diaphragm	Single
California Institute of Technology LT (GALCIT) [90]	LM	4	5 - 25	100	Diaphragm	Single
Gas Dynamics Tunnel (GDT) [91]	LICH	6.85	6.3 - 40.7	300	Diaphragm	Single
Huazhong University of Science and Technology LT [92]	LM	6	10	60	Fast acting valve	Dual
Hypersonic Ludwieg Tube Braunschweig (HLB) [93]	LM	6	3 - 20	80	Fast acting valve	Single/Dual
Hypersonic Test Facility Delft (HTFD) [94]	LM	7 - 9	2.2 - 19.7	100	Fast acting valve	Single/Dual
Konkuk University LT (KULT) [95]	LM	4 - 6	10 - 1100	86	Fast acting valve	Single
LENS II Ludwieg Mode [96]	LM	3.5 - 7	0.5 - 33	320	Diaphragm	Single
RWG, Göttingen [97]	LM	5-6.9	5-50	300	Fast acting valve	Single

Continued on next page

[7]Currently not operational as a quiet facility

Continued from previous page

Name	Mode(s)	M	Re_u, $\times 10^6$ m^{-1}	Test Time, ms	Valve/Diaphragm	Throat
University of Arizona Mach Quiet 5 LT[8] [98]	LM	4.84	5.2 - 39.9	100	Downstream double diaphragm	Single
University of Maryland Mach 4 LT [99]	LM	4	2.5 - 24	40	Fast acting valve	Single
University of Maryland High Temperature LT [100]	LM	6.25, 8	1.73-43.7	80	Fast acting valve	Single
University of Oxford High Density Tunnel (HDT) [101]	LM, LICH, ELM, PALM	6 - 7	5-96	50 (LM)	Fast acting valve	Dual
University of Tennessee Space Institute Mach 4 LT [102]	LM	4	3 - 54	125	Diaphragm	Single
University of Tennessee Space Institute Mach 7 LT [103]	LM	7	-	350	Diaphragm	Single
University of Texas at San Antonio LT[104]	LM	7.2	200	100	Diaphragm	Single
Tunnel University of Southern Queensland (TUSQ) [86, 105]	LM, LICH, PALM[9]	6 - 7	5 - 30	500[10]	Diaphragm/Valve	Single/Dual

[8] Currently not operational as a quiet facility
[9] In development
[10] These test times are only available in LICH

2.5 Conclusions

After reviewing the literature pertinent to force measurements, control effectiveness studies and Ludwieg tunnels, the following gaps have been identified:

1. There is extremely limited literature on the resultant effect of shape change arising from ablation on resultant control authority.

2. Control effectiveness studies are typically performed in blowdown facilities, often using a pitch-pause technique to characterise multiple values of angle of attack in a single run, without contributions from dynamic effects. The only control effectiveness studies in impulse facilities have either been fully static (i.e. characterise a single attitude and control effector deflection per run) or fully dynamic (i.e. no pauses in model motion).

3. Ludwieg tunnels are one of the most common hypersonic facilities in the world, but their test time is typically limited by facility length. New modes of operation for Ludwieg Tunnels, ELM and PALM, are proposed as a promising method for increasing the test duration available in those facilities to enable multiple attitudes or control deflections in a single run.

4. Dynamic test techniques can be used for identification of static aerodynamic derivatives both with and without appropriate dynamic scaling and can allow for continuous resolution of control effectiveness across both attitude angles and control effector deflections. However, to date all dynamic tests relating to control effectiveness have been performed without scaling of reduced angular velocities or any attempt to characterise contributions from dynamic coefficients.

This thesis will use a sting mounted model, capable of both acceleration compensated force balance measurements and free-to-roll dynamic test techniques, in the Oxford High Density Tunnel to address these gaps. Whilst other test techniques, such as free-flight, would also be suitable, sting based experiments allow the full test duration to be utilised (rather than being limited by the duration model remains in the core flow), and consequently allows for more attitudes or control effector deflections to be characterised in a single test.

Chapter 3

Blowdown Operation of Ludwieg Tunnels

Preamble

A key requirement for improving the state-of-the-art for control effectiveness studies in Ludwieg Tunnels is to increase the test duration they are able to produce. This chapter details the theory behind and commissioning of two blowdown modes of operation for Ludwieg tunnels: Extended Ludwieg Mode (ELM) and Plenum Augmented Ludwieg Mode (PALM). This chapter consists of unpublished and unsubmitted work, written in manuscript format. A statement of authorship is given at the end of the chapter, and references are given at the end of the thesis.

Associated Publications:

- Jack Hillyer, Luke Doherty, Chris Hambidge, and Matthew McGilvray. Extension of test time in Ludwieg tunnels. 2022. [84]
- Jack Hillyer, Luke Doherty, Christopher Hambidge, and Matthew McGilvray. Enhancing the test time performance of Ludwieg tunnels. In AIAA SCITECH 2024 Forum, page 2754, 2024. [106]

Associated Appendices:

Appendix A presents supplementary PALM data from testing at Mach 5 and Mach 6.

Abstract

This paper presents the commissioning of two blowdown modes of operation in the Oxford High Density Tunnel (HDT) at Mach 7: Extended Ludwieg Mode (ELM) and Plenum Augmented Ludwieg Mode (PALM). ELM is a quasi-steady blowdown mode, producing a steady decrease in supply pressure to the facility nozzle, whilst PALM offers steady supply conditions at the expense of total pressure and Unit Reynolds number capability. This paper presents the theory behind the modes and implications of adding a plenum to typical Ludwieg Mode performance before presenting quasi-1D numerical simulations, experimental results and a performance map of the HDT operating in PALM. ELM has been commissioned across the full range of HDT's current operating pressures, whilst PALM has been demonstrated for 3 fill pressures: 14 bar, 30 bar and 55 bar. Test times in both modes were limited by facility unstart to at most 400 ms, greater than a factor of 10 improvement relative to Ludwieg Mode, though for the 14 and 30 bar PALM cases this came with a reduction of Unit Reynolds capability of 40% and 30%, respectively. The 55 bar PALM case demonstrated a test time of 160 ms for a 20% reduction in unit Reynolds number capability. Theoretical performance maps predict that operation in PALM can provide a factor of 10 improvement to the test time capability for HDT for all M7 unit Reynolds numbers run to date in the facility without any upgrades. Hence, this paper presents a significant improvement of the capability of the HDT to investigate unsteady and long duration flow phenomena relative to standard Ludwieg Mode operation.

3.1 Introduction

Extensive ground testing is used during the design of a hypersonic vehicle for two key purposes: 1) as a cheap, low-risk alternative to flight tests for determining vehicle characteristics and behaviour [107] and 2) in support of CFD studies via provision of validation data and investigation of un-modelled phenomena [108–110]. However, the hypersonic flight regime is inherently complex and a single wind tunnel is not capable of replicating all of the effects of hypersonic flight simultaneously. For this reason, ground testing is often performed in an

array of hypersonic facilities, each with their own limitations [13]. One limitation common to all hypersonic facilities is their intermittent operation: test times are limited to minutes at most and are typically inversely proportional to flow enthalpy [111]. Enthalpy matched, full scale, continuous hypersonic wind tunnels are not feasible due to high structural and thermal loads and total power required (order of GigaWatts) [12].

For short duration intermittent hypersonic facilities like those typically operated within Universities, the duration of the test flow directly influences the experiments that can be performed as it dictates which flow properties have established. The length of test time required for the flow to establish is typically measured in flow lengths - the length of time it takes for a packet of fluid to reach a location of interest on a model - as it inherently accounts for the size of the facility/model. It is well known that pressure requires approximately one flow length to establish, whereas skin friction and heat transfer require up to three flow lengths depending on the state of the boundary layer [112, 113]. Unsteady effects, such as separation and recirculation regions, require significantly longer to establish - for instance recirculation regions on backwards facing steps such as those behind scramjet injectors can take up to 140 flow lengths [114]. These longer establishment times can sometimes be accommodated in short duration facilities by reducing the size of the model, but this comes at the cost of model complexity and often a loss of spatial data resolution. Longer test time allows for larger models to be used (up to the blockage limit) and enables a wider range of unsteady phenomena, such as Fluid-Structural-Interaction, unstart of high speed inlets, or investigation of wake flows, to be investigated. However, the benefits of increased test time are not limited to unsteady experiments - force balance measurements are simplified as stress waves internal to the model have sufficient time to equilibrate, allowing manufacturer supplied static calibrations to be used [39–41]. Additionally, longer test times allow for multiple model attitudes to be characterised in a single run, reducing the total number of tests required to characterise a vehicle.

One common type of low enthalpy, short duration hypersonic facility is a Ludwieg Tunnel [83, 115]. These typically produce cold perfect gas flows, capable of simulating flight Mach and Reynolds number but not high temperature gas effects. A Ludwieg Tunnel generally consists of a barrel filled with high pressure gas connected to a nozzle via a fast-acting valve or a diaphragm. The test gas is typically pre-heated to avoid liquefaction as it is expanded to hypersonic speeds through the facility nozzle. In Ludwieg Mode, flow is initiated by rapidly opening a valve or bursting a diaphragm, resulting in a centred rarefaction wave travelling upstream. Steady supply conditions to the facility nozzle are attained until the rarefaction wave returns to the nozzle throat, resulting in a decrease in supply pressure. Unless the test is then terminated, the rarefaction wave reflects, and the process repeats. This results

in a classic Ludwieg trace consisting of several steady flow plateaus. The length of each plateau, t_{wr}, is given by the length of time it takes for the rarefaction wave to return to the valve/diaphragm:

$$t_{wr} \approx \frac{2L_{\text{Barrel}}}{a} \tag{3.1}$$

Where L_{Barrel} is the length of the facility barrel and a is the speed of sound of the gas in the barrel. For the Oxford High Density Tunnel, t_{wr} varies between 35-50 ms [101].

Traditionally, extension of test times in Ludwieg tunnels is achieved via an increase in facility length [116, 88], or addition of unheated sections of the Ludwieg tube, locally slowing the passage of the rarefaction wave [100, 117, 94, 93]. Jones [85] proposed two new modes of operation for Ludwieg Tunnels aimed at extending the test time: Extended Ludwieg Mode (ELM) and Plenum Augmented Ludwieg Mode (PALM), x-t and p-t diagrams of which are shown in Fig. 3.1. In ELM, the opening time of the valve is increased to equal t_{wr}, extending the rarefaction wave and resulting in a steady decrease in nozzle supply pressure. This sacrifices the steadiness of a LM plateau, but greatly extends the test duration. PALM requires the Ludwieg Tunnel to have a dual-throat arrangement, with a plenum between the barrel and the facility nozzle and the plug valve located between barrel and plenum rather than at the nozzle throat. The barrel is then operated in ELM and the valve opening is adjusted to balance the mass flow into the facility plenum with the mass flow through the nozzle. This produces constant supply pressure to the facility nozzle, greatly extending the available steady test time to be comparable to some blowdown facilities (without a large increase in size of the Ludwieg tunnel). However, this extension of test time comes at the expense of total pressure and unit Reynolds number capability. If higher unit Reynolds numbers are required, the tunnel must be operated in Ludwieg Mode.

Both ELM and PALM have previously been implemented in the HDT [84, 106], but were limited in implementation to low fill pressures (14 bar). ELM has been implemented by the US Air Force Research Lab (AFRL) [88], and work is being done to retrofit a plenum and implement PALM in the Tunnel University Southern Queensland (TUSQ) facility [105].

This paper presents an overview of the theory of extending test times in Ludwieg tunnels in Section 3.2, from how it is typically increased for LM operation to the theory of operation of the new modes. Section 3.3 then provides an overview of the experimental facility and instrumentation and Section 3.4 presents the setup of the numerical model used to validate understanding of the modes. Section 3.5 outlines the data reduction used for the experimental results presented in Section 3.6. Finally, a performance map is given in Section 3.7 and conclusions given in Section 3.8

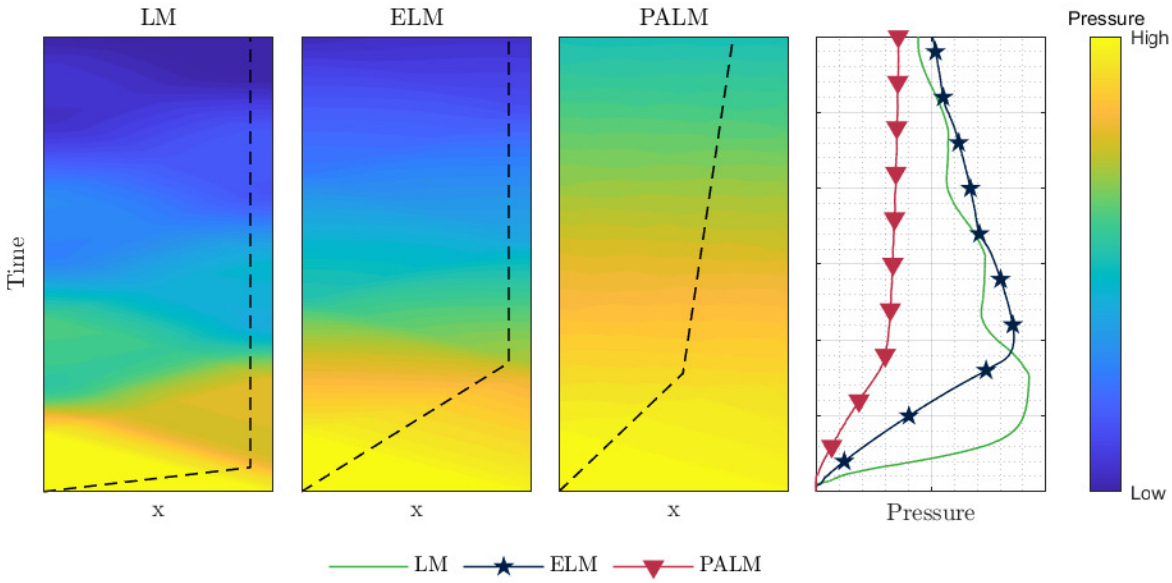

Fig. 3.1 x-t and p-t diagrams of a Ludwieg tunnel operating in LM, ELM and PALM, with valve openings overlaid with dashed lines on the contour plots. All generated with the L1D model discussed in Section 3.4

3.2 Extending Test Times

This section presents the theory behind extending the test time in Ludwieg Tunnels. It beings with a description of how test times are extended in the classic Ludwieg tunnel, before discussing the effect of adding a plenum to the Ludwieg tunnel on typical operation before concluding with the theory of operation of PALM.

3.2.1 Classic Ludwieg Tunnel

Fig. 3.2 shows a schematic of the simplest form of a Ludwieg tunnel, consisting of a barrel connected directly to the nozzle via a fast acting valve or a diaphragm. These facilities are typically relatively cheap to operate whilst providing steady test flows. Consequently, they are frequently used in Universities or research labs for generation of high quality aerodynamic data.

3.2.1.1 Ludwieg Mode

In this paper, the classical mode of operation is referred to as simply Ludwieg Mode (LM). As mentioned in Section 3.1, operation in LM can result in a supply pressure trace consisting of several steady flow plateaus. However, most Ludwieg tunnels are designed to shut down after the end of the first plateau, with effort being put into maximising its duration. The total

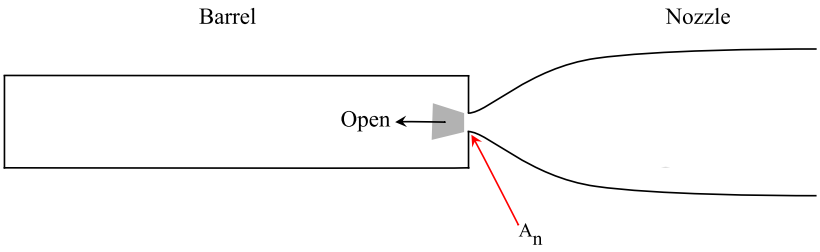

Fig. 3.2 Schematic of a classic Ludwieg Tunnel (omitting test section and dump tank)

pressure and total temperature during this plateau are given by Eqs 3.2 and 3.3 respectively, and the duration, t_{wr}, is given by Eq 3.4 [117]:

$$\frac{P_0}{P_{fill}} = \frac{(1+((\gamma-1)/2)M_t^2)^{\frac{\gamma}{\gamma-1}}}{(1+((\gamma-1)/2)M_t)^{\frac{2\gamma}{\gamma-1}}} \quad (3.2) \qquad \frac{T_0}{T_{fill}} = \frac{1+((\gamma-1)/2)M_t^2}{(1+((\gamma-1)/2)M_t)^2} \quad (3.3)$$

$$t_{wr} = \frac{2L_{\text{Barrel}}}{a}.\frac{1}{1+M_t}.\left(1+\frac{\gamma-1}{2}M_t\right)^{\frac{\gamma+1}{2(\gamma-1)}} \approx \frac{2L_{\text{Barrel}}}{a} \quad (3.4)$$

Where p is pressure and T is temperature of the gas in the barrel, with subscripts $fill$ and 0 denoting fill conditions and the conditions behind the expansion wave, respectively, γ is the ratio of specific heats of the test gas, M_t is the Mach number inside the tube, a is the speed of sound in the barrel and L_{Barrel} is the barrel length.

Increasing the duration of this plateau can be achieved by either increasing facility length, decreasing the speed of sound in the barrel or both. An increase in facility length can be achieved without an increase in laboratory length by addition of a bent section to the barrel[88], whilst a decrease in speed of sound can be attained by decreasing the temperature of the gas in the barrel, though this will impact the unit Reynolds number produced in the run. Recognising that the test gas only makes up a small portion of the gas inside the barrel (particularly if only running for a single plateau), tunnels can be designed to only pre-heat the section of the barrel that contains the test gas. The lower temperature section(s) of the barrel are typically physically lower than the high temperature barrel to avoid contamination of the test gas with the lower temperature barrel gas, and consequently the temperature profile in the barrel exhibits an almost step change. To minimise the reflection of the rarefaction wave at this temperature interface, the diameter of the unheated section is increased according to Eq 3.5:

$$d_{cold} = d_{hot} * \left(\frac{T_{hot}}{T_{cold}}\right)^{0.25} \quad (3.5)$$

Where d refers to the diameter, and T the fill temperature, of each section of the barrel.

Whilst these techniques have been employed with great success in numerous Ludwieg Tunnels (e.g. Hypersonic Test Facility Delft [94], Hypersonic Ludwieg Tube Braunschweig [93], University of Maryland High Temperature LT [100]), procurement of additional barrels for Ludwieg Tunnels can be an extremely expensive procedure and is ultimately constrained by the available laboratory space. Consequently, for existing facilities, it may be simpler to change how the facility operates in order to attain the test times required to investigate long duration phenomena.

3.2.1.2 ELM

ELM is a quasi-steady blowdown mode of operation, producing an approximately steady decrease in facility supply pressure. Implementation of ELM requires the facility to have a valve between the barrel and the nozzle throat, the opening of which must be controllable. Assuming a single stage valve opening, the exact form of the supply pressure trace is governed by the relation between time taken for the valve to open fully, t_{op}, and time taken for the rarefaction wave to return, t_{wr}:

$t_{op} << t_{wr}$: Ludwieg Mode. Supply pressure trace consists of several steady flow plateaus.

$t_{op} < t_{wr}$: Pseudo-ELM. The tail of the rarefaction wave is generated before the head returns, resulting in several steady flow plateaus of decreased duration.

$t_{op} = t_{wr}$: ELM. The tail of the rarefaction wave is generated as the head returns and becomes extended. Constant decrease in supply pressure attained, passing through the endpoints of each LM plateau.

$t_{op} > t_{wr}$: ELM, but the initial strength of the rarefaction wave, prior to its return to the nozzle throat, is reduced and so the initial gradient of supply pressure is lower. Hence, the supply pressure is higher at t_{wr}, but after this point falls at the same rate as the ELM trace. However, it is worth noting that as the valve acts directly at/on the nozzle throat, the valve area becomes the effective nozzle throat area (cf Fig. 3.2). Consequently, it is expected the nozzle will only produce flow at its designed Mach number once the valve is fully open (and the valve area is equal to the nozzle throat area).

x-t and p-t diagrams of a classic Ludwieg tunnel with each of these valve openings is shown in Fig. 3.3

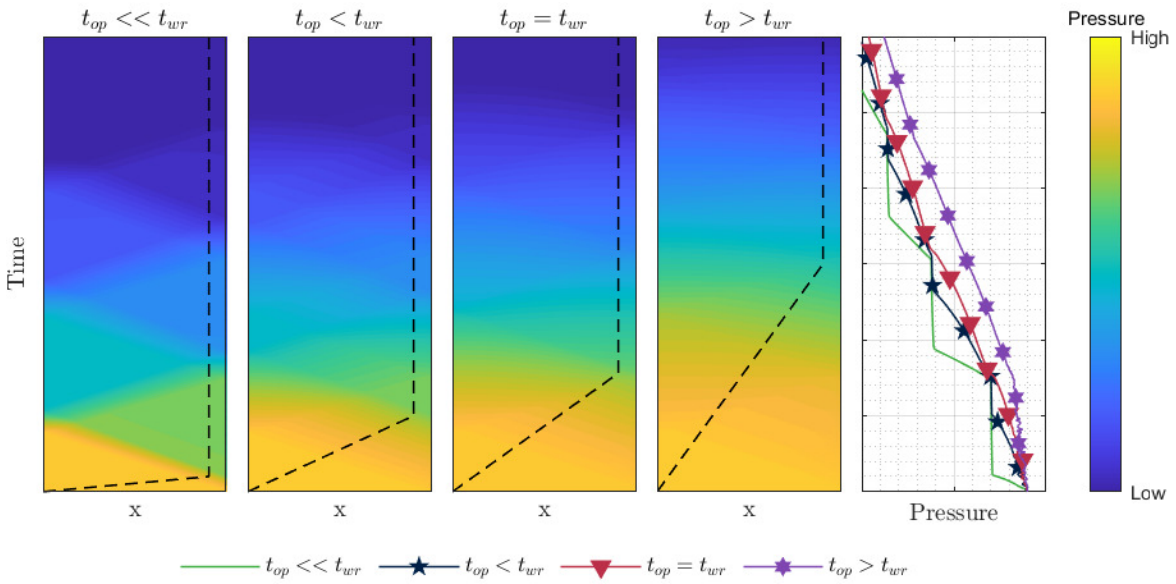

Fig. 3.3 x-t and p-t diagrams of a Ludwieg tunnel with single stage valve opening, changing opening time

3.2.2 Ludwieg Tunnels fitted with a plenum

Addition of a plenum region between the facility barrel and the nozzle throat enables the implementation of PALM, providing the fast acting valve acts on the upstream (barrel/plenum) throat (shown schematically in Fig. 3.4). However, before discussing the theory of PALM, the effect of adding a plenum on the performance of a Ludwieg tunnel in LM and ELM must be discussed.

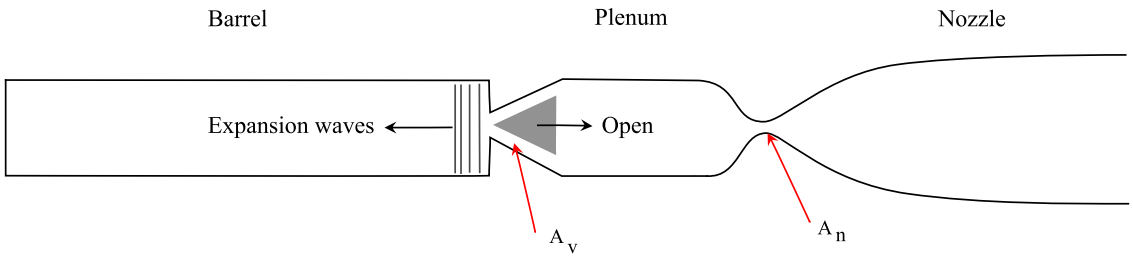

Fig. 3.4 Schematic of a dual-throat Ludwieg Tunnel (omitting test section and dump tank). A_v is the transient area through the valve as it opens

3.2.2.1 LM

The primary effects of adding a plenum to Ludwieg Mode performance are on the supply pressure to the facility nozzle and on the total temperature of the flow, with potential secondary effects on the test time. All of these effects are dependent on the ratio of areas between the nozzle throat and facility valve, defined here as α_ϕ:

$$\alpha_\phi = \frac{A_n}{A_v} \tag{3.6}$$

Where A_n is the area of the nozzle throat, and A_v is the effective area through the facility valve. For operation in LM, where the valve is opened as quickly as possible, the value of A_v can be taken as fixed and equal to the diameter of the valve throat.

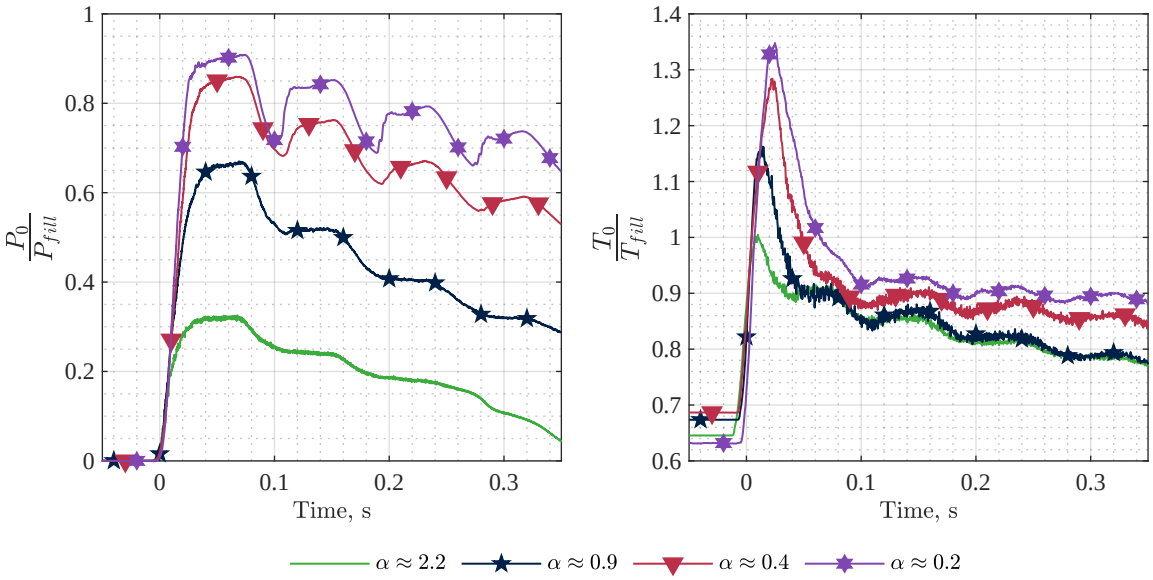

Fig. 3.5 Effect of changing nozzle throat area for a Ludwieg Tunnel fitted with a plenum (the Oxford High Density Tunnel, experimental data for different Mach number nozzles). The area of the upstream throat is consistent in all cases. Both supply pressure and total temperature 1 kHz lowpass filtered.

The effect of changing the value of α_ϕ on the supply pressure and total temperature of the flow is shown in Fig. 3.5. It can be seen that not only the magnitude but also the form of the supply pressure trace is dependent on α_ϕ. For $\alpha_\phi \approx 1$, the supply pressure trace is similar in form to a typical LM trace, with the exception of a start up period as the plenum fills. As α_ϕ decreases below 1, the peak supply pressure in the plenum increases due to the reduced mass flow out of the nozzle. This also has consequences for the form of the supply pressure trace, which now exhibits a transient increase after each return of the rarefaction wave, slightly reducing the duration of the plateau. Values of $\alpha_\phi > 1$ can begin to result

in difficulties regarding the choke point of the facility, which can move to the upstream throat. Depending on the head loss across the valve, the design of the plenum and the area ratio between the plenum and the nozzle throat, this can at best lead to shocks forming in the plenum, reducing the peak supply pressure attained in the test, and at worst prevent the facility nozzle from starting. Addition of damping materials in the plenum can aid in stagnation of the flow [118–120], expanding the nozzle throat diameters that a facility can accommodate and allowing for generation of consistent core flow diameters across a wider Mach number range.

The total temperature of the flow is mostly affected by the unsteady filling of the nozzle plenum at the start of the test, resulting in a transient increase in excess of the fill temperature. The magnitude and duration of this peak is also dependent on α_ϕ, with smaller α_ϕ resulting in both a greater magnitude and duration of the temperature peak. However, in all cases the total temperature will decay to an approximately steady state once steady supply pressures are achieved.

3.2.2.2 ELM

As with LM, the form of the ELM supply pressure trace is dependent on the value of α_ϕ, but, due to the slow opening of the valve, α now becomes a function of time with its value decreasing as the valve opens. This can present issues for larger nozzle throats, as the flow may now choke at the valve, reducing the peak supply pressure attained. However, once the valve opening is great enough for the choke point to switch to the nozzle throat, expected ELM behaviour can be attained.

Assuming there are no issues with the choke point of the facility, the ELM supply pressure trace will pass through the end of each LM plateau. Hence, it can be seen from Fig. 3.5 that decreasing the value of α_ϕ will decrease the rate of change of supply pressure in ELM. With regards to valve opening time and it's resultant effect on ELM supply pressure, addition of a plenum only affects the form of the supply pressure traces for the case where $t_{op} > t_{wr}$. This simply increases the rise time of the supply pressure, decreasing the peak supply pressure attained.

Finally, an interesting consequence of adding the plenum is the ability to only partially open the valve without affecting the effective nozzle throat area (and hence Mach number). In this case, the relations between t_{op} and t_{wr} discussed in Section 3.2.1.2 hold true, but the maximum supply pressure attained will be reduced. An x-t and p-t diagram of A Ludwieg tunnel operating in ELM with partial valve opening is shown in Fig. 3.6.

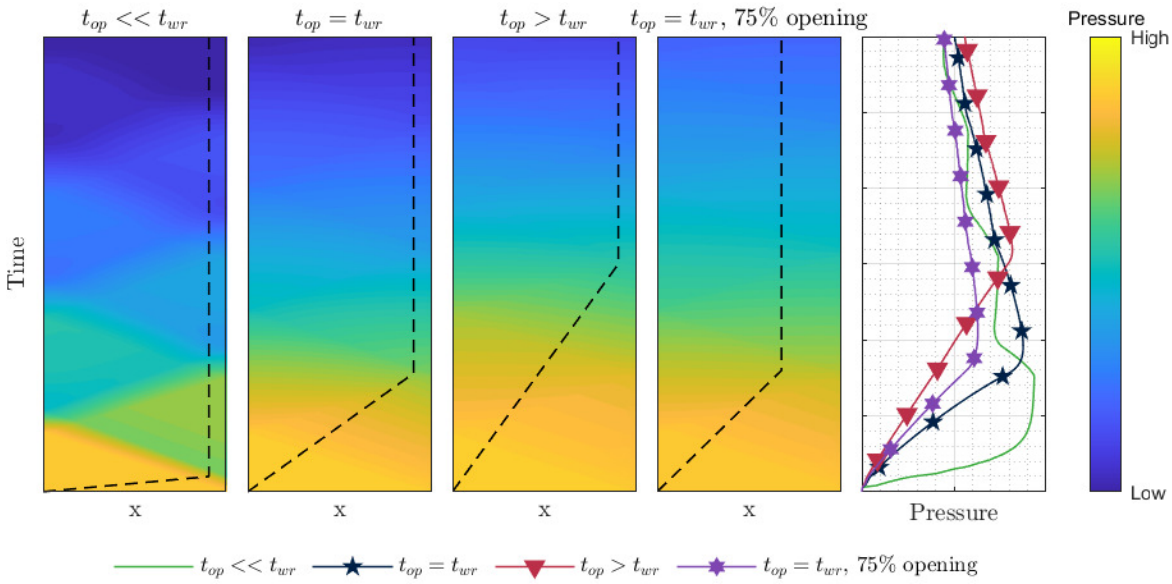

Fig. 3.6 x-t and p-t for a Ludwieg tunnel fitted with a plenum in LM and ELM. Also shown is an ELM case with partial valve opening

3.2.2.3 PALM

PALM is a metered implementation of ELM, allowing the operator of the facility to trade supply pressure/unit Reynolds number capability for greatly increased, steady test durations. It is the only mode of the three discussed here that depends on the facility having a plenum, and like ELM, also requires a fast acting valve at the upstream throat, the opening of which is tailored to achieve steady conditions in the plenum. The required valve opening is divided into two stages: the first, from time zero to t_{wr}, is the partial opening of the valve. As with ELM, the slow opening extends the rarefaction wave to produce a constantly decreasing barrel pressure, whilst the partial nature of the opening reduces the peak supply pressure attained. The second stage of valve opening is used to balance the mass flows in and out of the plenum. Steady conditions will be maintained until the supply pressure trace reaches the ELM trace that would be generated for that fill condition. As such, the ELM trace can be thought of as the bounding trace for PALM - all of the possible PALM conditions lie in the area underneath the ELM trace. Consequently, whilst there is only a single LM condition per facility fill pressure, there are theoretically infinite PALM conditions, each with a different peak supply pressure and test time, though in practice the PALM traces that can be attained are limited by feasible valve openings. The exact PALM condition achieved is a primarily a function of the valve opening at the end of the first stage - the lower the valve opening, the lower the supply pressure and consequently the greater the available test time. The steadiness of this test time is dictated by the speed of the second stage of valve opening - too fast, and

the supply pressure will rise to meet the ELM trace, too slow and the supply pressure trace will resemble an ELM trace with partial valve opening.

As with ELM, the slow opening of the valve required for PALM can lead to issues regarding the location of the choke point of the facility. This can be especially bad for PALM, where the required valve openings are slower and consequently more time is spent with larger values of α_ϕ. Therefore, operation in PALM may not be suitable for nozzles with large throat areas relative to the Ludwieg Tube diameter[1].

3.3 Oxford High Density Tunnel

The Oxford High Density Tunnel (HDT) is a Ludwieg tunnel located at the Oxford Thermofluids Institute, University of Oxford [121]. A schematic of the facility is given in Fig. 3.7, featuring a barrel of internal diameter 152 mm and length 17.35 m. The barrel is separated from the nozzle plenum by an upstream facing plug valve. The HDT features four operational nozzles, each with an exit diameter of 351 mm, covering the range of Mach 4 to Mach 7. The facility barrel can be heated to 550 K, and has a maximum pressure rating of 275 bar.

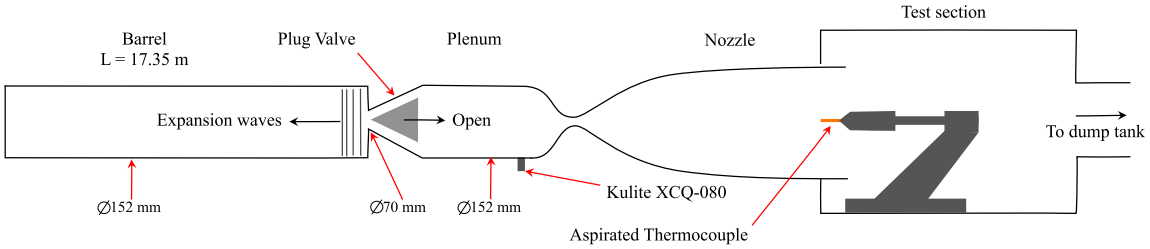

Fig. 3.7 Schematic of HDT. Adapted from [122]

3.3.1 Plug valve

A schematic of HDT's fast acting plug valve is given in Fig. 3.8. The plug valve is pneumatically actuated, with opening and closing achieved by venting and pressurising the volume behind the piston. A key feature of the HDT plug valve is the slots in the piston housing, exposed as the piston displaces, which provide the effective valve area variation required for PALM. The maximum area through the gas slots is greater than the area of the plug valve throat, and consequently there are two important piston positions for operation of HDT in PALM:

[1]Taking the case that the tube diameter is the limiting area for maximum upstream throat area

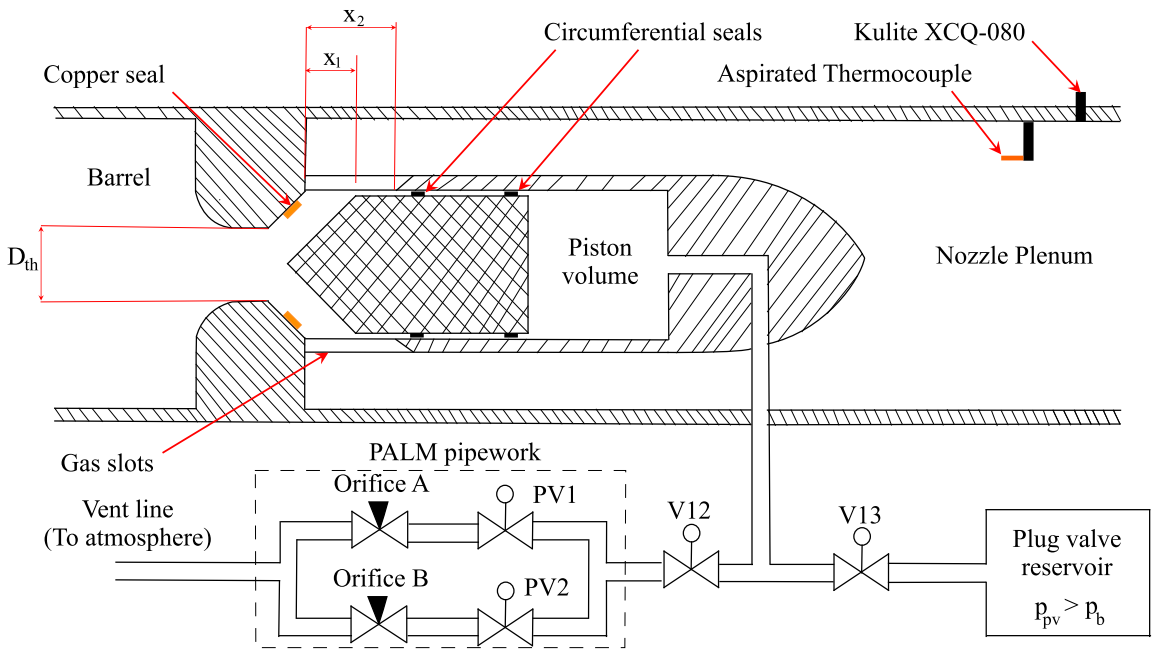

Fig. 3.8 Schematic of the HDT plug valve.

1. x_1: The exposed area of the gas slots is equal to the area of the plug valve throat

2. x_{wr}: Piston displacement at t_{wr}

When the piston is at x_1, the flow no longer sees a restriction from the piston, and the plug valve can be defined as fully open. If $x_{wr} < x_1$, the barrel pressure will constantly decrease, and PALM can be achieved.

The desired plug valve opening for PALM was achieved by installation of the PALM pipework in the plug valve vent line. This featured two branches, each featuring an interchangeable orifice and pilot operated solenoid. Actuation of each solenoid allowed the mass flow rate out of the plug vent to be modified, providing some control of the rate of plug valve opening - the greater the orifice size, the faster the plug valve motion.

3.3.2 Instrumentation

Nozzle supply conditions were measured using sensors mounted in the facility plenum. The supply pressure was measured using a flush mounted Kulite XCQ-080 transducer, and total temperature calculated from Aspirated Thermocouple (ATC) data using the processing outlined in [122, 123]. The Kulite was amplified with a Fylde FE-H379-TA differential amplifier, and the ATC with an Adafruit AD8495 amplifier. Both supply condition sensors

were recorded at 100 kHz. Uncertainties for each nozzle supply sensor are presented in Section. 3.5.

3.3.2.1 Pitot Rake

A pitot rake, mounted in the test section with probe tips at the nozzle exit plane, was used in these experiments to measure core flow extent and the duration of the useable test time. The Pitot rake was instrumented with Kulite pressure transducers at 7 radial positions (20 mm spacing), and ATC's at 2 radial positions, all recorded at 100 kHz. The Kulites were amplified with a Fylde FE-H379-TA differential amplifier and the Thermocouples a Fylde 351UA amplifier. Uncertainties for each pitot rake sensor are presented in Section. 3.5.

3.4 Numerical Setup

To validate understanding of the new modes and predict future performance capability, simulations of the HDT were performed using the L1D CFD code [124, 125]. L1D is a quasi-one dimensional Lagrangian flow solver used extensively in the design and modelling of hypersonic impulse facilities (e.g. shock tubes and Ludwieg tubes) where dominant flow processes are primarily one dimensional [126, 127].

3.4.1 Geometry

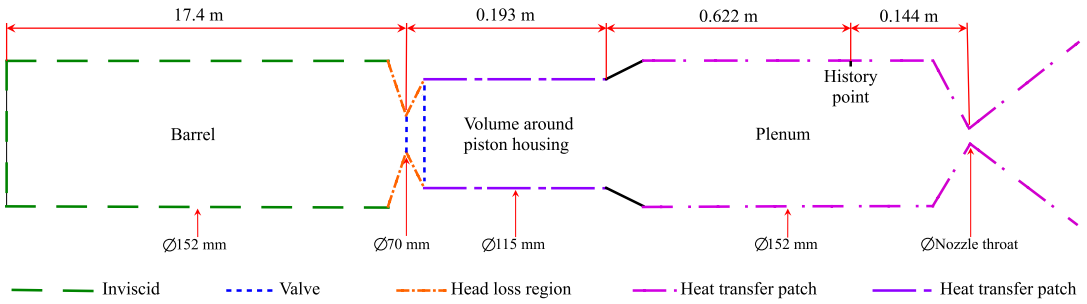

Fig. 3.9 Representation of the L1D geometry used to model HDT

The simulation geometry used in this work is shown in Fig 3.9. Due to the Lagrangian formulation of the code, L1D requires a relatively smooth variation in geometry between sections of differing diameters. Consequently, it is not possible to simultaneously match the volume, length and area distribution of the facility. For these simulations, the volumes and cross-sectional areas of the facility were preserved, whilst the length was not exactly

matched. Choosing to match the volumes and areas allows for the expansions through the facility to be properly modelled [128]. However, an exception was made for the volume around the piston housing, for which the maximum gas slot area was used. The maximum gas slot area is larger than both the equivalent area of the annular volume and the area of the plug valve throat. Using the maximum gas slot area for the volume around the piston housing enabled the full piston displacement to be modelled.

The simulation approximates the plug valve as two valves: the first is located at the plug valve throat, the second is at the maximum area of the gas slots. In the simulation, both valves are opened simultaneously with the same transient area variation. The downstream valve continues to open after the upstream valve is fully open. The use of two valves enabled the motion of the plug valve and the expansion of the barrel gas through the plug valve throat to be modelled. Using a single valve located at the plug valve throat only allows for the piston motion up to x_1 to be modelled. Similarly, a single valve located a the gas slots does not appropriately capture the expansion of the high pressure barrel gas through the plug valve throat in the initial stages of opening.

3.4.2 Tuning

The L1D model of the facility was tuned to match experimentally measured nozzle supply pressure and temperature traces (measured at the history point in Fig. 3.9) for facility fill conditions of 14 bar and 500 K. Tuning of the facility supply pressure was achieved by the addition of a head loss patch across the facility plug valve to represent the change in flow direction as the flow passes through the valve. The remainder of the facility barrel was modelled as inviscid, which allowed for the pressure drop caused by the rarefaction wave to be better matched. Total temperature tuning requires an accurate wall temperature along the length of the facility. The HDT features insulated heaters between the rear face of the barrel and upstream face of the plenum, so the temperature of this region was set to the fill temperature. Downstream of the heaters, the facility plenum and nozzle are uninsulated, and so the wall temperature was defined by a series of temperature patches, based on measurements of the plenum walls taken with a barrel fill temperature of 500 K. The total temperature was then tuned by a combination of two heat transfer patches, in which the local heat transfer co-efficient between the gas slug and the wall is increased. This allowed modelling of a geometry where the cross-sectional area is not accurately modelled by a tube. The first patch was added to the volume around the piston housing, where the flow passes through an annular area. The second heat transfer patch was located across the

facility plenum, where the heat transfer coefficient was increased to account for the larger temperature gradient.

The results of this tuning are shown in Fig. 3.10a, from which it can be seen that the tuned L1D model closely matches the experimental nozzle supply pressure trace, with two main discrepancies. The first is in the wave timings of the facility, in which the simulated arrival of the reflected head of the rarefaction wave precedes the experimental case. This a consequence of the L1D geometry not matching the physical length of the facility. This discrepancy becomes more apparent at later times (t > 240 ms), as the rarefaction wave reflects and the speed of sound in the barrel decreases. The second discrepancy is in the magnitude of supply pressure for plateau 5 onwards, which is underpredicted by the L1D. This is likely a consequence of the head loss tuning across the facility plug valve. The tuned model also closely matches the experimental total temperature trace, accurately predicting the total temperature on the plateaus, though the simulation shows more transient changes between plateaus. The cause for this is not yet known, but may be a consequence of ATC bandwidth.

To assess the robustness of the tuning to fill condition, the simulation was re-run for a 50 bar, 500K fill condition. The results are shown in Fig. 3.10b. It can be seen that there remains excellent agreement between simulated and experimental supply pressures, but the total temperatures are slightly over-predicted. Overall, the L1D model predicts the observed behaviour of HDT sufficiently well as to enable insight into how valve opening affects resultant supply pressure traces.

3.5 Data Reduction

This section presents an overview of the data reduction used in this paper for calculation of nozzle supply conditions and core flow extent. Uncertainties have been propagated through the data reduction equations using the jitter methodology [129], using a 5 point stencil and a 0.2% perturbation magnitude.

3.5.1 Nozzle supply conditions

Total temperature was calculated from ATC data, using the processing described in [122, 123]. To summarise, the total temperature is calculated by deconvolution of the measured temperature trace with an analytical step response model of the ATC. The step response is primarily a function of two parameters of the ATC: effective half-length and convective heat transfer coefficient, both of which may be dependent on the test condition. Determination of

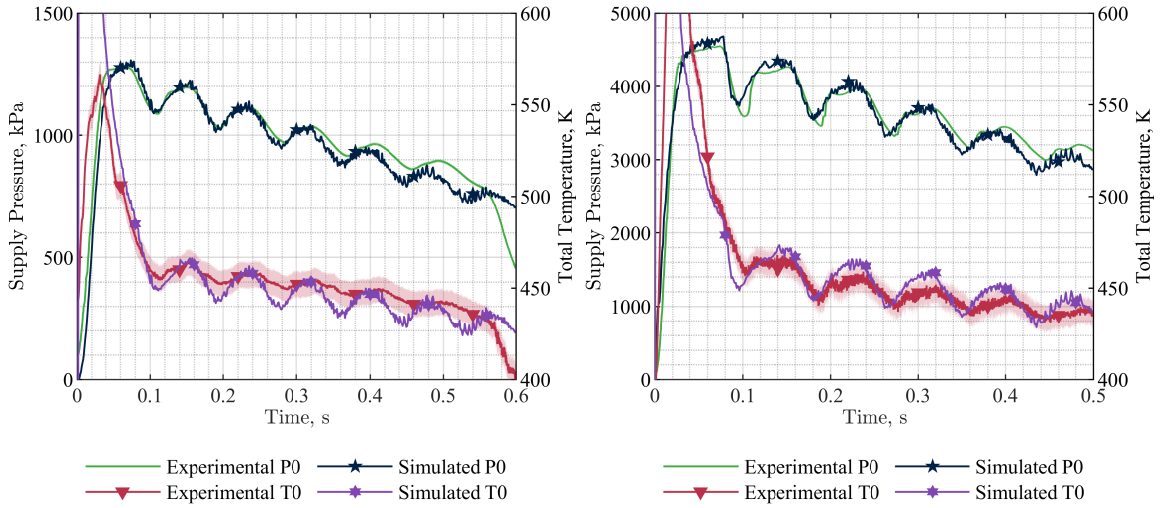

(a) Tuned Condition

(b) Off-tuned condition

Fig. 3.10 Comparison of the tuned L1D model with experimental data

these parameters requires 3 shots per test condition, each with different initial temperatures of the ATC. Assuming that the total temperature is identical across the three shots, the effective half length and heat transfer co-efficient of the ATC can be obtained, allowing calculation of the total temperature.

The plenum based ATC was not fitted for the ELM commissioning campaign, so total temperatures for that data are calculated from ATC data from the pitot rake, using an effective heat transfer coefficient and half length from a 14 bar ELM condition. The plenum based ATC was used in PALM commissioning and for the mode-to-mode comparisons. The LM total temperature was fully characterised, but for the PALM and ELM shots in that section the total temperature has been calculated using an effective heat transfer coefficient and half-length attained from characterisation of an 8 bar ELM condition. It should be noted that the plenum based ATC does not fully resolve the total temperature on the first LM plateau[2], but has shown to be consistent with ATC's installed on the pitot rake for $t > 0.1$ s.

For all campaigns, the Unit Reynolds Number was calculated assuming a constant Mach number, perfect gas and isentropic expansion through the facility nozzle, with viscosity calculated using Keye's relation [130]. The use of an assumed constant Mach number in the unit Reynolds calculation was motivated by the PALM commissioning campaign (and mode-to-mode comparisons), where both total temperature and supply pressure are measured

[2]This is likely due to the ATC being too far upstream of the nozzle throat to capture the transient increase in T0 as a result of unsteady filling of the nozzle plenum

in the facility nozzle plenum. Mach number being assumed constant (rather than being calculated from pitot pressure) permits the supply conditions to be calculated in isolation of facility unstart and hence permits the full capability offered by PALM to be compared to Ludwieg Mode[3].

Tables 3.1 presents a summary of the input uncertainties for the supply condition calculations. The value for the assumed constant Mach number was taken from the average centreline Mach number in that test, as measured by the pitot rake, and the input uncertainty magnitude was calculated as the RMS of the transient uncertainty in centreline Mach number.

Table 3.1 Summary of the input uncertainties to the supply condition calculations

Flow Property	P0	T0	M		
			LM	ELM	PALM
Sensor	Kulite XCQ-80	ATC	Assumed Constant		
Value	Measured	Measured	7.04	7.00	6.99
Uncertainty	$\pm$7000 Pa (0.1% FSO)	$\pm$15 K	$\pm$0.06	$\pm$0.071	$\pm$0.1

3.5.2 Radial Core flow extent

In this paper, the radial core flow extent is characterised with two parameters: 1) Mach number and 2) RMS pitot noise. Mach number was calculated iteratively using the Rayleigh-Pitot equation, given in Eq 3.7 [131]:

$$\frac{p_{02}}{p_{01}} = \left[\frac{(\gamma+1)M_1^2}{(\gamma-1)M_1^2+2}\right]^{\frac{\gamma}{\gamma-1}} \left[\frac{(\gamma+1)}{2\gamma M_1^2-(\gamma-1)}\right]^{\frac{1}{\gamma-1}} \tag{3.7}$$

Where p_{02} is the total pressure behind the shock, measured by the pitot sensor, p_{01} is the nozzle supply pressure, γ is the ratio of specific heats of the test gas, and M_1 is the freestream Mach number.

The RMS pitot noise was calculated for Kulite data in accordance with the processing in [101]. First, a $1-20$kHz bandpass filter was applied to the raw data to remove the contribution of mean pressure. The RMS of this bandpass filtered data was taken across a user defined test period, and then normalised by the mean pressure on that test period.

[3]The flow exiting the plenum remains choked on the nozzle throat and so supply condition measurements are independent of unstarted flow inside the nozzle

Table 3.2 Models and uncertainties of the Kulites in the HDT pitot rake

Radius (mm)	0	20	40	60	120	140
Model	XCQ-080	Unknown	XCQ-093	XCQ-093	XCQ-080	XCQ-080
Range	7 bar	1 bar	50 PSI	50 PSI	3.5 bar	3.5 bar
Uncertainty			$\pm 0.1\%$ FSO			

3.6 Results

This section presents experimental results from the commissioning of ELM and PALM in the Oxford High Density Tunnel with the Mach 7 nozzle. Data was attained in two campaigns: an ELM commissioning campaign and a PALM commissioning campaign, performed approximately 9 months apart. It begins with a comparison of the three modes in terms of supply conditions, test time and core flow extent, before presenting results from the commissioning of each mode, detailing conditions achieved. Unfortunately, due to issues experienced with the HDT heaters in each campaign, the data between the campaigns can not be directly compared. Consequently, all data is only compared to shots from the same campaign.

3.6.1 Mode to Mode Comparisons

3.6.1.1 Supply Conditions

Fig. 3.11 presents comparisons in terms of nozzle supply pressure, total temperature and calculated unit Reynolds number, along with their respective steadiness across the modes for a 14 bar fill condition. For clarity, uncertainties are only plotted over the useable test period prior to unstart, and all steadiness plots have been truncated at each individual shot's shutdown.

The top two graphs in Fig 3.11 show the supply pressures attained in each of the modes of operation. It can be seen that the LM trace consists of several quasi-steady plateaus, each of approximately 35 ms duration. The form of the LM trace is as expected for a value of $\alpha_\phi < 1$, with transient increases in pressure after the return of the rarefaction wave. This also has implications for the steadiness of the plateaus - all plateaus show a non-zero rate of change of supply pressure - however the plateau duration is short enough that the maximum deviation from the average pressure is less than 2.5%, with deviation decreasing for each subsequent plateau. It can also be seen that the strength of the rarefaction wave decreases with each reflection, as evidenced by the decreasing magnitude of pressure drop between

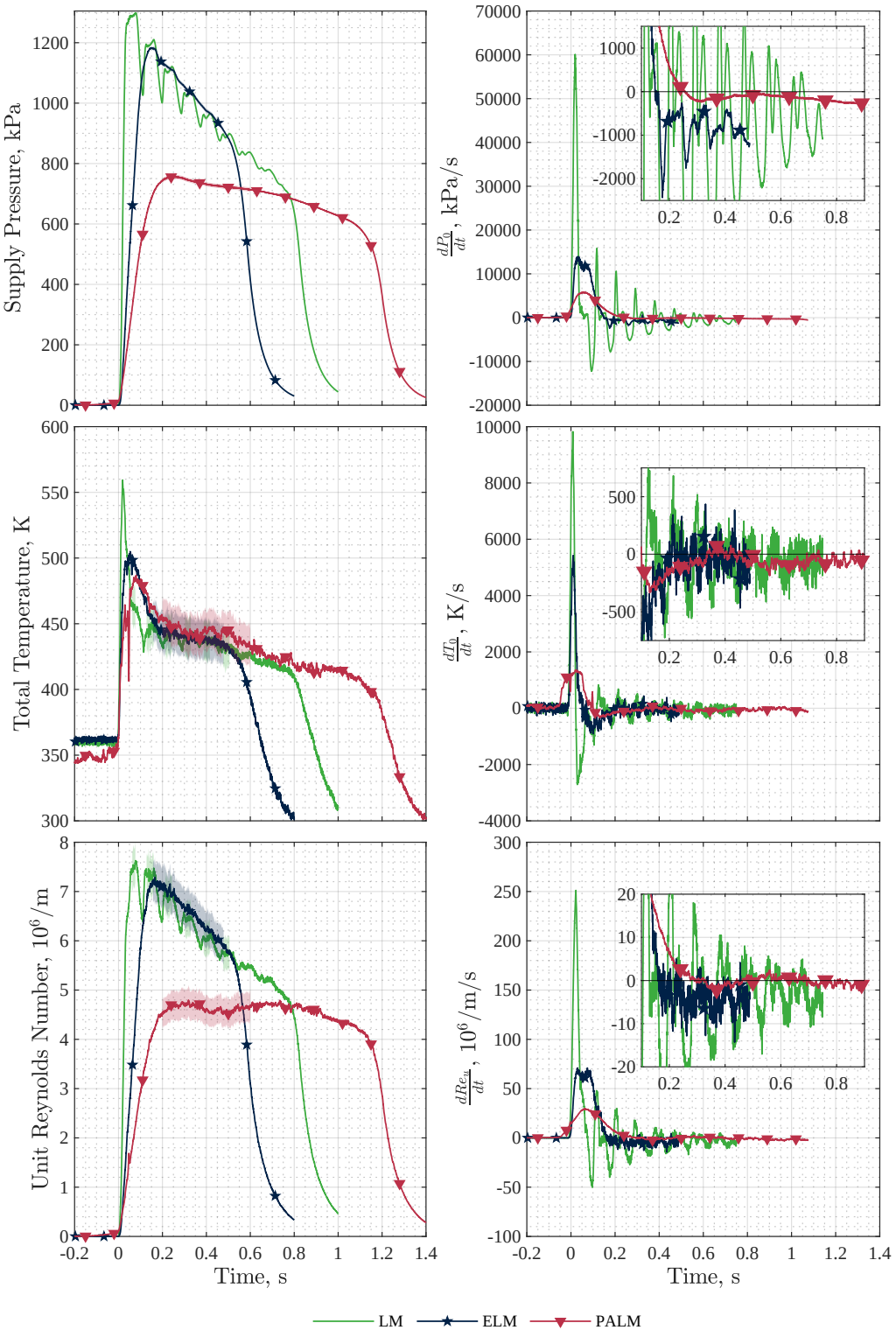

Fig. 3.11 Comparison of supply conditions across LM, ELM and PALM

plateaus. L1D simulations indicate that if this shot had not been terminated (by closing the plug valve), this trend would continue and the LM trace would decay to an ELM trace.

The ELM trace consists of a monotonically decreasing supply pressure across the test time, though the rate of change of supply pressure is not constant. The monotonic decrease shows that ELM has been achieved rather than pseudo-ELM, but the non-constant rate of change implies a non-ideal valve opening. The achieved valve opening can be inferred from the form of the supply pressure traces. It can be seen in Fig. 3.11 that the magnitude of $\frac{dp_0}{dt}$ locally peaks each time the head of the rarefaction wave returns, before decaying to an approximately constant value. This greater $|\frac{dp_0}{dt}|$ indicates that the head of the rarefaction wave is stronger than the tail, implying the piston motion consists of an initial jolt backwards followed by a slower, smoother remaining opening. This jolt is a consequence of "stiction" in the plug valve circumferential seals[4]. Regardless, the maximum deviation from an ideal ELM trace is approximately 1%. The PALM trace consists of a single test period, of approximately 900 ms duration, exhibiting a decreasing supply pressure at a significantly reduced rate relative to ELM. The gradient is not constant, but is smallest in magnitude for $0.35 < t < 0.5$ s and changes most significantly at approximately $t = 0.8$ s. The reduced magnitude is a result of a slightly better matched valve opening in that period, and the sharp change in gradient is a result of the PALM trace meeting the effective ELM trace.

A comparison between the total temperatures is given in the middle two graphs of Fig 3.11. In all 3 modes, there is a transient increase at the start of the test due to unsteady filling of the facility plenum. The total temperatures in LM and ELM are consistent after $t = 0.25$ s, corresponding to the third LM plateau, showing an approximately steady decrease in total temperature across the test. This decrease is a consequence of heat transfer to the unheated and uninsulated plenum walls. The PALM trace is consistent with the ELM trace for the duration of the ELM test, with the exception of a local trough at approximately $t = 0.05$s in the PALM trace. This is an artefact of the total temperature processing and is not expected to be physical. There is a slight deviation from the constant rate of decrease of total temperature in PALM for $0.35 < t < 0.5$ s as a result of the increased rate of plenum filling (and consequently decreased rate of change of supply pressure) in that period.

The bottom two graphs of Fig 3.11 present the calculated unit Reynolds number achieved in each mode. The LM and ELM traces follow the supply pressure across the shot, with LM producing steady plateaus and ELM a steady decrease. Operation in PALM demonstrates an almost constant Unit Reynolds number for $0.2 < t < 0.8$ s, culminating in a less than 3.5% deviation from average Unit Reynolds number across that period. This constant Unit Reynolds arises from the decay in supply pressure and total temperatures cancelling each

[4]See Section 3.6.2.3

Table 3.3 A comparison between the test times offered by LM and PALM for different percentage deviations from average unit Reynolds number

Mode	Test Time, ms			
	1% ΔRe_u	2% ΔRe_u	5% ΔRe_u	10% ΔRe_u
LM	10	35	35	35
PALM	45	165	750	900

other out. In future, it may be desirable to attain a steady decrease in supply pressure to match the decreasing total temperature and attain a constant unit Reynolds Number across the run[5]. As with the supply pressure traces, the Unit Reynolds number for PALM decreases at an approximately constant rate for $t > 0.8$s.

3.6.1.2 Test Time

The test time provided by a facility is dependent on the specific experiment being performed, with each experiment having different requirements for its performance indices in terms of steadiness or maximum permissible deviation from an average value. For HDT, a facility which is primarily used for force measurements, boundary layer transition and heat transfer studies, the typical performance indices for test time are unit Reynolds number and Mach number. Table 3.3 presents a table of how the test time available in PALM changes with different thresholds of deviation of unit Reynolds number. This shows that the full 900 ms duration of the PALM trace can be used if the unit Reynolds number is allowed to vary by up to 10% from its average value. However, the pitot pressure and Mach Number traces in Fig. 3.12 show that, currently, this full duration can not be used due to unstart of the facility nozzle, which limits the available test time in PALM to 400 ms. The Mach number traces across the modes are broadly consistent across the 3 modes, with the exception of the increased duration of the start-up period in ELM and PALM. Table 3.4 presents a summary of the demonstrated test time, as well as maximum deviations of supply conditions from average values for LM and PALM, and deviations from a straight line of best fit through the ELM data. Overall, it can be seen that PALM offers a factor of 25 increase in test time, for an approximately 40% reduction in unit Reynolds number relative to the 2nd LM plateau, though due to unstart the actual test time improvement is currently limited to a factor of 10.

[5]Operation in this manner would not be dissimilar to AEDC tunnel 9, where supply pressure is increased across the run to compensate for an increasing total temperature.

Table 3.4 Summary of demonstrated test time in each mode. All LM data has been calculated for the second plateau. Deviation has been calculated as deviation from average across the test period for LM and PALM, whereas ELM has been calculated as maximum deviation from a line of best fit through the data.

Mode	Test Time, ms		Mean Value			Max Deviation, %		
	Potential	Current	P_0, kPa	M	Re_u, $10^6 m^{-1}$	P_0	M	Re_u
LM	35 (x8)	35 (x6)	1196	7.04	7.32	1.2	1.8	1.9
ELM	320	320	1044	7	6.6	1.1	0.7	2.8
PALM	900	400	732	6.99	4.6	3.5	0.8	3.4

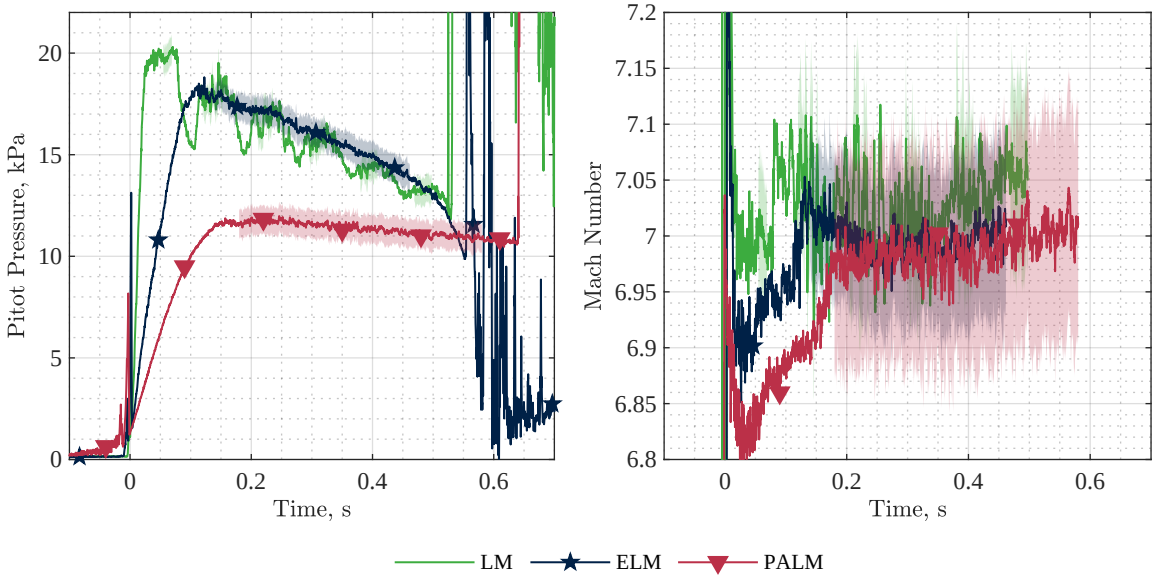

Fig. 3.12 Left: Pitot pressures showing unstart of the facility nozzle. Right: Mach number traces across the 3 modes

3.6.1.3 Radial Core Flow Extent

Radial core flow extent can be characterised by inspection of two parameters: 1) Mach number and 2) RMS pitot noise, both shown in Fig 3.13. It can be seen that both the Mach number and the RMS pitot noise distributions are consistent across the modes, indicating, as expected, that operation in ELM and PALM has no effect on the radial extent of the core flow. In all cases, the RMS noise increases significantly at $R = 140$mm, though the Mach number stays within 2% of its average across the core flow. This indicates that the probe at $R = 140$mm is likely at the edge of the core flow in all 3 modes, demonstrating a core flow diameter of $240 < \phi < 280$ mm. For all modes, the values for RMS pitot noise appear to be consistent with those in other hypersonic facilities [132, 133].

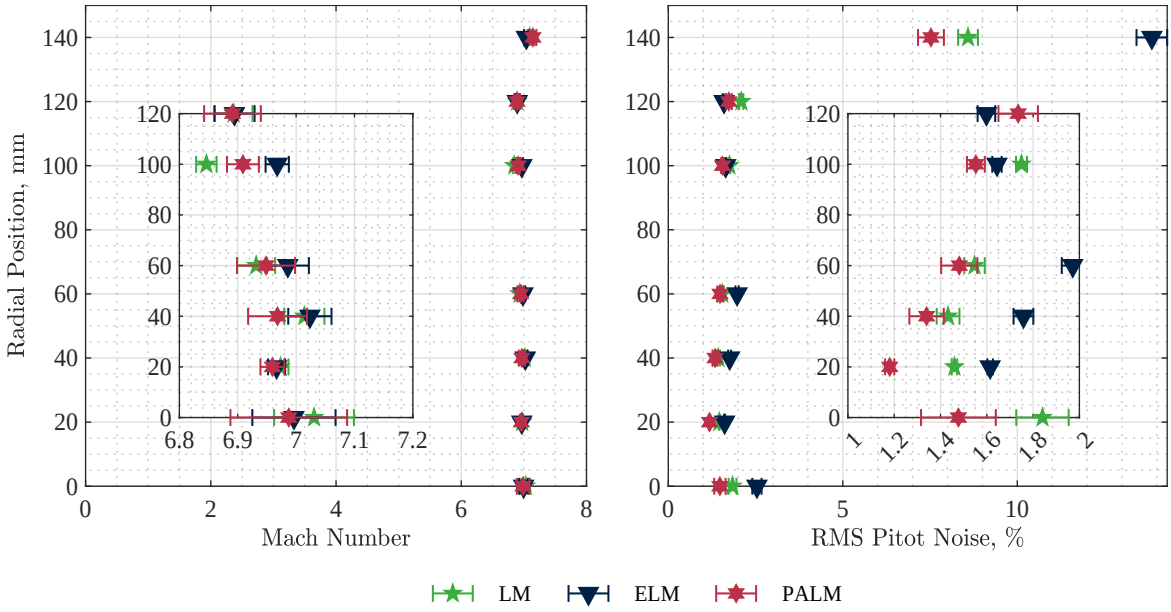

Fig. 3.13 Core flow comparison

3.6.2 ELM commissioning

This section presents results from the commissioning of ELM at Mach 7. It presents the range of supply pressures and unit Reynolds numbers ELM has been commissioned over, discusses the size of the core flow and the repeatability of the mode.

3.6.2.1 Supply Conditions

Fig 3.14 presents the range of supply pressures and unit Reynolds numbers achieved during ELM commissioning, with Unit Reynolds number traces truncated at the end of the useable test duration. All have identical setups in terms of PALM pipework and associated timings. Similar to the ELM trace in the Section 3.6.1.1, all ELM traces show a non-ideal valve opening arising from stiction in the plug valve seals. Each shot features a slightly different duration - this is a result of the plug valve being closed at different points and independent of being operated in ELM. As expected, the unit Reynolds traces follow the supply pressure traces, though the unit Reynolds number traces are slightly steadier as a result of decreasing total temperature. Overall, it can be seen that ELM has been demonstrated across fill pressures of 15 to 65 bar, and fill temperatures of 500K and 550K. It is expected that ELM will be able to be implemented at any M7 condition, though the test time is currently limited by facility unstart to 400 ms.

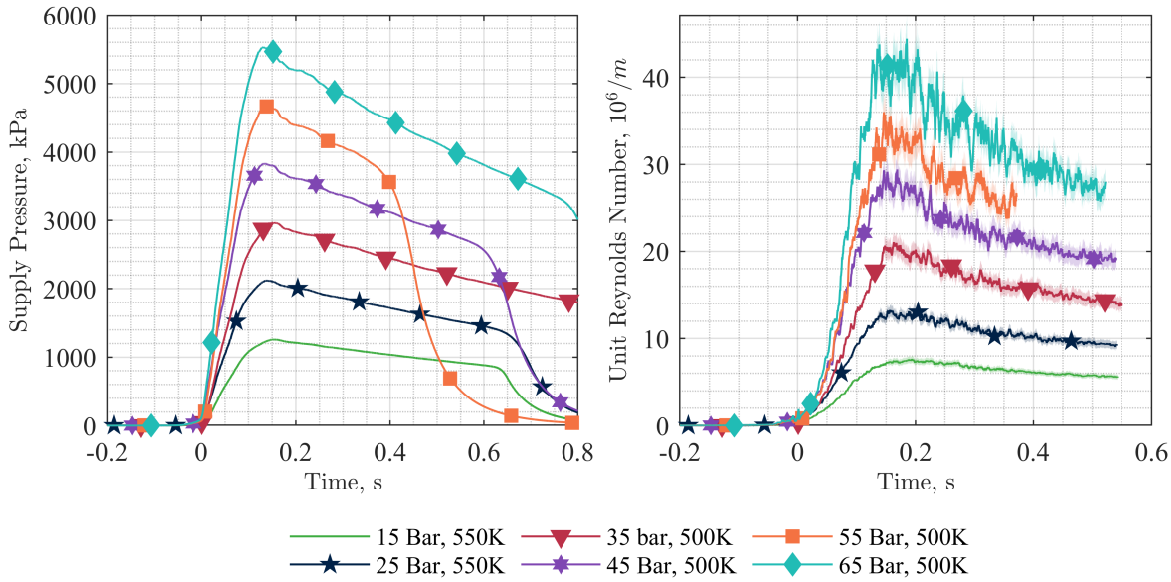

Fig. 3.14 ELM supply conditions

3.6.2.2 Radial Core Flow Extent

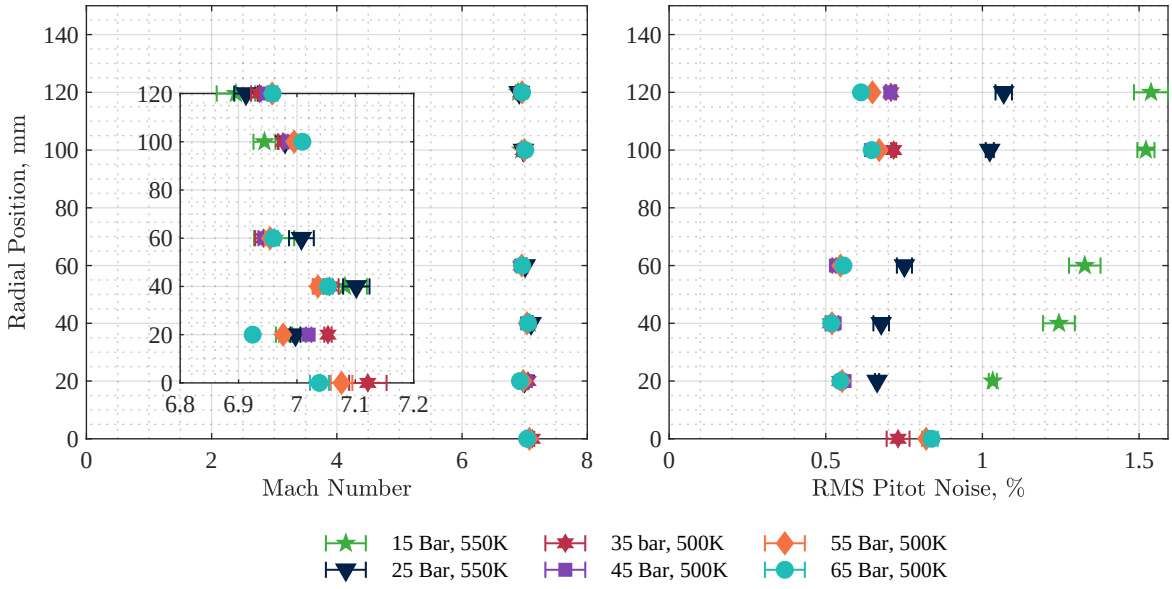

Fig. 3.15 Core flow in ELM

Fig. 3.15 shows the core flow distribution in ELM in terms of radial distributions of Mach number and RMS pitot noise. Unfortunately, the probe at $R = 140$mm was not functional for the ELM commissioning campaign. Regardless, it can be seen that the Mach number is consistent to within 2% across all fill pressures shown. Additionally, the RMS pitot noise is

consistent for $p_{fill} \geq 35$ bar, but increases in magnitude for the lower fill pressures. This is to be expected as the average supply pressure for these conditions is much lower.

3.6.2.3 Repeatability

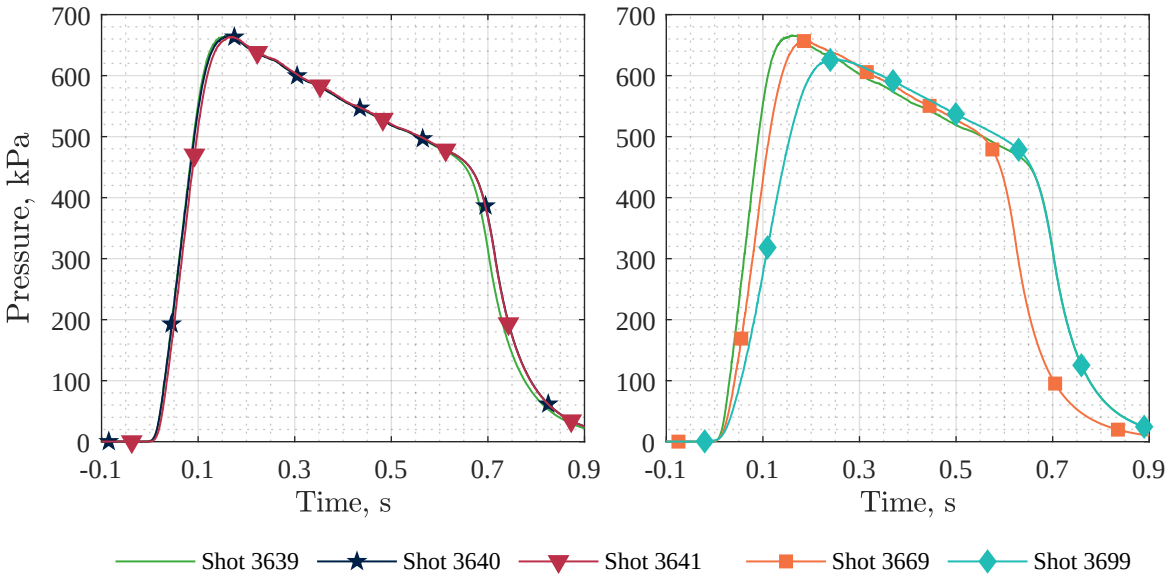

Fig. 3.16 Repeatability of ELM

Fig 3.16 presents data on the repeatability of ELM, both on a sequential and non-sequential shot-to-shot basis. It can be seen that ELM exhibits almost perfect sequential shot-to-shot repeatability, producing near identical supply pressure traces[6]. However, for non-sequential shots, the repeatability is slightly worse - later shots exhibit both a longer rise time and a smoother decay of supply pressure. This is caused by degradation of the circumferential seals on the plug valve piston. As these degrade, the stiction reduces, resulting in a lower differential pressure being required for the piston to being to move and consequently a slower, smoother valve opening.

3.6.3 PALM commissioning

This section discusses the effect of PALM pipework orifice diameters on the resultant supply pressure traces. It should be noted that these orifice sizes are specific to the facility and this implementation of PALM, so are presented here for clarity of discussion rather than as guidelines for other facilities.

[6]This is consistent with behaviour in LM

3.6.3.1 Variation of first stage orifice

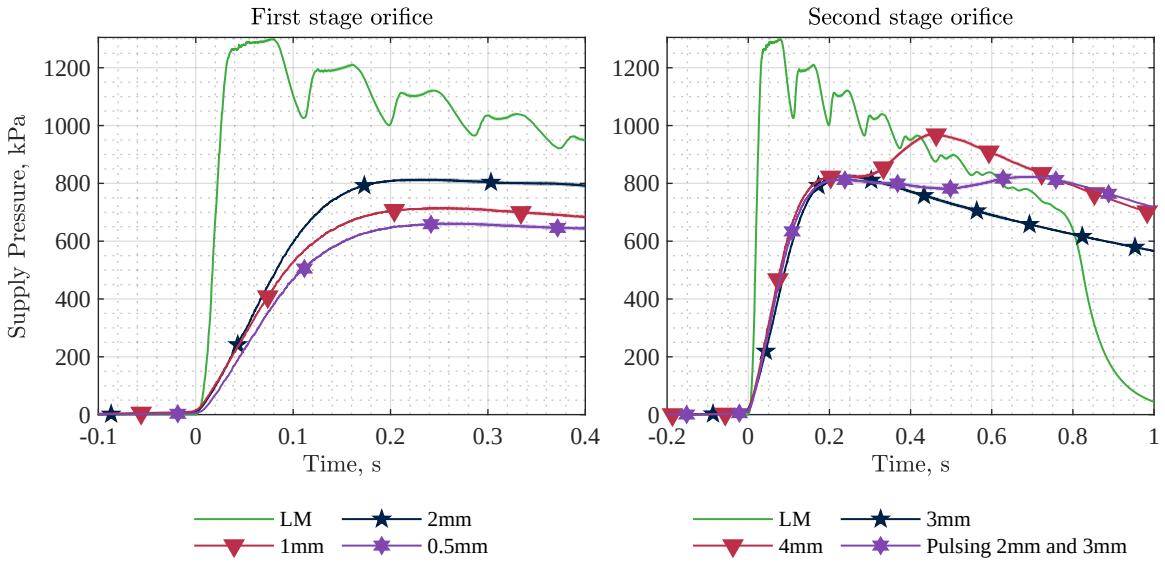

Fig. 3.17 The effect of changing valve opening on resultant supply pressure

The left hand figure of Fig 3.17 presents experimental results from varying the orifice diameter in the first stage. Decreasing the orifice diameter restricts mass flow from behind the plug valve, resulting in a smaller valve opening at the end of the first stage and subsequent lower peak supply pressure. However, it can be seen that there are diminishing returns on the decrease in supply pressure with decreasing orifice diameter. This is, again, a consequence of the stiction in the plug valve seals preventing lower first stage valve openings from being attained.

3.6.3.2 Varying second stage orifice

The right hand figure in Fig 3.17 shows a comparison between 3 PALM shots with different orifices being used in the second stage. It can be seen that for the 3mm orifice case, the second stage opening of the valve was too slow, providing similar behaviour to an ELM case with partial valve opening. Conversely, the 4mm orifice results in a second stage motion that is too fast, causing the supply pressure to increase until it meets, and subsequently follows, the ELM trace. Unfortunately, the available orifice sizes in this campaign were too discrete to allow for a single orifice to attain a tuned PALM condition. Consequently, the steadiest PALM trace was achieved with pulsing of the PALM valves to approximate the orifice required for tuned second stage motion. This has an impact on the overall steadiness of the supply pressure, culminating in a deviation of approximately 13% from the average

pressure across the plateau. It expected that a steadier plateau can be achieved with improved control of plug valve motion.

3.6.3.3 Repeatability

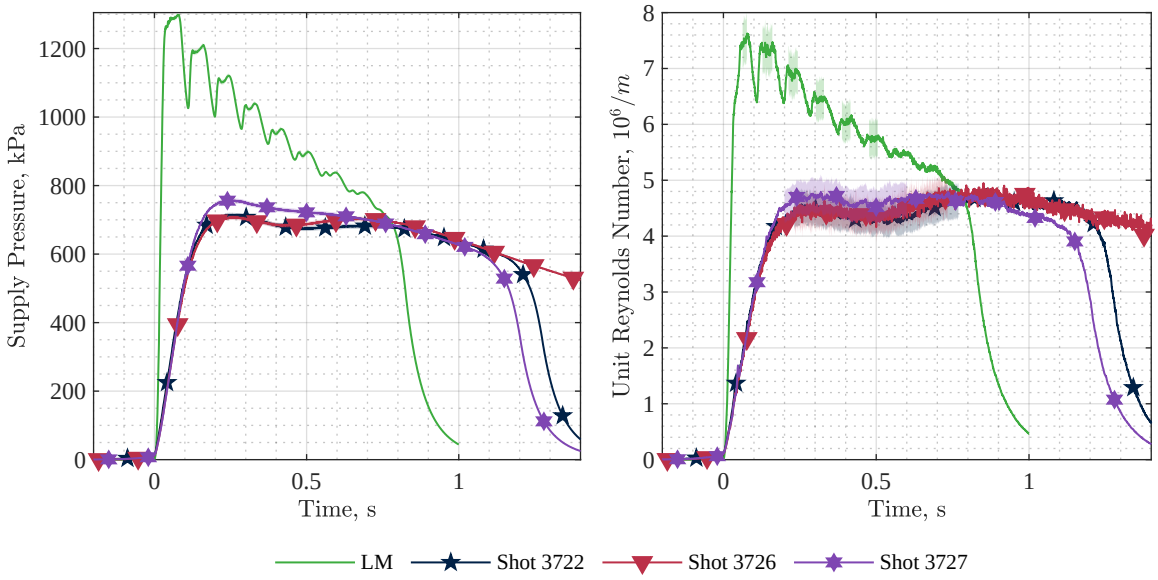

Fig. 3.18 Shot-to-shot repeatability of PALM

Fig. 3.18 shows the supply pressures and unit Reynolds numbers from 3 repeat shots with identical setup. It can be seen that shots 3722 and 3726 show excellent repeatability - with supply pressure traces both having a very similar form - but shot 3727 exhibits a slightly different form. The cause of this is likely day-to-day variability in the state of the circumferential seals of the plug valve piston, as shot 3727 was performed on the day after the other two shots. For this reason, noting the dependence of the total temperature trace to the form of the supply pressure trace, a probe capable of measuring total temperature in a single shot may be worth developing. Regardless, it can be seen from Fig. 3.18 that the unit Reynolds traces are repeatable within the uncertainty bounds, resulting in a less than 5% deviation between the average unit Reynolds numbers between the shots.

3.6.3.4 Increasing Fill Pressure

Given that the fundamental operating principle of PALM is to trade supply pressure for test time performance, it is highly desirable to increase the facility fill pressure to compensate. Fig 3.19 shows a comparison between LM and PALM for fill pressures of 30 and 55 bar. No experimental data is available for LM at 30 and 55 bar in this heater configuration, so the

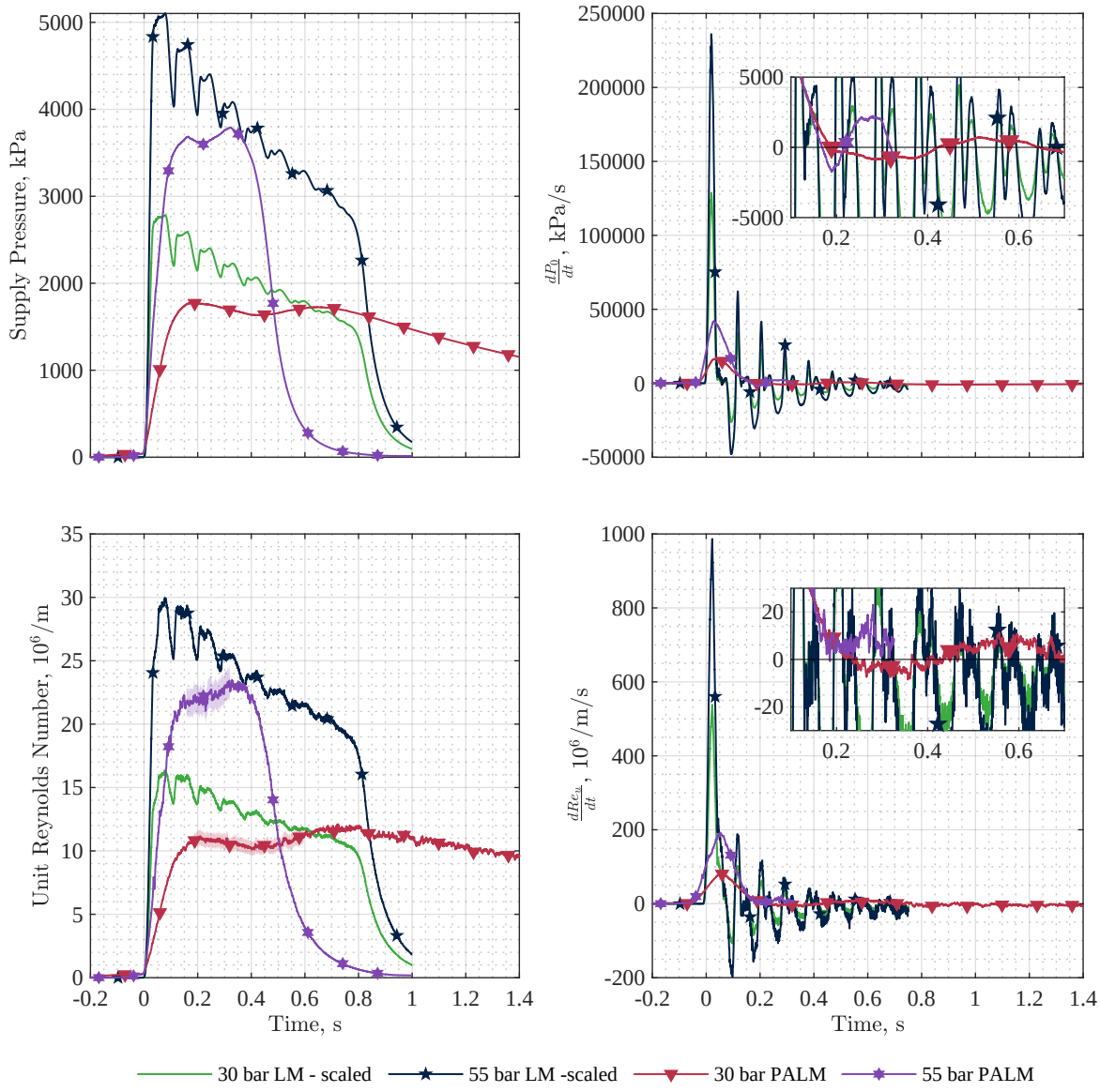

Fig. 3.19 Comparison of supply conditions in PALM with increasing fill pressure. Total temperature is not shown as this is assumed independent of fill pressure during scaling

LM data is scaled from a 14 bar LM shot attained during this campaign. It can be seen that both PALM traces have a non-ideal second stage opening, evidenced by a non-steady supply pressure and unit Reynolds number. Even so, it can be seen that PALM is comparable, if not better, to a LM plateau in terms of steadiness, and produces a significant increase in available test time.

Fig. 3.20 shows the core flow distributions for PALM with higher fill pressures. This data is consistent with the ELM commissioning (cf Fig. 3.16) in that the Mach number and RMS pitot noise distributions are largely similar across fill pressures, with RMS pitot noise

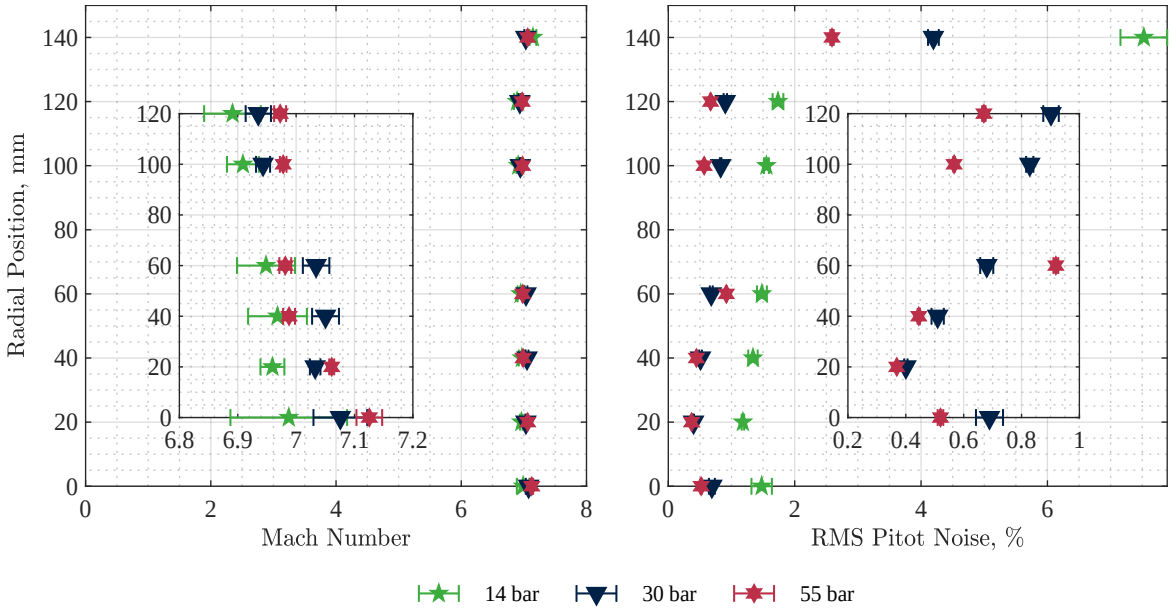

Fig. 3.20 Core flow comparison

increasing with decreasing fill pressure. Finally, Table 3.5 presents a summary of the PALM conditions attained during this commissioning. For a 14 bar fill, operation in PALM has been demonstrated to potentially extend test times by a factor of 25, for an approximately 40% reduction in unit Reynolds number capability, though in practice this was limited to a factor of 10 improvement by facility unstart. For a 30 bar fill condition, the improvement in test time was again limited to a factor of 10 from a factor of 15, with a 30% reduction in unit Reynolds capability relative to LM. For a 55 bar fill condition, a factor of 5 increase in test time was demonstrated for a 20% reduction in unit Reynolds number. In all cases, the PALM supply pressure and Unit Reynolds number were steadier than the Ludwieg Mode plateaus. Hence, operation in PALM has offered a increase in the available test time across a range of unit Reynolds numbers.

Table 3.5 Comparison of average supply conditions and test times attained in PALM commissioning

Fill Pressure, kPa	Average		LM equivalent fill, kPa	Test Time, ms	
	P_0	Re_u		Demonstrated	Potential
1400	7.35	4.6	860	400	900
3000	16.9	10.6	1990	400	600
5500	36.7	22.2	4320	161	161

3.7 Performance map

This section presents the potential performance of the HDT operating in PALM in terms of unit Reynolds number and test time achievable based on numerical simulations. It begins with the theoretical maximum, before discussing practical limitations and their effects on the resultant performance. The section concludes with some recommendations for future upgrades to HDT to achieve the maximum test time. The discussion of test time in this section will be limited to the steady test time potentially available in PALM - that is, before it meets the ELM trace. Though the test flow after this point may be useable for experiments, it is not unique to PALM and therefore considered outside the scope of this performance map.

3.7.1 Theoretical

L1D was used to characterise the theoretical performance of HDT operating in PALM at the maximum rated fill pressure of the facility. Fig 3.21 shows transient supply pressure and unit Reynolds number for two cases, one with $x_{wr} = 0.6x_1$ and the other $x_{wr} = 0.3x_1$, to illustrate a range of PALM capability. The value of x_{wr} chosen for the simulations is somewhat arbitrary but is expected to bound physically realisable values and so provide an indication of the achievable performance envelope. It can be seen that $x_{wr} = 0.3x_1$ offers a supply pressure of approximately 75 bar and Unit Reynolds number of 40×10^6 m^{-1} for a test time approaching 1 second. However, higher unit Reynolds numbers can still be achieved, as indicated by the $x_{wr} = 0.6x_1$ case which results in Unit Reynolds numbers of 90×10^6 m^{-1} at a test time of 400 ms.

3.7.2 Practical Limitations

3.7.2.1 Fill Pressure

The first practical limitation considered on is the maximum fill pressure able to be run without risking damage to the facility. The HDT test section and dump tank currently have a pressure rating of 1 bar absolute. Consequently, in order to avoid test section over-pressurisation, the fill pressure of HDT is limited to 100 bar at Mach 7, significantly reducing the unit Reynolds number capability.

3.7.2.2 Facility Unstart

As demonstrated in Section 3.6.1.2, the test time increases offered by ELM and PALM are currently limited by unstart of the facility nozzle. Nozzle unstart is a function of 2 parameters:

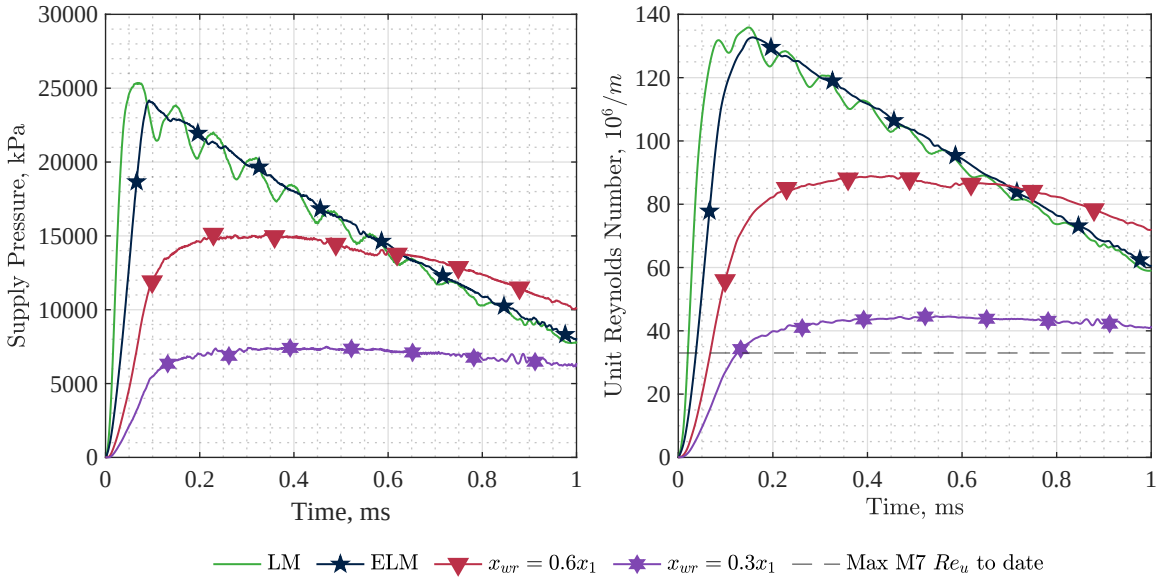

Fig. 3.21 Supply conditions to the facility nozzle with 275 bar, 500 K fill conditions

1) mass flow through the facility, set by nozzle throat diameter and supply conditions, and 2) test section and dump tank pressures. These are dependent on 1, but additionally depend on model blockage, diffuser geometry and dump tank volume. HDT currently features a constant area tube connecting the test section to the dump tank, which limits pressure recovery and consequently does little to prevent the higher dump tank pressure from propagating upstream and collapsing the test flow. Addition of a blockage in the constant area section, as implemented by [117], may aid in pressure recovery and delay nozzle unstart until dump tank pressure exceeds pitot pressure. As is, unstart limits the maximum test time available in PALM to 400 ms.

3.7.3 Current Performance

Based on the practical limitations discussed in the previous section, the currently achievable performance map of HDT operating in PALM can be defined and compared with the theoretical envelope (based on maximum pressure capability of the barrel). The results are presented in Fig. 3.22 where the left figure presents the output of M7 L1D simulations conducted with settings of 100 bar, 500 K, and the figure on the right illustrates the current performance of the HDT operating in PALM. It can be seen that the current test time is limited to approximately 400 ms, with unit Reynolds numbers of approximately 32×10^6 m^{-1} possible. Noting the maximum M7 unit Reynolds number run in the HDT to date is

approximately 33×10^6 m^{-1}, PALM presents a factor of 10 improvement in test time for all Mach 7 unit Reynolds numbers run to date in the facility.

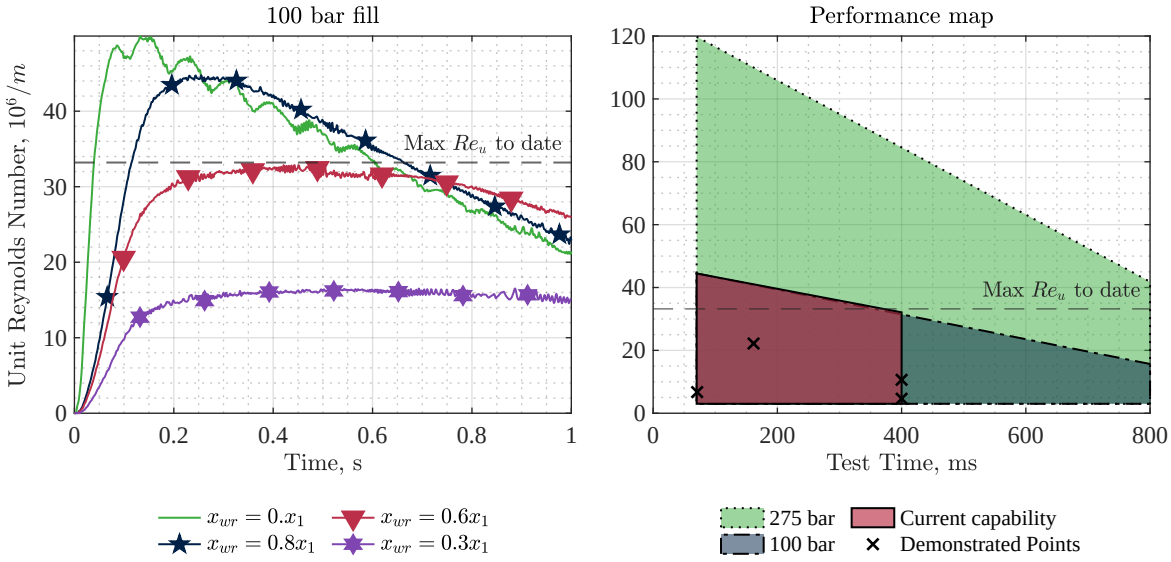

Fig. 3.22 Left: Unit Reynolds number traces with 100 bar fill conditions. Right: Performance map of the HDT operating in PALM at Mach 7.

3.7.4 Potential Facility Upgrades

There are four key recommendations for facility upgrades in order to maximise HDT's test time performance:

1. Pressure test facility test section, dump tank and other downstream infrastructure to a minimum of 5 bar absolute.
2. Redesign ducting between test section and dump tank to prevent unstart.
3. Increase dump tank volume.
4. Replace the circumferential seals on the plug valve with a lower friction alternative.

The first upgrade will increase the unit Reynolds number capability, whilst upgrades 2 and 3 will increase the achievable test time (before unstart). Upgrade 4 will improve the repeatability of the mode, as well as increasing the range of valve openings that can be achieved in PALM and allowing lower values of x_{wr} to be attained. The authors note that whilst the presented analysis was conducted at Mach 7, the recommended upgrades maximise performance across all of the current HDT nozzles.

3.8 Conclusion

This paper has presented experimental results from the commissioning of two new modes in the Oxford High Density Tunnel: Extended Ludwieg Mode and Plenum Augmented Ludwieg Mode. Both modes offer blowdown operation, with ELM producing a steady decrease in supply conditions and PALM producing steady supply conditions at the expense of total pressure capability. Operation in PALM has been experimentally demonstrated for 3 fill conditions. For a 14 bar fill, operation in PALM has been demonstrated to potentially extend test times by a factor of 25, for an approximately 40% reduction in unit Reynolds number capability, though in practice this was limited to a factor of 10 improvement by facility unstart. For a 30 bar fill condition, the improvement in test time was again limited to a factor of 10 from a factor of 15, with a 30% reduction in unit Reynolds capability. For a 55 bar fill condition, a factor of 5 increase in test time was demonstrated for a 20% reduction in unit Reynolds number. In all cases, the PALM supply pressure and unit Reynolds number were steadier than the Ludwieg Mode plateaus. A theoretical performance map for the HDT operating in PALM has been presented, and recommendations made to enhance HDT's current test time performance. It is worth noting that due to the increased duration of facility startup, PALM is currently unsuitable for certain experiments (e.g. free-flight force measurements [52]). Additionally, increased test time may be detrimental for heat transfer experiments, as the 1D semi-infinite wall assumption often used in the data reduction may no longer be valid. However, the improvement in test time greatly expands the capability of the HDT for investigating both steady and unsteady phenomena, for example force balance measurements, fluid-structure interaction, high speed inlet characterisation, and wake flows. Prior to development of PALM, an order of magnitude increase in steady test time for a fully heated Ludwieg tunnel would only have been possible with an order of magnitude increase in facility length. Hence, if any operator of a Ludwieg Tunnel desires to increase facility test time, the authors recommend retrofitting a plenum between the barrel and nozzle and implementing PALM.

Acknowledgements

This research was funded by DSTL. The authors would like to thank Hal Surtell for assembling and installing the PALM pipework. Thanks also to Mailys Buquet, Maxime Dahmani-Moussa, and Tristan Crumpton for operating HDT across the ELM and PALM commissioning campaigns.

Statement of Authorship

Paper Title:

Blowdown operation of Ludwieg Tunnels

Paper Status:

Unpublished and unsubmitted work written in manuscript style

Authors of the original paper:

Hillyer, J., Doherty, L.J., Hambidge, C.J, McGilvray, M.

Author contribution:

- **Hillyer, J.** : Lead author, conceptualisation, data curation, formal analysis, and writing.
- Doherty, L.J. : Supervision as Primary Supervisor.
- Hambidge, C.J.: Supervision as Hypersonics Facilities Manager
- McGilvray, M. : Supervision as Principle Investigator.

Student Confirmation: **Date:** 13/01/2024

Supervisor Confirmation: **Date:** 13/01/2024

Chapter 4

Control effectiveness studies in hypersonic Ludwieg tunnels

Preamble

A research aim of this thesis was to improve the state-of-the-art for control effectiveness studies in Ludwieg Tunnels, in particular by increasing the amount of characterisation that can be performed in a single test. In this chapter, the extended test duration attained in Chapter 3 is leveraged to perform tests in which multiple control effector deflections are characterised in a single test using a deflection-pause methodology. Additionally, this chapter presents the development of the quasi-static technique, a low uncertainty test technique that allows for continuous resolution of control effectiveness with roll position. This chapter is currently unsubmitted but written in manuscript format for submission to journal after the thesis is completed. A statement of authorship is provided at the end of the chapter, and references are given at the end of the thesis.

Associated Appendices:

N/A

Abstract

Control effectiveness studies are typically performed in blowdown facilities, where the available test time allows for multiple model attitudes to be characterised in a single run. However, the costs associated with running blowdown facilities can lead to compromises in the number of configurations characterised, and in the case of the X-43A, can ultimately contribute to flight failure. This paper presents experimental results from testing aimed to improve the state-of-the-art for control effectiveness studies in Ludwieg tunnels to enable these facilities to be used as an alternative to blowdown tunnels during vehicle design. This is achieved by leveraging the extended rise time and test duration of the recently commissioned Extended Ludwieg Mode to 1) investigate the effect of nozzle supply pressure rise time on force balance natural frequency excitation and assess the suitability of a 6 Degree of Freedom Inertial Measurement Unit for acceleration compensation, 2) characterise multiple control effector deflections in a single test and 3) develop a free-to-roll model for continuous, low uncertainty, resolution of control effectiveness as a function of roll position. It is demonstrated that for Ludwieg Tunnels, addition of a plenum between the fast acting valve and the nozzle throat can reduce the magnitude of the startup loads models are subject to, and that the duration of the nozzle startup period, not the overall rise time of the facility nozzle supply trace, dictates which natural frequencies are excited. It is also demonstrated that 6 Degree of Freedom Inertial Measurement Unit's can be used for acceleration compensation, including use of differentiated gyroscope measurements for moment compensation. Excellent agreement is shown between tests performed with a constant wing deflection and those with multiple wing setpoints during the test. The free-to-roll technique is validated against force balance data at zero degrees angle of attack and has demonstrated the ability to characterise multiple roll positions in a single test at angle of attack. Overall, this paper has presented significant improvements to the both the quantity and quality of characterisation that can be achieved in a single run, reducing the total number of tests required to characterise a vehicle's control effectiveness and improving confidence in the aerodynamic database generated during vehicle design.

4.1 Introduction

In any speed regime, the backbone of flight vehicle design is the generation of a high quality aerodynamic database in the form of aerodynamic coefficients. Values for these coefficients can be numerically predicted using Computational Fluid Dynamics (CFD) [1–4], experimentally measured in ground test facilities [6–8], or generated from flight data [9–11], with the trend moving towards numerical techniques as their physical fidelity has grown. However, CFD still requires wind tunnel validation data to improve confidence in its predictions and consequently wind tunnel testing still plays an important role in flight vehicle design.

The need for an extensive, high quality aerodynamic database is demonstrated by the first flight of the X43A, a scramjet demonstrator which failed after suffering an overstressed right elevon during the transonic stage of boost [134]. The post-flight Mishap Investigation Board identified 3 causes for the failure, one of which was aerodynamic modelling inaccuracies resulting from too coarse a resolution of elevon deflection in the pre-flight wind tunnel tests. This caused a non-linearity in both hinge moment and roll control effectiveness - that is, how much roll control moment a control effector can produce - to be missed. Control effectiveness studies such as these generally consist of an experimental model with fixed control effector deflections and resultant forces measured using a force balance. These are typically performed in blowdown facilities [6–8, 15], where the available test time permits multiple attitudes to be characterised in a single run using a pitch-pause methodology. Pauses in model movement enable the flowfield to stabilise and hence permits determination of the static aerodynamic coefficients in the absence of dynamic effects. Choice of resolution is generally dictated by the costs associated with ground testing [6], and hence to improve the resolution of control effectiveness studies either: 1) further improvements to the range of attitudes/configurations characterised in a single run (e.g. models with movable control effectors) or 2) a reduction in the cost-per-run of a control effectiveness study must be made. Noting that blowdown tunnels are generally expensive to operate relative to low enthalpy impulse facilities such as Ludwieg tunnels [16], point 2 can be achieved by improving the testing methodologies currently available in those facilities.

Force measurements in Ludwieg tunnels are complicated by their impulsive nature (specifically, high startup forces, rapid flow initialisation and short test durations) inducing vibrations in the force measurement system that superpose on the measured force signal. It is expected that an increase in rise time of the facility nozzle supply pressure trace will excite fewer of the force measurement system's natural frequencies and consequently reduce the magnitude of these vibrations [25], but where this is not possible custom force balances (designed for maximum natural frequency) [27, 26, 37], and acceleration compensation

[31, 28, 32, 33, 38] can be used to minimise/remove the oscillatory content. To date, acceleration compensation has exclusively used linear accelerometers, with their location in the model being a compromise of geometry and signal quality - accelerometers compensating force measurements are ideally situated as close as possible to the force balance to maximise the likelihood the measured accelerations are in phase with the force measurement, whilst accelerometers compensating moments are ideally placed at model extremities to maximise signal. Use of a 6 Degree-of-Freedom (6DoF) MicroElectricalMechanical Systems (MEMS) Inertial Measurement Unit (IMU), such as those those typically used in free-flight experiments [51, 52, 21, 53–61, 65, 66], may allow for fewer compromises in accelerometer placement, but these are yet to be demonstrated as suitable for acceleration compensation in impulse facilities - particularly for moment compensation where angular accelerations are attained from differentiation of gyroscope measurements.

To date, control effectiveness studies performed in low enthalpy impulse facilities have been either fully static, with only a single attitude and control effector deflection characterised in a run [17–19], or fully dynamic (no pauses) [20, 21]. Static tests allow direct measurement of the static coefficients, but naturally require an extensive number of tests to characterise a vehicle. In contrast, fully dynamic tests have the ability to attain a continuous resolution of control effectiveness with control deflection and attitude, but care must be taken during experimental design in order to ensure that dynamic phenomena are either not influencing the measurements or can be isolated from static coefficients.

This paper leverages the extended test time capability of the recently implemented Extended Ludwieg Mode (ELM) [84, 106] to improve the state-of-the-art for control effectiveness studies in Ludwieg tunnels. Firstly, the effect of the extended rise time and test duration of ELM relative to standard Ludwieg Tunnel operation on the oscillatory content in the measured force traces is explored, and the suitability of a 6 DoF MEMS IMU for acceleration compensation is investigated. Improvements to the state of the art for the control effectiveness studies in Ludwieg tunnels is then achieved by utilising a model capable of moving control effectors during a test and performing experiments with a deflection-pause methodology. The experimental model is a 10 degree half angle cone fitted with all moving wings, and the primary measurements are of roll control effectiveness. Finally, a dynamic test technique - the quasi-static technique - is developed for resolution of control effectiveness with roll angle. This technique leverages the inherently low aerodynamic roll damping characteristic of hypersonic vehicles, coupled with low values of reduced angular velocity, to attain a low uncertainty measurement of the control effectiveness.

The remainder of this paper is organised as follows: descriptions of the experimental facility and model are given in Section 4.2 and Section 4.3, respectively. The data reduction

techniques are explained in Section 4.4, and experimental results are presented in Section 4.5. Finally, conclusions are presented in Section 4.6.

4.2 Facility

4.2.1 The Oxford High Density Tunnel

All tests in this paper were performed in the Oxford High Density Tunnel (HDT), a Ludwieg tunnel located at the Oxford Thermofluids Institute, University of Oxford [121]. A schematic of the facility is given in Fig. 4.1, featuring a barrel of internal diameter 152 mm and length 17.35 m. The barrel is separated from the nozzle plenum by an upstream facing plug valve. The HDT features four operational nozzles, each with an exit diameter of 351 mm, covering the range of Mach 4 to Mach 7. The facility barrel can be heated to 550 K, and has a maximum pressure rating of 275 bar.

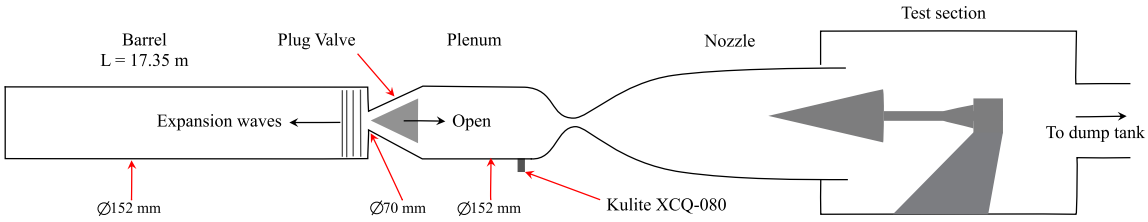

Fig. 4.1 Schematic of HDT. Adapted from [122]

The HDT is currently capable of being operated in 4 modes: 1) Ludwieg Mode (LM), 2) Light Isentropic Compression Heating (LICH), 3) Extended Ludwieg Mode (ELM) and 4) Plenum Augmented Ludwieg Mode (PALM). ELM and PALM are proposed as the most suitable of these modes for force balance experiments owing to their increased test duration, allowing more time for vibrations to damp out, and extended rise time, slightly relaxing the requirement for high natural frequency of the force balance system. Unfortunately PALM was still under active development during these experiments so was not available to be used. The majority of tests presented in this paper were performed in ELM, though LM was also used to investigate the effect of supply pressure rise time on the form of the measured force trace.

4.2.2 Instrumentation

Nozzle supply conditions were measured using sensors mounted in the facility plenum. The supply pressure was measured using a flush mounted Kulite XCQ-080 transducer, and

total temperature calculated from Aspirated Thermocouple (ATC) data using the processing outlined in [122, 123]. The Kulite was amplified with a Fylde FE-H379-TA differential amplifier, and the ATC with an Adafruit AD8495 amplifier. Both supply condition sensors were recorded at 100 kHz on NI PXIE 6368 cards housed in a NI PXIe-1092 chassis (henceforth referred to as the NI DAQ).

4.3 Experimental Model

This section provides an overview of the experimental model used in this testing. The same model was used for both the acceleration compensated force balance and quasi-static experiments, with configuration changes being achieved through replacement of a central assembly.

4.3.1 Geometry

The experimental model used in this campaign, shown installed in the test section in Fig. 4.2a, consisted of a 10 degree half angle cone with base diameter 148.5mm, fitted with 4 all moving wings in an X configuration. To reduce root gap effects, the wings were situated on flats machined into the cone surface. These flats themselves are 3 degree expansions relative to the cone surface, chosen to give sufficient space for the full range of wing motion whilst minimising the static pressure decrease through the expansion. All cone components were manufactured from Aluminium 7075 T6, and a summary of the model properties is given in Table 4.1, where the moment of inertia was measured with a Raptor Scientific KSR 330.

The wings are 3D printed and driven by DFRobot SER0044 servo motors. Sizing of the wings was a balance between the holding torque of the chosen motors, the inertia of the model (to ensure adequate signal) and limiting the possibility of saturation of the onboard IMU in the quasi-static tests. The wing geometry is shown in Fig. 4.2b, and can be seen to have a length of 70 mm and a pivot at 51.5% chord.

A two axis traverse was used in these experiments for positioning the model in pitch and yaw. The traverse has a usable motion range of ± 15 degrees in pitch and ± 5 degrees in yaw. It is not able to be moved during the test.

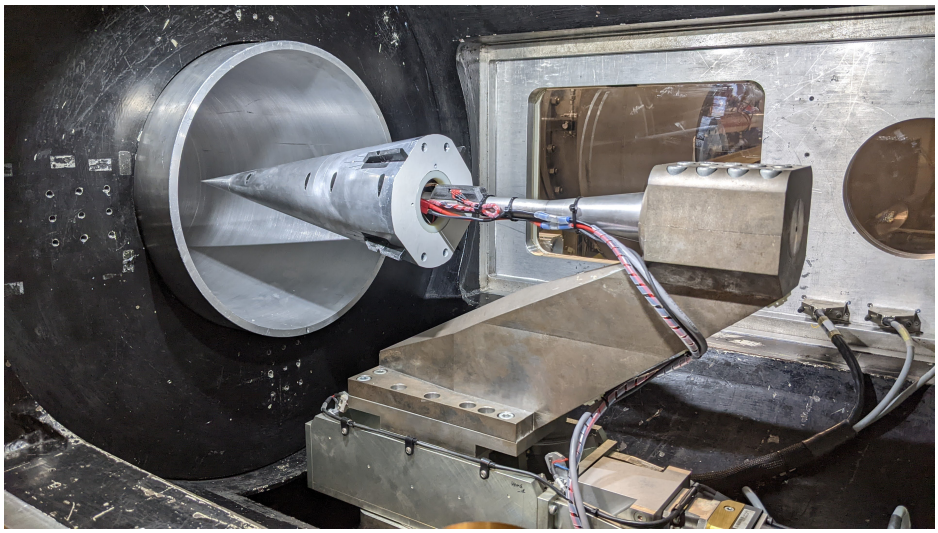

(a) Installed in the test section on the two axis traverse in force balance configuration

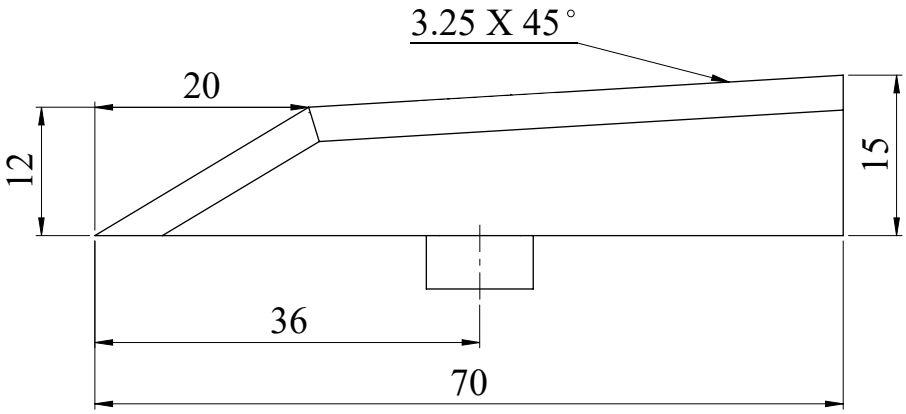

(b) All moving wing geometry. All dimensions in milli metres

Fig. 4.2 Experimental model

4.3.2 Onboard Data Acquisition

The experimental model featured two onboard Data Acquisition Systems (DAQs): a "pressure" DAQ and a "control" DAQ, both installed in each model configuration. Each DAQ recorded a 6-axis TDK ICM-42688-P Inertial Measurement Unit (IMU) at 32 kHz, situated on satellite boards to decouple IMU placement from main DAQ board (aka motherboard) location. A summary of the IMU full scale range and associated uncertainties are given in Table 4.2. The IMU connected to the control DAQ was mounted on the sting and the IMU recorded by the pressure DAQ was mounted in the model on the centreline, just upstream of the bearings/force balance (dependent on model configuration). The pressure DAQ recorded

Table 4.1 Summary of model properties. Inertia is the inertia about the cone axis. Inertia and Centre of Gravity (CoG) measured using a raptor scientific KSR330.

Property	Unit	Value	Uncertainty
Nose radius	mm	1.25	-
Half angle	°	10	-
Base diameter	mm	148.5	± 0.2
S_{ref}	m^2	0.0173	± 0.0001
Mass	kg	3.5	± 0.1
Inertia, J	$kg\,m^2$	0.0068	$\pm 8.5 \times 10^{-5}$
CoG (radius)	mm	0.18	± 0.2

a further 4 Honeywell HSCMAND015PASA5 pressure transducers at 4 kHz, recess mounted on the cone flats (approximately 14 mm upstream of wing tips - see Fig. 4.3a), and used for model alignment, whilst the control board drove the servo motors and recorded their feedback position. The control DAQ also recorded a VectorNav VN100 Attitude Heading Reference System (AHRS) at 400 Hz, providing a Kalman filtered estimate of roll, pitch and yaw and enabling closed loop control of models in the future. The internal layout of the model, with instrumentation locations annotated (excluding IMU on the sting) is shown in Fig. 4.3b.

Table 4.2 TDK ICM-42688-P IMU full scale range and uncertainties. All taken from manufacturers datasheet

	Full Scale Range	Uncertainty
Gyroscopes	$\pm 2000\,^\circ s^{-1}$	$\pm 2\,^\circ s^{-1}$
Accelerometers	$\pm 16g$	$\pm 0.016g$

4.3.3 Quasi-Static Configuration

For the quasi-static experiments, the model was mounted to the sting via a pair of SKF 30202 tapered roller bearings, mounted back to back to provide load bearing capacity in both axial directions. The IMU in the model was used as the primary force measurement device for this configuration, and the sting mounted IMU was not connected. Both DAQs are triggered off of the models roll rate. In the case of tare shots, performed with zero degree wing deflections, the pressure DAQ is triggered from one of the pressure sensors, thereby ensuring data was collected.

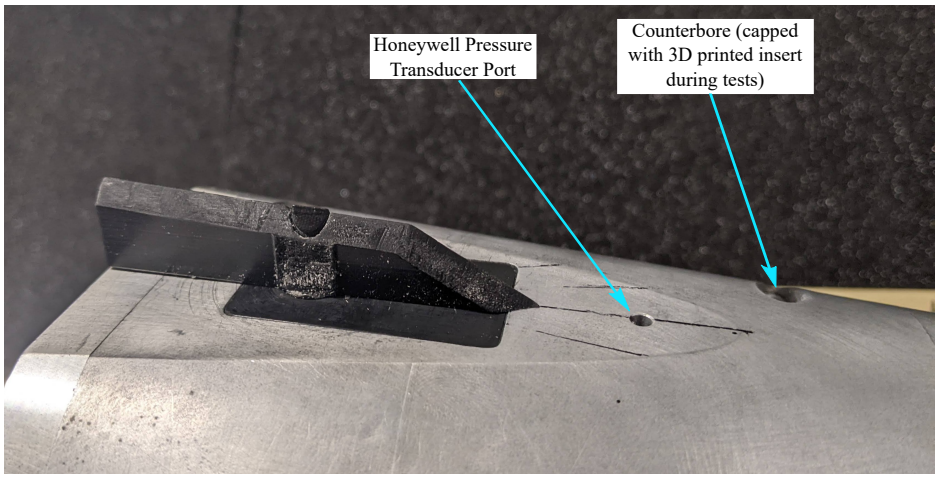

(a) Respective position of the Honeywell pressure transducer ports and the wings on the flats

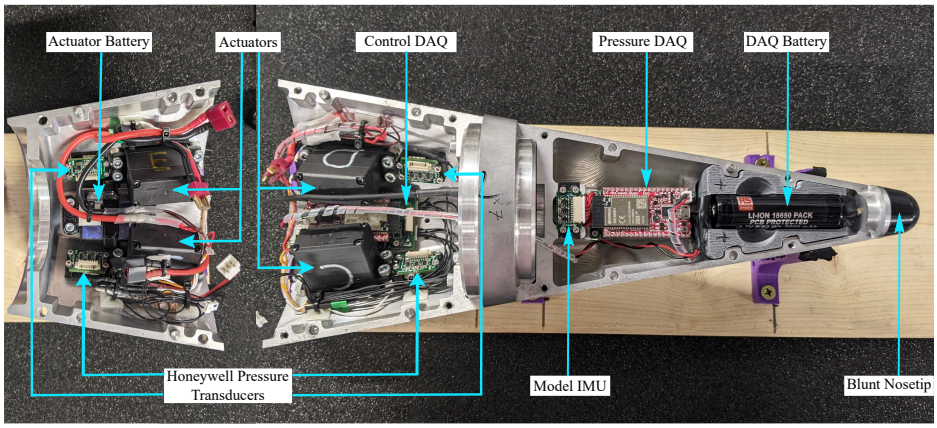

(b) Internal layout of the model. The blunt nosetip was not used in these experiments

Fig. 4.3 Photo of the experimental model, showing the relative positions of the data acquisition systems, the instrumentation and the actuators.

In this configuration, the model is entirely battery powered: the onboard DAQs were both powered by a single 18650 Li-ion battery, whilst the actuators were powered by an Urgenex 2S Li-Po battery. Combined with the onboard data acquisition system, and disconnected IMU on the sting, this setup enabled unrestrained model motion in roll.

4.3.4 Force Balance Configuration

The force balance used in these experiments was an ATI-Mini45, calibration type SI-145-5. A summary of its load ratings and natural frequencies are given in Table 4.3. The force balance has three sensing beams, with applied loads being measured by silicon semiconductor strain

gauges arranged in six half-bridge pairs. Simple bridge completion circuity, mounted in the test section, was used so the force balance could be amplified by a Fylde FE-H379-TA differential amplifier and recorded on the NI DAQ at 100 kHz. The manufacturer provided static calibration was used after verification of its accuracy with an in-house static calibration. This force balance is acceleration compensated using the IMU's recorded by the two onboard DAQs.

Table 4.3 ATI Mini 45 specifications. Note that the natural frequencies listed are for the force balance in isolation. When installed in the model, the additional mass reduces the overall natural frequency of the system [27, 28].

	Full Scale Range	Uncertainty	Natural Frequency
Drag	290 N	$\pm$ 2.175 N	5.4 kHz
Rolling Moment	5 N m	$\pm$ 0.0625 N m	5.6 kHz

As the model was static in this configuration, wires are able to be connected to the model without concern of them being damaged by its motion. For convenience, the onboard DAQs were thus powered by a benchtop power supply, and the servos were driven at 7.2V by a BK precision 1688B power supply. Additionally, both onboard DAQs were triggered with a TTL from the NI DAQ.

4.4 Data Reduction

This section presents an explanation of the data reduction used in this paper, detailing the calculation of freestream properties and aerodynamic coefficients (including coordinate systems). The methodology for uncertainty calculation is also described.

4.4.1 Freestream Conditions

Freestream conditions were calculated assuming isentropic expansion of calorifically perfect air from measured nozzle supply pressure and calculated total temperature data. Total temperature was calculated from plenum based ATC measurements using the processing in [122, 123]. Mach number was assumed to be constant across the test, with the value taken from the measured centreline Mach Number from a Pitot rake shot at the chosen fill conditions. Viscosity was calculated using Keyes relation [130]. A summary of the input uncertainties for the supply condition calculations is given in Table 4.4.

Table 4.4 Summary of the input uncertainties to the supply condition calculations

Flow Property	P0	T0	M	
			LM	ELM
Sensor	Kulite XCQ-80	ATC	Assumed Constant	
Value	Measured	Measured	7.04	7.00
Uncertainty	$\pm$7000 Pa (0.1% FSO)	$\pm$15 K	$\pm$0.06	$\pm$0.071

4.4.2 Coordinate Systems

There are three primary axis systems relating to the aerodynamics of a test article in a wind tunnel test section, all of which have origins at the vehicle centre of mass[1] [25]:

1. *Inertial/Laboratory fixed axes*: x axis is positive downstream, z axis is aligned with the gravity vector and y axis forms the right hand system.

2. *Body Axes*: This is a coordinate system that moves with the test article. The x axis lies in the plane of symmetry of the model, positive towards the nose, y axis points to starboard and the z axis forms a right handed axis system. All moments (yawing, pitching, rolling) are expressed about these axes, and the Eulerian angles (yaw ψ, pitch θ, roll ϕ) are the angles formed between these axes and the inertial axes. Rolling moment is defined as positive by the right hand screw rule about the body axis, and wing deflections are defined as positive when they act to create a positive rolling moment. Noting that all rolling moments presented in this paper are negative, wing deflections are presented as magnitudes rather than absolute values.

3. *Wind axes*: The x axis is defined along the velocity vector of the test article relative to the fluid, the z axis lies in the plane of symmetry of the test article and the y axis forms the right handed axis system. In flight, the definition of the x axis inherently accounts for the motion of the body and the relative wind, but in a sting based experiment where the model is constrained this vector simply reduces to the freestream velocity vector. All body forces (Lift, Drag, Sideforce) are expressed in these axes.

The most significant angles in terms of the vehicle aerodynamics are the angle of attack, α, and angle of sideslip, β, which define the orientation of the body to the effective wind. For a constrained experiment where the model exhibits no translation, these angles reduce to simply the angle between the freestream velocity vector and the body x and y axes,

[1]The origin of the inertial reference frame is arbitrary, and defined at the centre of mass in this work for simplicity.

respectively. For these tests, the body axes were aligned with the freestream velocity vector using the Honeywell pressure sensors, and so movement of the traverse from that aligned position directly affects the model angle of attack and sideslip.

The force balance and IMU's used in these experiments have their own axis systems which rotate with the body axes and so are transformed into the body axes prior to data analysis.

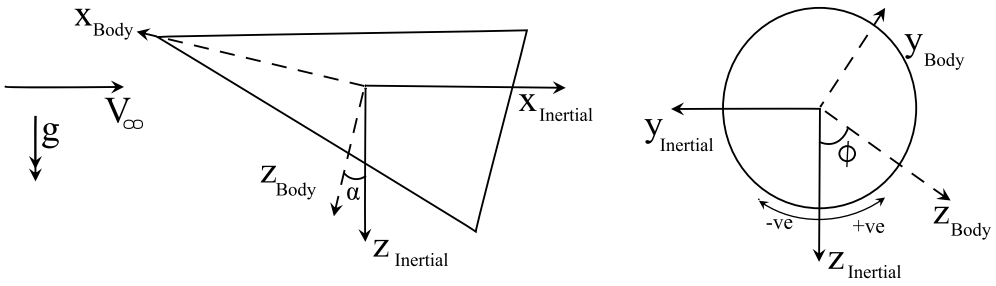

Fig. 4.4 Definition of the body (dashed lines) and inertial (solid lines) axes used in this campaign. In this figure, the freestream velocity vector is assumed to be aligned with the x axis of the inertial frame

4.4.3 Control Effectiveness

The primary measurements in this paper are of roll control effectiveness. In the same way as for the Lift and Drag, the aerodynamic rolling moment, L_{aero}, produced by a flight vehicle can be related to the rolling moment coefficient, C_l, by the dynamic pressure and a reference area as per Eq 4.1:

$$L_{aero} = qS_{ref}l_{ref}C_l \tag{4.1}$$

Where q is the dynamic pressure, S_{ref} is a reference area (for this analysis, cone base area) and l_{ref} is a reference length. The reference length for roll is typically the vehicle span, b, which will be used in all subsequent equations.

In flight dynamics, C_l is typically expressed as a first order Taylor series expansion of perturbations of non-dimensionalised flight states about an equilibrium condition. The coefficients in these equations are typically broken down into groups of static and dynamic coefficients, where static coefficients are functions of the vehicle shape and attitude, and the dynamic coefficients are functions of the time history of its motion. In this analysis, the rolling moment coefficient will be taken to have the form given by Eq 4.2, where the

contributions from static aerodynamics is separated into contributions from the vehicle shape and the control effectors:

$$C_l = \underbrace{C_{l_{Body}}(M,\alpha,\beta,\phi) + C_{l_{Control}}(M,\alpha,\beta,\phi,\delta_1,...\delta_n)}_{\text{Static Coefficients}} + C_{l_{Dynamic}}(M,\dot{\alpha},\dot{\beta},\dot{\phi},\dot{\delta}_1,...\dot{\delta}_n) \quad (4.2)$$

Where $C_{l_{Body}}$ is the rolling moment coefficient produced by the vehicle at that attitude with no control effector deflections, $C_{l_{Control}}$ is the control effectiveness and its dependency on α, β, and ϕ is essentially a measure of how windward the control effector is, and $C_{l_{Dynamic}}$ are the contributions from dynamic aerodynamic derivatives. A measurement of $C_{l_{Body}}$ was attained from a test with no control effector deflection, allowing $C_{l_{Control}}$ to be determined at each attitude for varying control effector deflections.

4.4.3.1 Acceleration Compensated Force Balance

Though the Mini45 is a 6 axis force balance, only the drag and rolling moment measurements are presented in this work. Hence, this section presents an outline of the data reduction used for compensation of those signals, though naturally these processes can be extended to other axes with appropriate axes transformations and filter widths. As the force balance and the IMU were recorded at different sample rates (100 and 32 kHz, respectively), some resampling is necessary. In this work, it was chosen to downsample both traces onto a common timebase to avoid interpolation of data points complicating the uncertainty calculations. The final point to be addressed before moving onto the explanation of the data reduction is the time alignment of the IMU and force balance data (recorded on different DAQs). This was achieved with a least-squares optimisation process, whereby the drag/rolling moment coefficient was assumed constant for a set test window (i.e. Lift/Drag directly follows supply pressure trace) and time alignment shifted to minimise the deviations of the resultant acceleration compensated measurement from a straight line of best fit through the unfiltered/oscillatory data. This process is not dissimilar to the processed used in Störkmann [28], though in that case the least-squares fit was used in determination of the C_{AC} matrix discussed later.

The underlying equations for acceleration compensation of the drag and rolling moment are given in Eq. 4.3 and Eq 4.4, respectively:

$$D_{AC} = D_{UC} - C_{AC} * a_x \quad (4.3) \qquad L_{AC} = L_{UC} - C_{AC} * \ddot{\phi} \quad (4.4)$$

Where D_{AC} and L_{AC} are the acceleration compensated drag and rolling moment, respectively, D_{UC} and L_{UC} are the uncompensated drag and rolling moment, respectively, C_{AC} is a calibration matrix relating the inertial forces to accelerometer readings, a_x is the acceleration in the body x axis and $\ddot{\phi}$ is the angular acceleration about the cone axis.

The process for acceleration compensation of the drag is as follows:

1. Transform IMU axes into body axes
2. Convert from g's to $\mathrm{m\,s^{-2}}$. Assuming 9.81 $\mathrm{m\,s^{-2}}$ for local gravity.
3. Set the initial pre-test accelerations to zero to remove contributions from gravity.
4. Downsample all force and acceleration data onto a common timebase (4 kHz).
5. Perform the acceleration compensation as per Eq 4.3, with C_{AC} equal to the mass of the model

For the rolling moment, the angular acceleration is attained from differentiation of the gyroscope readings as follows:

1. Transform IMU axes into body axes
2. Convert from $^{\circ}\,\mathrm{s^{-1}}$ to $\mathrm{rad\,s^{-1}}$
3. Pre-smooth the angular rates with a 3ms moving average filter.
4. Downsample all force and angular rate data onto a common timebase (4 kHz).
5. Differentiate angular rates to attain angular accelerations.
6. Smooth angular acceleration data with a 2.5ms moving average filter.
7. Perform the acceleration compensation as per Eq 4.4, with C_{AC} equal to the inertia of the model about the cone axis.

The overall rolling moment measured by the force balance is then given by Eq. 4.5:

$$L_{AC} = L_{aero} + L_{CoG} + L_{Reaction} + L_{offset} \tag{4.5}$$

Where L_{CoG} is the rolling moment arising from displacement between the force balance sensing origin and the model centre of gravity, $L_{Reaction}$ are contributions from the reaction moments arising from conservation of angular momentum with all moving wing actuation and L_{offset} is a reported rolling moment arising from zero bias of the strain gauges. If the

force balance is zeroed prior to the test, the output, L_{AC}, then reduces to L_{aero} (evaluated without the contributions from model motion), plus the reaction moments as per Eq 4.6:

$$L_{AC} = qS_{ref}b\left(C_{l_{Body}}(M,\alpha,\beta,\phi) + C_{l_{Control}}(M,\alpha,\beta,\phi,\delta_1,...\delta_n) + C_{l_{Dynamic}}(M,\dot{\delta}_1,...\dot{\delta}_n)\right) + L_{Reaction} \tag{4.6}$$

With the reaction moments and dynamic contributions vanishing for experiments with static wing deflections (assuming steady freestream conditions).

4.4.3.2 Quasi-Static Force measurements

The data reduction equation for the quasi-static technique is yielded by the application of Newtons second law to the force measurement system, given by Eq. 4.7:

$$J\ddot{\phi} = L_{aero} + L_{CoG} + L_{Reaction} - L_{Friction} \tag{4.7}$$

Where $L_{Friction}$ represents the bearing friction and L_{CoG} now arises from displacement between the centre of gravity and the rolling axis (in this case, cone centreline). With reference to Table 4.1, it can be seen that the lateral displacement of the CoG is less than 0.2 mm from the centreline and hence it was decided to neglect this term from the analysis.

As this technique is inherently dynamic, the contribution from dynamic aerodynamics can not immediately be disregarded. Assuming that bearing friction is proportional to angular rate, the rolling moment is now given by Eq. 4.8:

$$J\ddot{\phi} + c\dot{\phi} = L_{Reaction} + qS_{ref}b\left[C_{l_{Body}}(M,\alpha,\beta,\phi) + C_{l_{Control}}(M,\alpha,\beta,\phi,\delta_1,...\delta_n) + C_{l_{Dynamic}}(M,\dot{\phi},\dot{\delta}_1,...\dot{\delta}_n)\right] \tag{4.8}$$

Where c is the coefficient of bearing friction. Again, for static control effector deflections, the rolling moment reduces to Eq. 4.9:

$$J\ddot{\phi} + c\dot{\phi} = qS_{ref}b\left[C_{l_{Body}}(M,\alpha,\beta,\phi) + C_{l_{Control}}(M,\alpha,\beta,\phi,\delta_1,...\delta_n) + C_{l_{Dynamic}}(M,\dot{\phi})\right] \tag{4.9}$$

The only remaining dynamic term in Eq 4.9 is the roll damping coefficient, defined relative to non-dimensional roll rate:

$$C_{l_{dynamic}} = C_{l_{\dot{\phi}}} \frac{\dot{\phi} b}{2V} \qquad (4.10) \qquad C_{l_{\dot{\phi}}} = \frac{\partial L}{\partial \frac{\dot{\phi} b}{2V}} \qquad (4.11)$$

And hence, the data reduction for the quasi-static tests is given by Eq 4.12:

$$J\ddot{\phi} + \left(c - C_{l_{\dot{\phi}}} \frac{qS_{ref} b^2}{2V} \right) \dot{\phi} = qS_{ref} b \left(C_{l_{Body}}(M, \alpha, \beta, \phi) + C_{l_{Control}}(M, \alpha, \beta, \phi, \delta_1, ...\delta_n) \right) \qquad (4.12)$$

It is well understood that the roll damping experienced by a hypersonic vehicle is extremely low [49, 135, 48, 136]. Quinn [49] develops a theoretical prediction of roll damping derivative for a cone travelling at hypersonic speeds, given by Eqs. 4.13-4.15:

$$C_{l_{\dot{\phi}}} = \frac{0.688}{(\sin(\theta_c))^{1/2} * (Re_{d,\infty})^{1/2}} \left[\lambda \frac{\mu_1}{\mu_\infty} \frac{P_1}{P_\infty} \frac{M_1}{M_\infty} \left(\frac{T_\infty}{T_1} \right)^{1/2} \right]^{1/2} \qquad (4.13)$$

$$\lambda = \frac{T_1}{\mu_1} \frac{\mu'}{T'} \qquad (4.14) \qquad \frac{T'}{T_1} = 1 + 0.076(\gamma - 1) M_1^2 + 0.481 \left[\frac{T_W}{T_1} - 1 \right] \qquad (4.15)$$

Where P is pressure, μ is viscosity, M is Mach number and T is temperature, with subscripts 1 denoting inviscid surface values, ∞ denoting freestream values, W denoting wall conditions and $'$ denoting average boundary layer values.

Substituting values for this experiment (using Keyes' relation for viscosity) into Eqs. 4.13-4.15 yields:

$$C_{l_{\dot{\phi}}} \approx 0.0049 \qquad (4.16) \qquad C_{l_{\dot{\phi}}} \frac{qS_{ref} b^2}{2V} \approx 4.9 \times 10^{-6} \qquad (4.17)$$

The bearing friction was determined in-situ at the end of each test while the model was still rotating in a near vacuum environment using Eq. 4.18:

$$\frac{c}{J} = -\left(\frac{\ddot{\phi}}{\dot{\phi}} \right)_{\text{Wind off}} \qquad (4.18)$$

Typical values for bearing friction, c, were found to be 0.001-0.003. Whilst the above theoretical prediction does not include contributions to the damping from the all moving wings, these are not expected to make order of magnitude differences to the overall damping. Consequently, it is expected that the bearing friction will dominate the aerodynamic roll damping and thus the rolling moment is given by Eq. 4.19:

$$J\ddot{\phi} + c\dot{\phi} = qS_{ref}b\left(C_{l_{Body}}(M,\alpha,\beta,\phi) + C_{l_{Control}}(M,\alpha,\beta,\phi,\delta_1,...\delta_n)\right) \tag{4.19}$$

4.4.4 Uncertainties

All uncertainties have been propagated through the data reduction techniques outlined previously using the jitter methodology [129] (5 point stencil and a 0.2% perturbation magnitude), with the exception of the acceleration compensation and bearing friction. Acceleration compensation serves only to remove oscillations about the mean value, rather than affecting the mean value itself, and consequently the presented uncertainties are those provided by the force balance manufacturer (cf. Table 4.3). For the bearing friction, the calculated uncertainty for $\frac{c}{J}$ was felt unreasonably low[2] in light of the assumptions used in Eq. 4.18 and consequently a $\pm 10\%$ relative uncertainty was used for the value of $\frac{c}{J}$. In all plots in the experimental results section, uncertainties are shown with shaded regions, plotted only over each shots' test time.

4.5 Experimental Results

4.5.1 Facility Nozzle Supply Conditions

All tests in this paper were performed at Mach 7 with fill conditions of 8 bar and 500 K, corresponding to an 38km altitude flight condition at one to five scale. Typical supply condition traces of the HDT operating in LM and ELM are shown in Fig. 4.5, with LM producing several steady flow plateaus of 35 ms duration and ELM demonstrating an increased rise time followed by a steady decrease in supply pressure for approximately 400 ms. A detailed explanation of the form of each trace is given in Chapter 3.

4.5.1.1 Model Alignment

Two independent methods were used to confirm alignment of the model with the freestream, both leveraging it's broadly axisymmetric nature: 1) Orthogonal Pressure Sensors (identical when aligned) and 2) Lift and sideforce (0 when aligned). Results are shown in Fig. 4.6. It can be seen there is excellent agreement between the pressure sensors across the test, with the exception of the North East sensor for $0.15 < t < 0.25$ s. This is likely a result of this

[2]The calculated uncertainties were on the order of 10^{-7}.

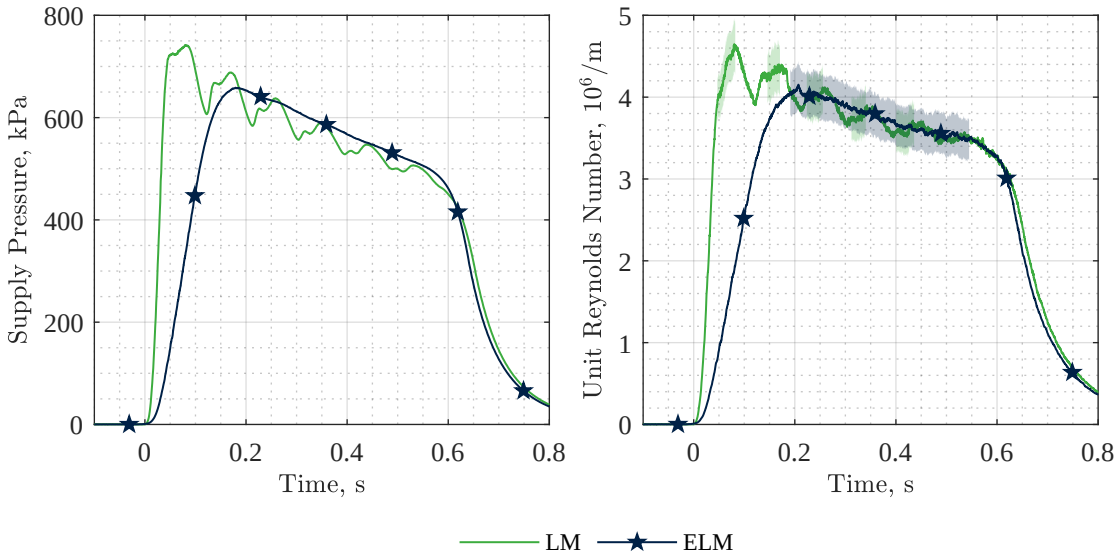

Fig. 4.5 HDT Nozzle supply conditions used in these experiments. Uncertainties are present on the supply pressure plot, but are too small to see

sensor having a slightly more recessed mounting due to a manufacturing defect. The lift and sideforce show good agreement, both demonstrating oscillations about 0 N.

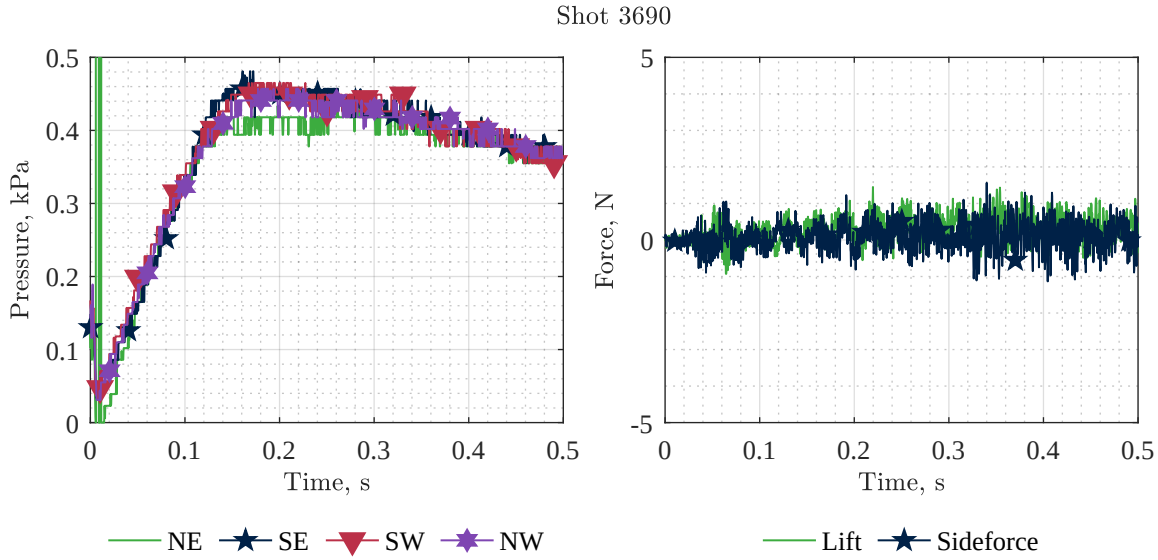

Fig. 4.6 Typical pressures and acceleration compensated forces from an “aligned” shot

4.5.2 Force Balance Results

This section presents experimental results utilising a commercial off-the-shelf force balance in a hypersonic Ludwieg Tunnel. It beings with a discussion of the effect of the form of the nozzle supply trace, particularly rise time and test duration, before presenting results from acceleration compensation and test performed in a deflection-pause manner.

4.5.2.1 Effect of Rise time/Nozzle startup and test duration

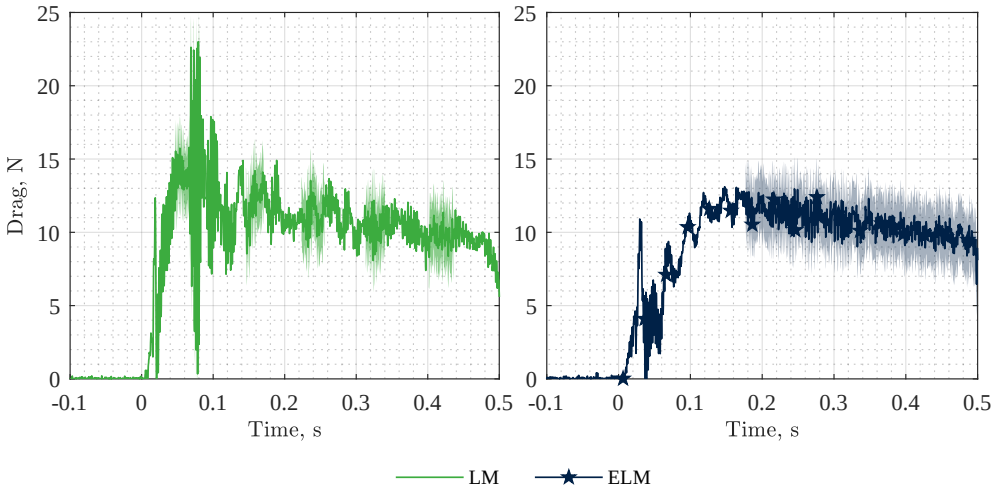

(a) Drag

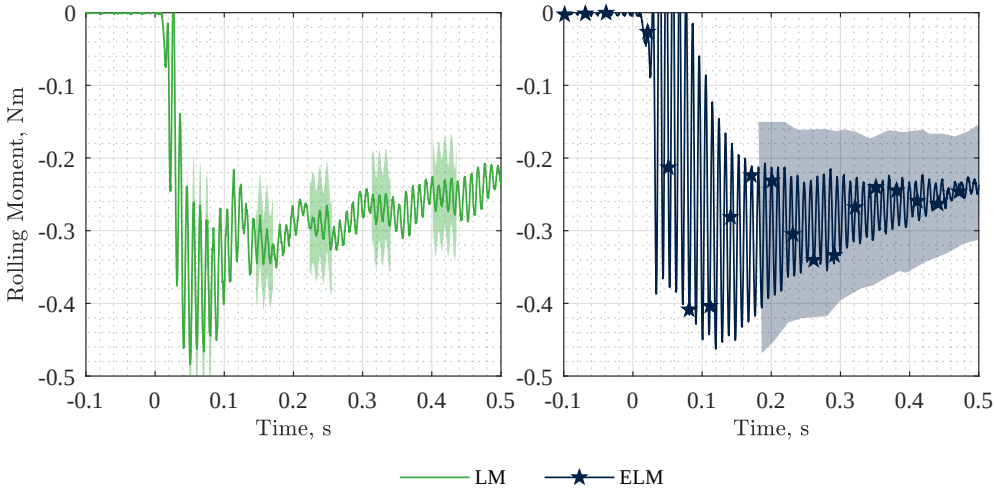

(b) Rolling Moment

Fig. 4.7 Uncompensated, unfiltered force measurements in LM (shot 3658, left) and ELM (shot 3653, right).

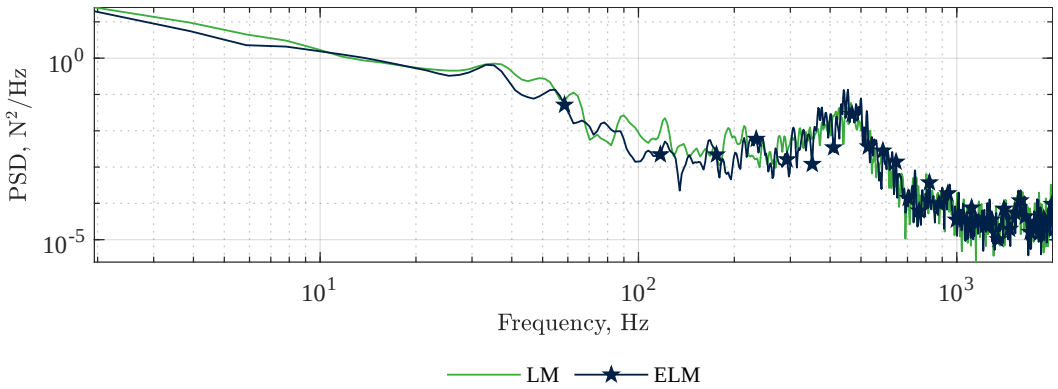

(a) Drag

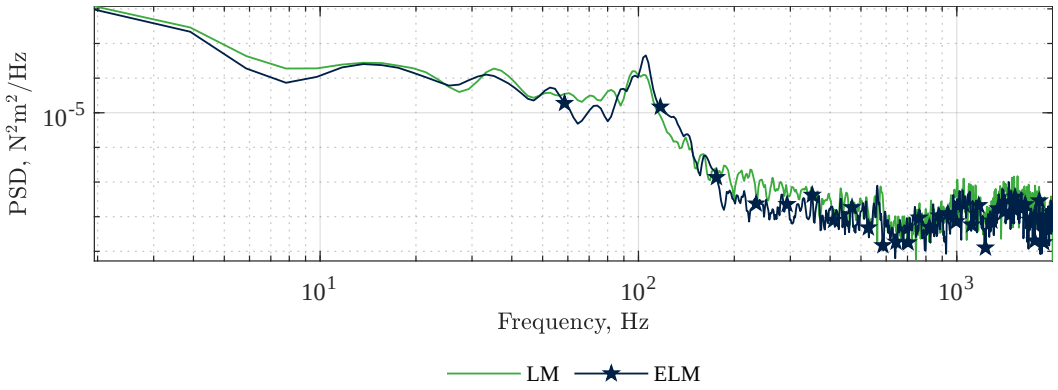

(b) Rolling Moment

Fig. 4.8 Power Spectral Density of each force measurement

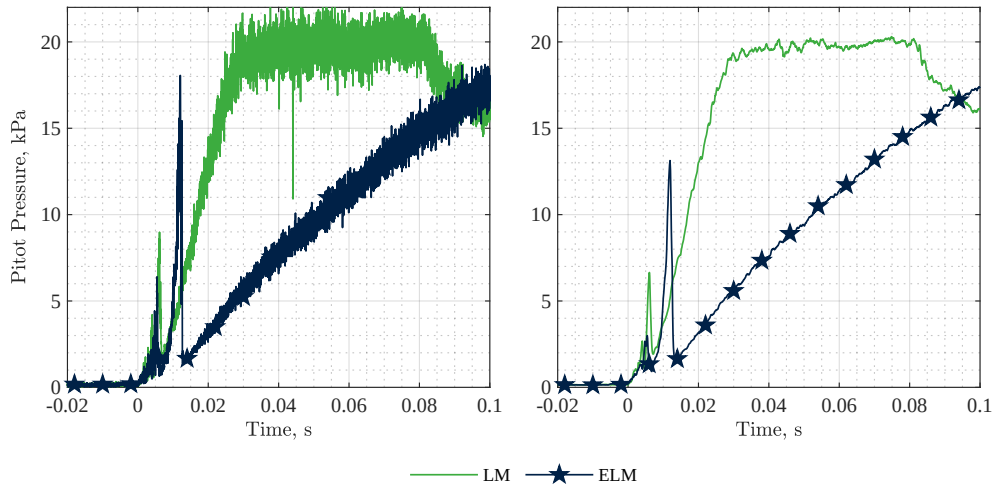

Fig. 4.9 Unfiltered (left) and 1kHz low pass filtered (right) Pitot Pressure traces in LM (shot 3614) and ELM (shot 3623). For both traces, $t = 0$ is set to flow arrival

Fig. 4.7a and Fig 4.7b present the unfiltered drag and rolling moment, respectively, attained from shots operated in LM and ELM to investigate the effect of rise time and test duration on resultant force measurements. Though drag is not of critical importance for control effectiveness studies, it is included in this discussion for completeness. It can be seen that all traces broadly follow their respective supply pressure traces (cf. Fig. 4.5), but feature transient spikes and oscillations as a consequence of excitation of the system natural frequencies. From inspection of the Power Spectral Density (PSD) shown in Fig. 4.8, it can be seen that there are two natural frequencies of importance for the Drag measurements: 1) the natural frequency of the sting ($\approx$ 35 Hz) and 2) the natural frequency of the force balance and the model itself ($\approx$ 500 Hz). For the rolling moment, the response is only dominated by the natural frequency of the model and force balance ($\approx$ 100 Hz). It can be seen that the quality of the drag measurements is comparable in each mode, though the LM trace demonstrates excitation of the 500 Hz mode on each plateau. However, for the rolling moment, it can be seen that operation in ELM results in a significant increase in oscillation magnitude despite the increased rise time - contrary to expectations given existing literature [25, 26].

The Pitot pressure traces shown in Fig. 4.9, taken from a 14 bar shot in each mode, reveal the cause of the increased oscillation magnitude in ELM. Two shocks arising from the nozzle starting process can be seen for both modes, with ELM producing shocks that are both stronger and further apart in time. Defining the nozzle startup time as from when the pressure starts to rise to the passage of the second shock, it can be seen that this is approximately 5 ms for the LM case, whilst for ELM it is approximately 12 ms. The characteristic times of the system are summarised in Table 4.5, demonstrating the increased oscillation magnitude of the rolling moment in ELM is a consequence of the increased duration of the nozzle startup period. Hence, it is the duration of the nozzle startup period, as opposed to the rise time of the supply pressure, that is of critical importance for excitation of the natural frequencies of the system. However, as expected, the extended test duration available in ELM allows for the induced vibrations to damp out, ultimately culminating in lower oscillation magnitudes at the end of the test.

Table 4.5 Summary of characteristic times of the force balance and supply pressures, Nozzle startup is defined as the time between the pitot pressure starting to rise and the passing of the secondary nozzle shock.

	Drag		Rolling Moment	Rise Time		Nozzle Startup	
	Sting	FB	FB	LM	ELM	LM	ELM
Characteristic Time, ms	28	2	10	25	110	5	12

It should be noted that whilst both Fig. 4.7a and Fig 4.7b show a transient increase in drag and rolling moment at the start of the test in both modes (occurring at $t = 20$ms for LM and at $t = 30$ms for ELM), the magnitude of this increase is less than the peak value measured during the test - atypical of force measurements in impulse facilities. This is a consequence of the HDT featuring a plenum between the barrel and nozzle throat, allowing the nozzle starting process to occur at a lower supply pressure and reducing the strength of the starting shocks. This observation allows future experimenters to size their force balance load rating based on the forces expected during the test as opposed to the startup forces, reducing uncertainty in the measurements.

4.5.2.2 Acceleration Compensation

Fig. 4.10b and Fig. 4.10c present model and sting based acceleration compensation, respectively, of the drag in both modes. It can be seen that neither compensation technique is able to significantly improve the quality of the drag measurements in LM, though model based compensation does reduce the magnitude of the transient variation for $0.07 \leq t \leq 0.1$ s. The relative advantages of each acceleration compensation technique are well demonstrated by the ELM data in Fig. 4.10b and Fig. 4.10c, where it can be seen that model based compensation is able to remove the majority of the contributions from force balance natural frequencies, whereas the sting based acceleration compensation is able to remove the lower frequency oscillations attributed to the sting vibrations. This is corroborated by the PSD data shown in Fig. 4.11, demonstrating a reduction in the power of the respective natural frequencies for each compensation type. Interestingly, the model IMU does display a peak in the PSD at the sting natural frequency, which suggests this frequency content was out of phase between the model IMU and the force balance.

Noting that this paper presents the first time[3] that acceleration compensation of a moment measurement has been performed using differentiated gyroscope data from a 6 DoF MEMS IMU, it is felt necessary to present the IMU data at the critical stages of data processing before presenting the acceleration compensated data itself. This is shown in Fig. 4.12, with gyroscope data being given in Fig. 4.12a and differentiated gyroscope data in Fig. 4.12b. As expected, the raw gyroscope data demonstrates clear oscillations about zero $\mathrm{rad\,s^{-1}}$, at a frequency of approximately 500 Hz (force balance natural frequency). The moving average filter removes the transient oscillations superposed on this signal, though this comes at the cost of a slight reduction in the peak values of the trace. These trends are then repeated in the differentiated gyroscope data, though the magnitude of the transient oscillations superposed on the 500 Hz content is significantly reduced.

[3]To the authors knowledge

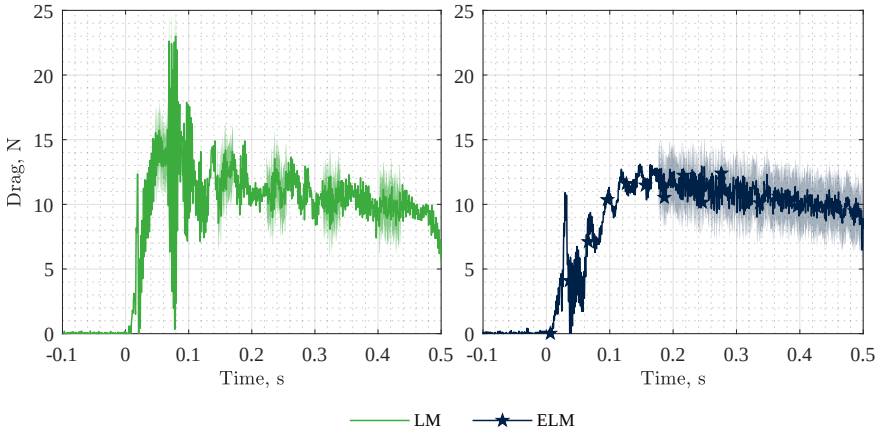

(a) Uncompensated, unfiltered Drag measurements (reproduced for clarity)

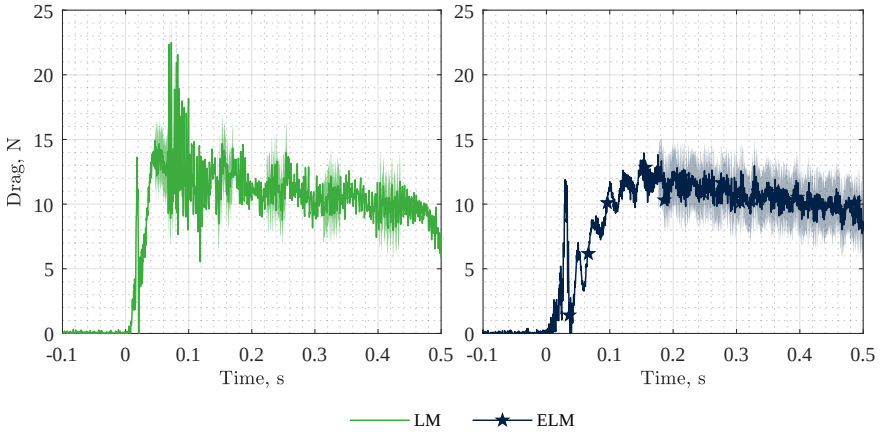

(b) Model based acceleration compensation

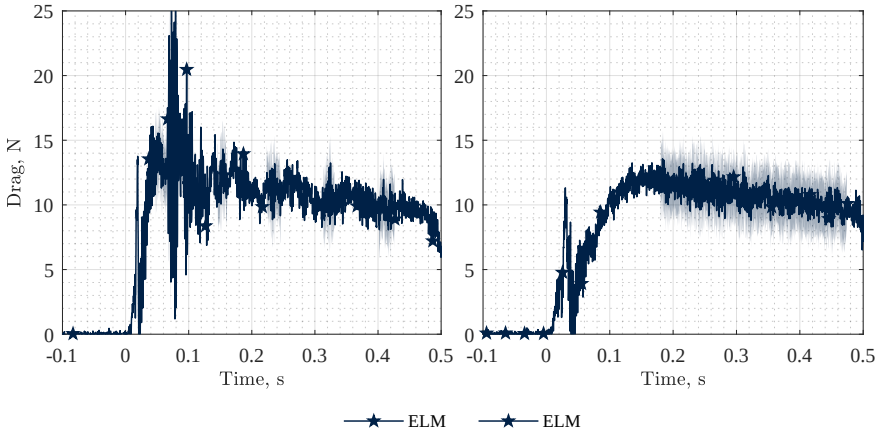

(c) Sting based acceleration compensation

Fig. 4.10 Acceleration compensated Drag measurements in LM (shot 3658, left) and ELM (shot 3653, right).

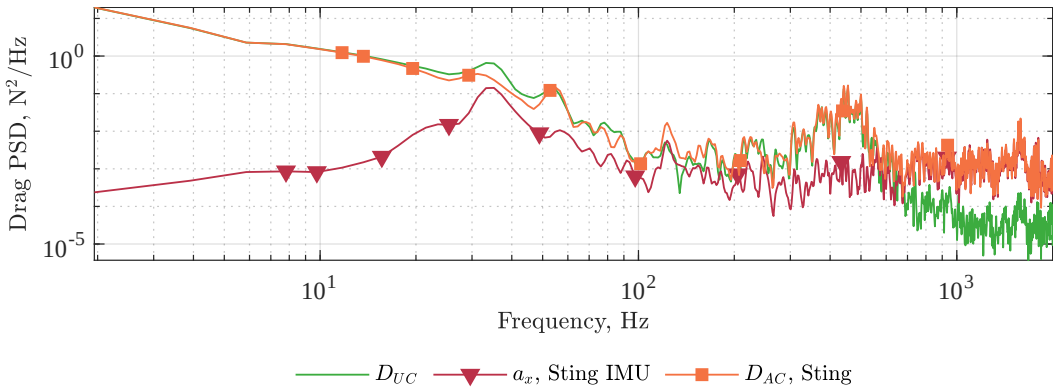

(a) Sting based acceleration compensation

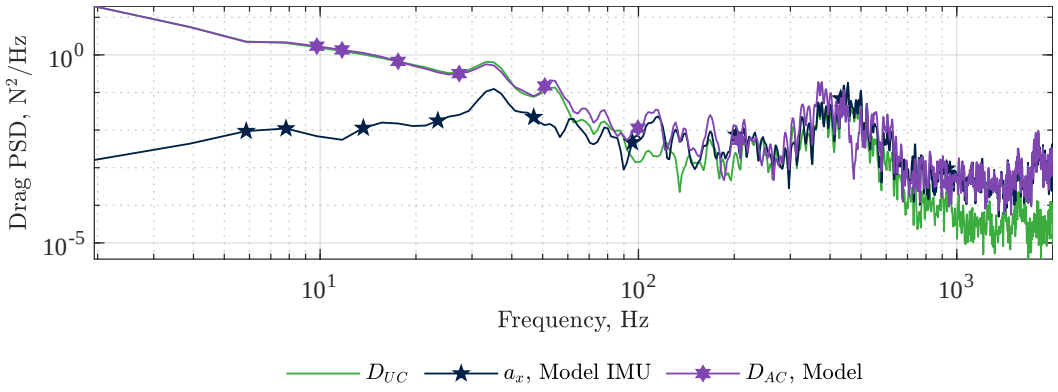

(b) Model based acceleration compensation

Fig. 4.11 Power spectral densities of drag measurements with each type of acceleration compensation in ELM (shot 3653)

Fig. 4.13b presents acceleration compensation of the rolling moment in LM and ELM, demonstrating an almost complete reduction of the low frequency oscillations and significantly improving the quality of the data. This is again in agreement with the PSD data shown in Fig. 4.14, which demonstrates a reduction in the power of the 500 Hz frequency content present in the uncompensated data. Together, Fig. 4.12, Fig. 4.13b and Fig. 4.13b demonstrate 6 axis MEMS IMU's are suitable for acceleration compensation in hypersonic Ludwieg tunnels, including the use of differentiated gyroscope measurements for moment compensation.

Overall, this section has demonstrated that the use of acceleration compensation in Ludwieg tunnels can significantly improve the quality of force and moment data attained (even without a custom force balance) and hence acceleration compensation is recommended for any force balance testing in facilities with similar test durations where commercial-off-the-shelf force balances are used.

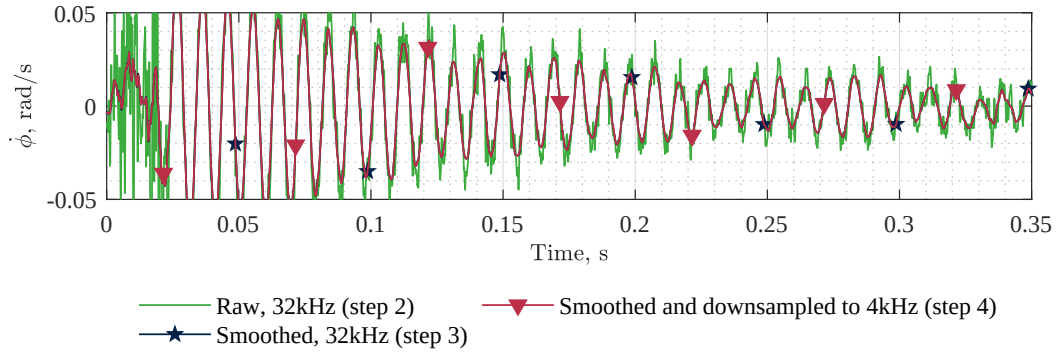

(a) Raw roll rate and 3 ms moving average filtered roll rate

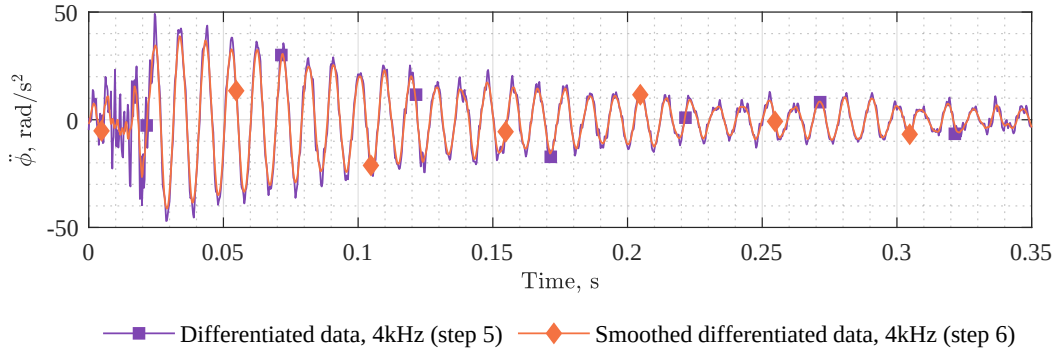

(b) Angular acceleration, with and without a 2.5 ms moving average filter applied after differentiation

Fig. 4.12 Data from the model IMU used in rolling moment compensation in ELM (shot 3653). Zoomed in relative to the plots to demonstrate the effect of filtering on the signal during processing

4.5.2.3 Deflection-Pause Tests

Fig. 4.15 presents comparisons between tests with fully static wing deflections and a test performed with a deflection-pause methodology. In all cases, testing was performed in ELM and all 4 moving wings were deflected. Uncertainties are plotted only over each shots test time - the differences in test period start is a result of the changeable rise time in ELM as a consequence of wear on the plug valve piston seals (see Section 3.6.2.3) - and hence data can only be compared in these regions. Looking first at the uncompensated data in Fig. 4.15b, it can be seen that the data from the deflection-pause test is significantly less oscillatory than the tests with static deflections. Noting the reduction in oscillation magnitude in the 10° static deflection case relative to the 20° wing deflection, the lower oscillation magnitude in the deflection-pause test arises from the wings being in a neutral position (i.e. zero degree deflection) at the passage of the starting shocks over the model - essentially reducing the

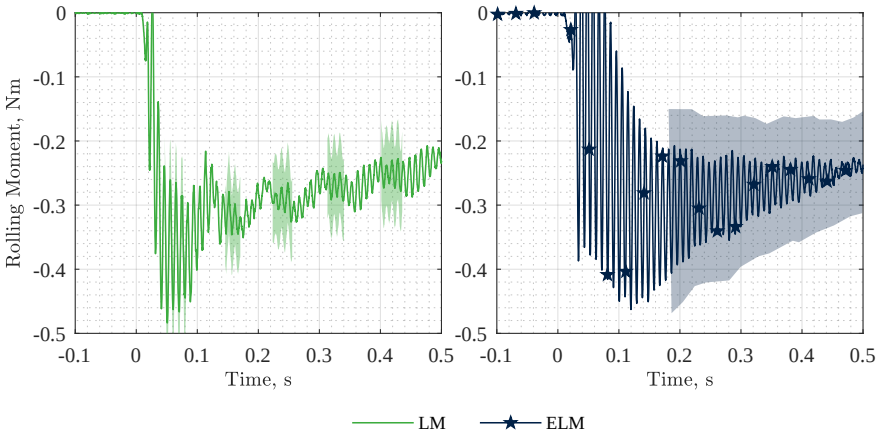

(a) Uncompensated, unfiltered Rolling Moment (reproduced for clarity)

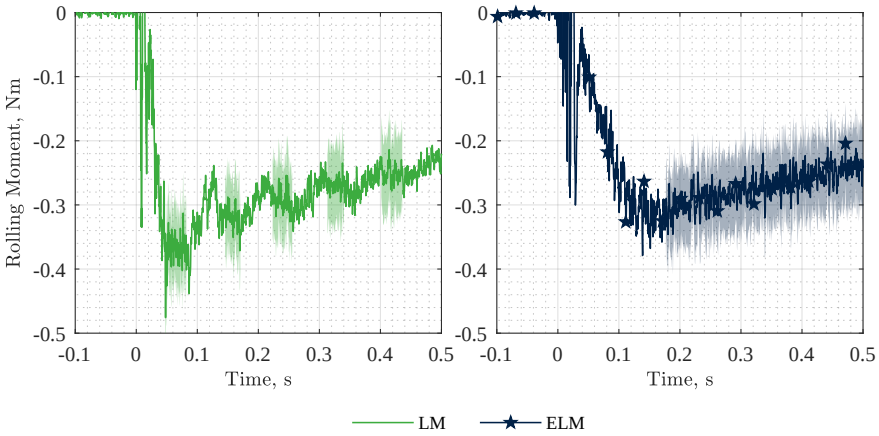

(b) Model based acceleration compensation

Fig. 4.13 Rolling moment measurements in LM (shot 3658, left) and ELM (shot 3653, right). All data downsampled to 4 kHz as per processing outlined in Section 4.4.3.1.

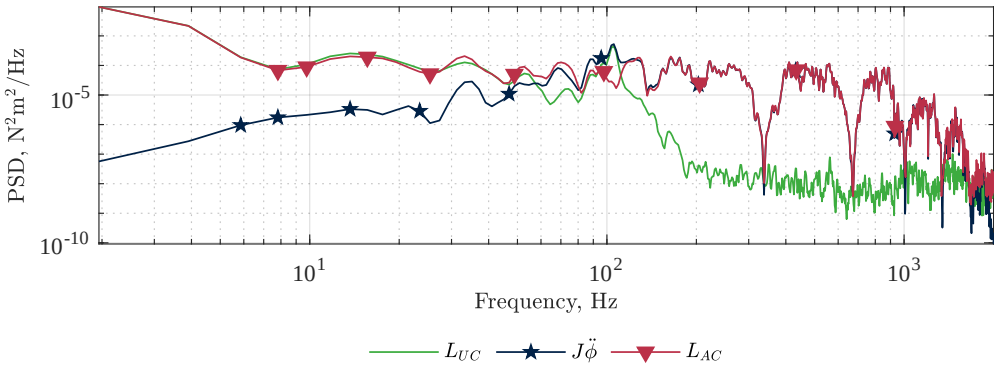

Fig. 4.14 Power spectral densities of rolling moment measurements with and without acceleration compensation in ELM

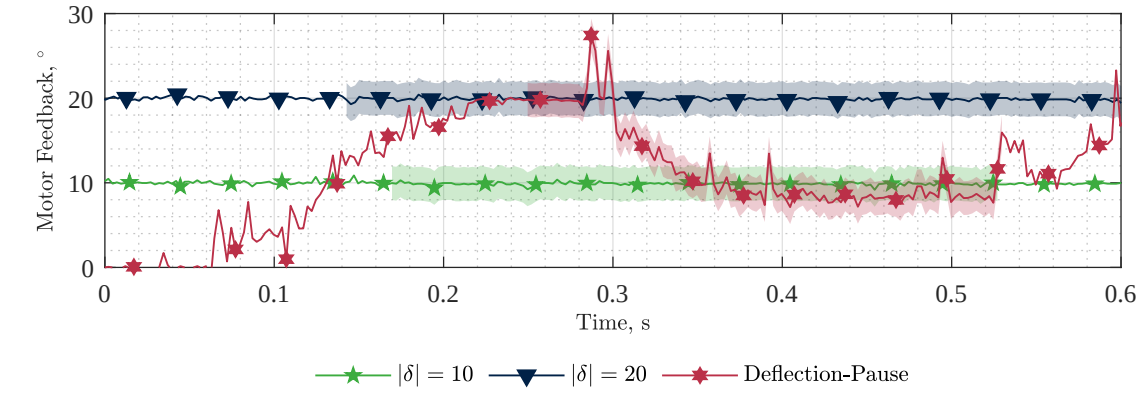

(a) Motor feedback

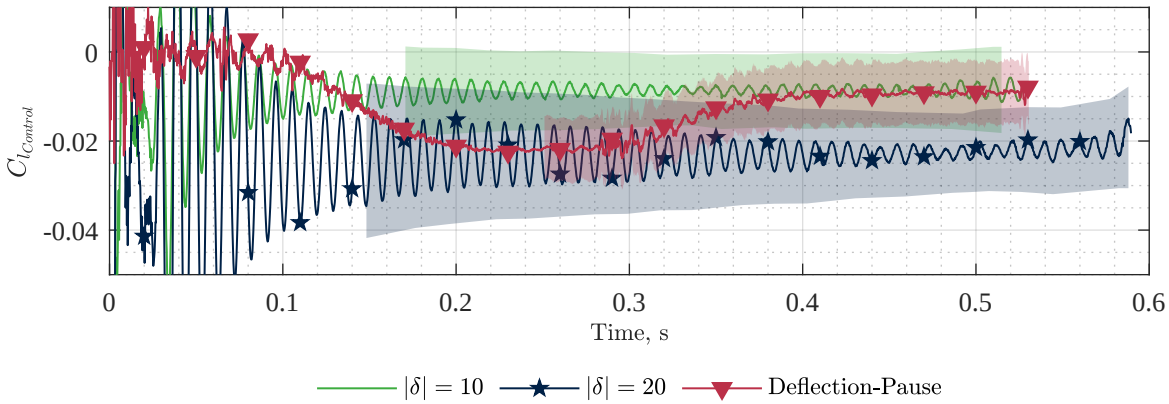

(b) Uncompensated data

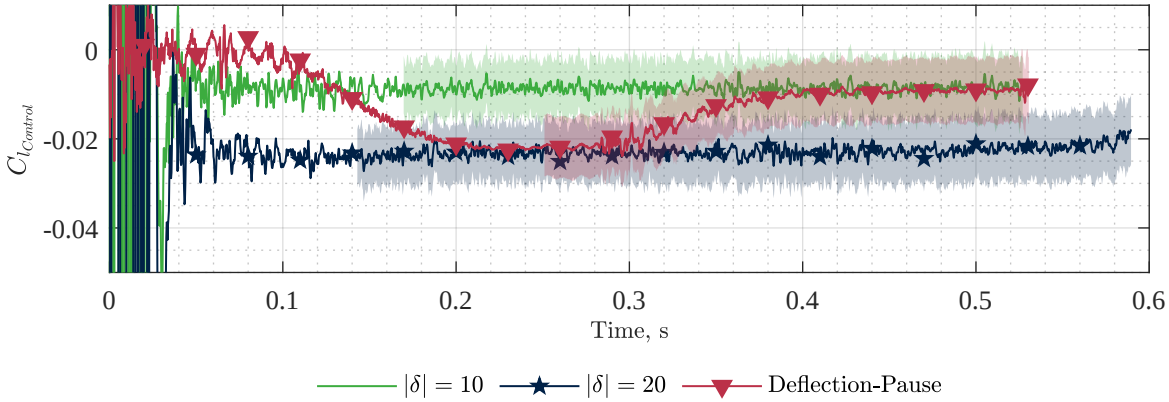

(c) Acceleration compensated data for static wing deflection tests, uncompensated data for the deflection-pause test

Fig. 4.15 Comparison of tests with fully static wing deflections and a test performed with a deflection-pause methodology. Uncertainties are only plotted over each shots test time.

magnitude of the forcing function for oscillation generation. This results in a lower signal from the gyroscopes and consequently precludes the use of acceleration compensation in

that shot. For this reason, the acceleration compensated data from the static tests is plotted against the uncompensated data from the deflection-pause test in Fig. 4.15c. It can be seen that there is excellent agreement between the static wing deflection and deflection-pause tests, with only a minor (<5%) under-prediction for the 20° setpoint and another minor (<5%) over-prediction for the 10° setpoint. Though the differences here are minor, and well within the uncertainty of the force balance, the form of this trace, as well as the motor feedback shown in Fig. 4.15a, indicates that the difference arises from issues with the motors ability to accurately track the command. This could be a result of either the internal PID loop of the servos not being precise enough or the power supply used lacking sufficient power to drive all the actuators simultaneously. Regardless, the agreement between static data and deflection-pause tests is close enough to demonstrate the feasibility and utility of performing deflection-pause tests for control effectiveness measurements in Ludwieg tunnels.

4.5.3 Quasi-Static Results

This section presents the experimental data attained with the quasi-static technique. It begins with a validation of the technique against force balance data, presents results from tests aiming to resolve control authority as a function of roll position at angle of attack, before presenting results from experiments using a deflection-pause methodology.

4.5.3.1 Validation of methodology

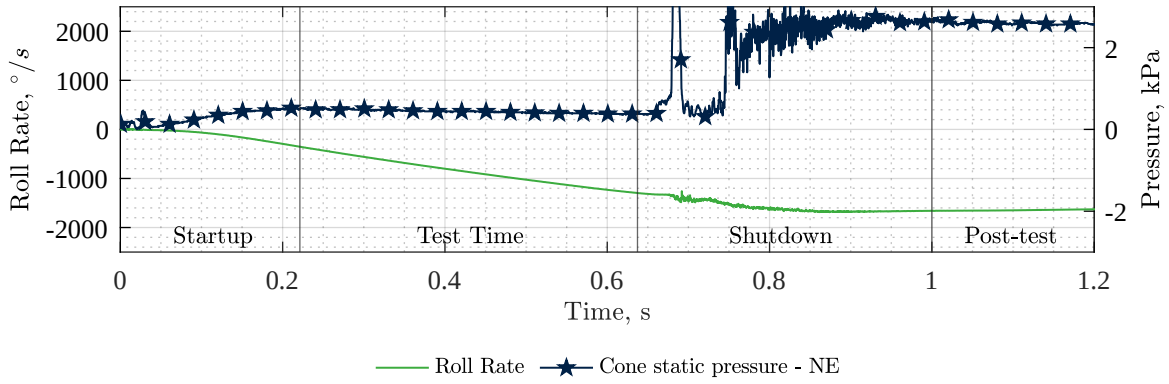

Fig. 4.16 Example roll rate trace from quasi-static tests, with pertinent test periods labelled. Shot 3695

Fig. 4.16 presents typical roll rate and cone static pressure traces from a quasi-static test, with pertinent test periods labelled. It can be seen that there is an approximately linear roll rate during the test time, indicating an approximately constant control effectiveness, as

expected. The bearing friction is estimated during the post-test period after tunnel shutdown, with test section pressures of approximately 2.5 kPa.

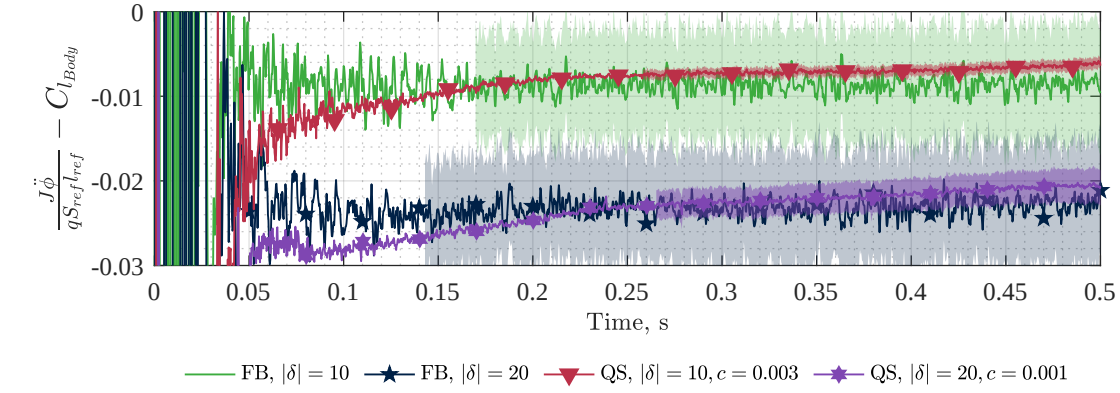

(a) Contributions from bearing friction neglected

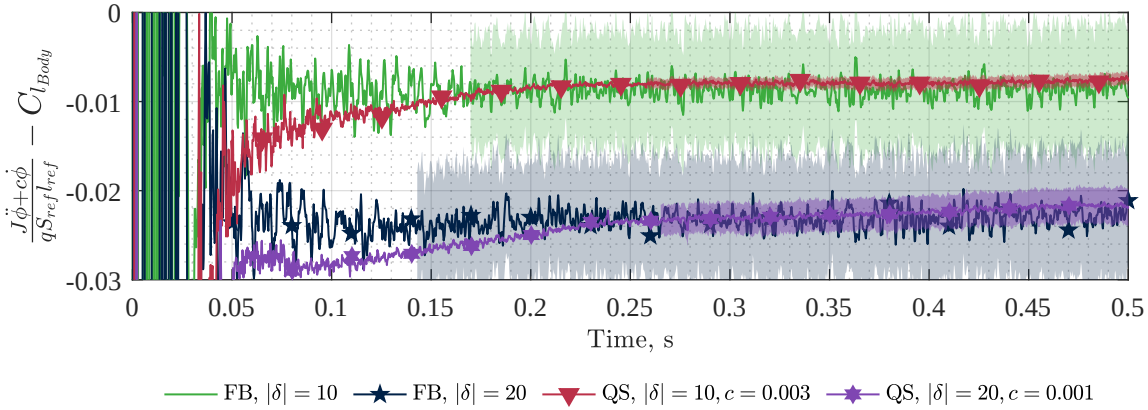

(b) Accounting for bearing friction, using the post-test deceleration to estimate bearing friction

Fig. 4.17 Comparison between Force Balance (FB) and Quasi-Static (QS) Data

Validation that the quasi-static technique is providing a measurement of the static aerodynamics in absence of dynamic effects is demonstrated by the results presented in Fig. 4.17, which presents a comparison with force balance tests. Again, all tests were performed in ELM and all four wings were deflected. Fig. 4.17a presents results neglecting the contribution of bearing friction. It can be seen there is moderate agreement between the two techniques, with the quasi-static data for both wing deflections showing a consistent under-prediction of the rolling moment relative to the force balance case. The degree of under-prediction increases with time and hence roll rate, indicating that the contribution from damping and friction can not be ignored. Fig. 4.17b shows the quasi-static data calculated with the bearing friction found from post-test decelerations. Accounting for bearing friction significantly improves the agreement between the two techniques, demonstrating that the aerodynamic roll damping is negligible relative to the bearing friction and unable to be ascertained with the current setup,

as expected. It can be seen that for both wing deflections, the quasi-static data presents a lower uncertainty measurement of the control effectiveness relative to the force balance case. Overall, the capability of the quasi-static technique, including using the post-test period to estimate bearing friction, has been demonstrated for performing control effectiveness studies.

4.5.3.2 Resolving control effectiveness as a function of roll angle

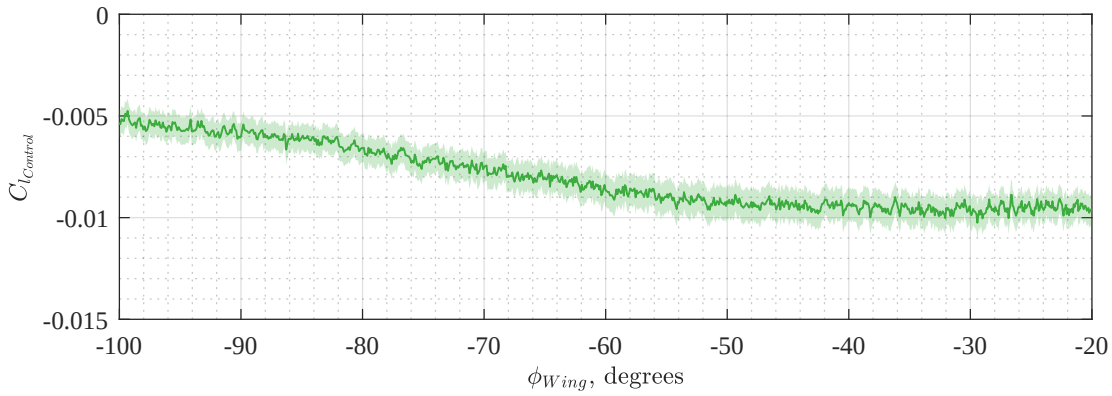

(a) Cone at 6° angle of attack and a single wing deflection of 20°

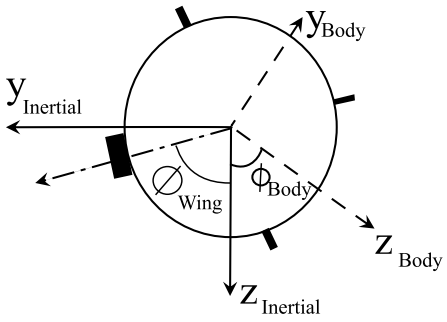

(b) Definition of ϕ_{Wing}

Fig. 4.18 Use of the quasi-static technique to characterise control effectiveness as a function of roll angle

Noting that the control authority provided by a control effector is directly influenced by how windward that control effector is, Fig. 4.18 presents data from a shot performed with the cone at 6° angle of attack and a single wing deflected at 20°. Data has been truncated to only that within the test time (hence the wing azimuthal angle not starting at zero). As expected, there is a clear reduction in control authority as the wing rotates further from the windward ray ($\phi_{Wing} = 0$), but unfortunately the achieved roll position was limited by the control authority of the singular wing in combination with the test time and inertia of the model - if lower inertia, or longer test time, the model would rotate through a greater angle

over the course of the test. Future work may include tests that start with all 4 wings deflected at 20°, before returning 3 of the wings to 0° deflection. This would allow an increased roll rate to be generated at the start of the test and allow for more angles to be characterised.

4.5.3.3 Deflection-Pause Tests

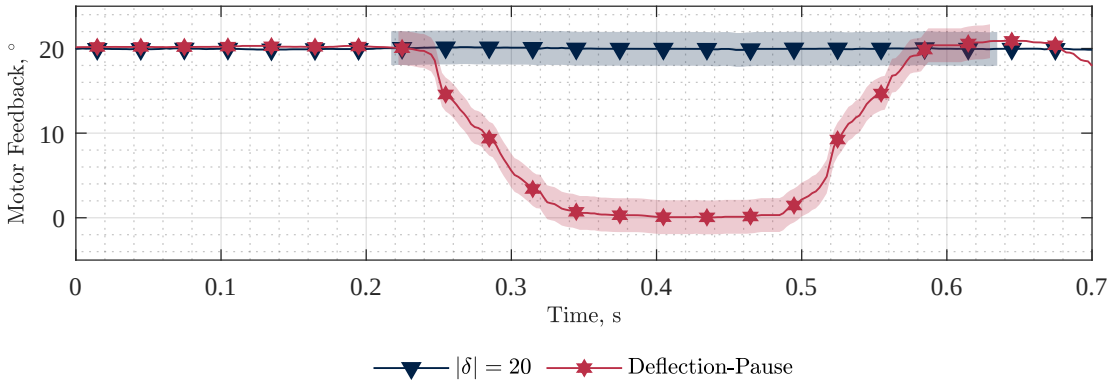

(a) Motor Feedback. Unfortunately, no data was captured for the wing deflections in the 10 degree test.

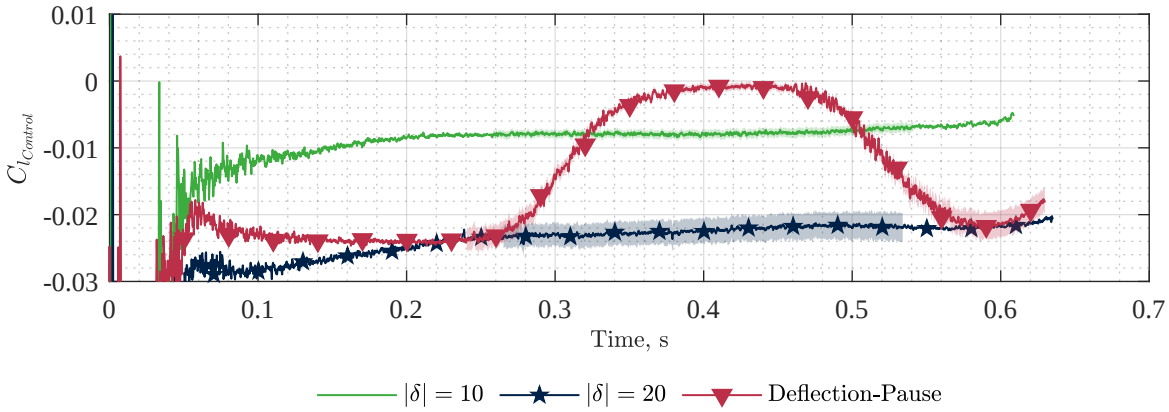

(b) Control effectiveness

Fig. 4.19 Comparison of deflection-pause tests with tests performed with static wing deflections using the quasi-static technique

Fig. 4.19 presents a comparison between tests with static wing deflections and a test with multiple wing deflections using the quasi-static technique at zero degrees angle of attack. Conversely to the equivalent force balance tests, the quasi-static tests begin with a 20° wing deflection as the actuator commands are triggered once the roll rate exceeds a set value. Relative to the force balance tests, it can be seen there is improved agreement between the two sets of tests , likely a result of the battery used to power the actuators being able to supply a greater current. Finally the deflection-pause test exhibits significant overshoot relative

to the 10 ° case whilst the wings are moving. This is due to both the reaction moments and dynamic aerodynamics arising from the compression of the freestream with actuator movement. Further work to characterise the reaction moments may allow extraction of this dynamic control effectiveness.

4.6 Conclusion

This paper has presented experimental results from a campaign leveraging the extended test duration of the recently developed Extended Ludwieg Mode (ELM) to improve the state-of-the-art for control effectiveness studies in hypersonic Ludwieg tunnels. It is demonstrated that for Ludwieg tunnels, it is the duration of nozzle startup period, not the overall rise time of the supply condition traces that serves to excite the natural frequencies of a force measurement system, and that addition of a plenum between the fast acting valve and the nozzle throat can reduce the magnitude of the startup loads imposed on the force balance. It is shown that 6 axis MEMS IMU's are suitable for acceleration compensation in hypersonic Ludwieg tunnels, including use of differentiated gyroscope measurements for moment compensation. Additionally, the paper has demonstrated the ability to characterise multiple wing deflections in a single run, as well as characterise multiple roll angles at angle of attack. With a further increase in test time or faster motors, it would be possible to characterise further wing deflections in a single test. Further improvements may also be made to the quasi-static technique to allow more roll positions to be characterised in a single quasi-static run through scheduling of actuator commands. Overall, this paper has presented significant improvements to the both the quantity and quality of characterisation that can be achieved in a single run, reducing the total number of tests required to characterise a vehicle's control effectiveness and improving confidence in the aerodynamic database generated during vehicle design.

4.7 Acknowledgements

This research was funded by DSTL. The authors would like to thank Mr Christopher Hambidge for his operation of HDT during this campaign. Finally, the authors would like to thank the Structural Dynamics team at AWE Plc for measurement of the cone mass properties.

Statement of Authorship

Paper Title:

Control effectiveness studies in hypersonic Ludwieg Tunnels

Paper Status:

Unpublished and unsubmitted work written in manuscript style

Authors of the original paper:

Hillyer, J., Doherty, L.J., Bacic, M.B, McGilvray, M.

Author contribution:

- **Hillyer, J.** : Lead author, conceptualisation, data curation, formal analysis, and writing.
- Doherty, L.J. : Supervision as Primary Supervisor.
- Bacic, M.B. : Supervision as Secondary Supervisor.
- McGilvray, M. : Supervision as Principle Investigator.

Student Confirmation: **Date:** 13/01/2024

Supervisor Confirmation: **Date:** 13/01/2024

Chapter 5

Effect of shape change on control effectiveness

Preamble

One of the research aims of this thesis was to investigate the effect of shape change on control effectiveness. This chapter presents experimental results from testing of a 10 degree half angle cone fitted with all moving wings in the Oxford High Density Tunnel. Two nosetips are tested, with bluntness ratios 1.7% and 17%, in addition to 6 permutations of all moving wing geometries: one sharp, one blunt and a further 4 geometries simulating varying degrees of leading and trailing edge burnthrough of the control effector. The experimental data presented in this chapter was captured during the same experimental campaign as those in Chapter 4, and consequently the techniques discussed in that chapter were not fully validated and thus unable to be used. This chapter is currently unsubmitted but written in manuscript format for submission to journal after the thesis is completed. A statement of authorship is provided at the end of the chapter and all references are given at the end of the thesis.

Associated Appendices:

N/A

Abstract

In the hypersonic regime, aerodynamic control surfaces are subject to extreme aerothermal loading owing to the local shocks arising from their deflection exacerbating the already harsh aerothermal environment characteristic of hypersonic flows. Control effectors are typically protected by ablative coatings, but this comes at the expense of changes to the outer mold line of the effector, potentially affecting their control effectiveness (the control moment they are able to produce). This paper presents experimental results from testing of a 150 mm base diameter, 10 degree half angle cone with all moving wings in the Oxford High Density Tunnel, investigating the effect of shape change on control effectiveness. Two nosetips, with bluntness ratios of 1.7% and 17%, were tested, along with 6 variations of wing shape. At zero degrees angle of attack, it was found that increased nosetip bluntness ratio decreases the control effectiveness provided by all moving wings, owing to the increased thickness of the entropy layer and consequent low total pressure zone close to the cone surface. It was found that blunting of the leading edge of the all moving wing also resulted in a reduction in control effectiveness, though this effect was negligible in comparison with the effect of nosetip blunting. Similar trends were shown at 6 degree angle of attack, though the reduction in control effectiveness resulting from leading edge blunting was reduced. The remaining 4 all moving wing geometries were tested in conjunction with the 17% bluntness ratio nosetip, 3 simulating varying degrees of trailing edge burnthrough and another simulating the effect of leading edge burnthrough. For all of the trailing edge burnthrough cases, the control effectiveness was found to be lower than that expected if control moment were simply proportional to wing area. This was attributed to a pressure relieving effect as a consequence of adding burnthrough, whereby the total pressure distribution on the remaining wing is decreased relative to the total pressure on the non-damaged wing. In the case of leading edge burnthrough, the measured control effectiveness was greater than that expected if control effectiveness proportional to wing area, which was attributed to the total pressure distribution on the non-damaged wing, which may exhibit a region of low total pressure in the removed section as a consequence of its proximity to the curved shock produced by the blunt wing leading edge.

5.1 Introduction

In any speed regime, the backbone of flight vehicle design is the generation of a high quality aerodynamic database in the form of aerodynamic coefficients. Values for these coefficients can be numerically predicted using Computational Fluid Dynamics (CFD) [1–5], experimentally measured in ground test facilities [6–8], or generated from flight data [9–11]. Characterisation of the vehicle with these techniques allows assessment of the vehicle in terms of key performance indices. Two common performance indices for hypersonics are the vehicle controllability and manoeuvrability, both of which are functions of the control effectiveness - how much control moment the control effectors are able to produce.

Currently undergoing a resurgence of interest for both military and civilian applications, hypersonics is an inherently complex flight regime characterised in part by the extreme aerothermal environment that vehicles are subject to. This is exacerbated for the control effectors, typically aerodynamic control surfaces in the continuum regime, as a consequence of the shock generated by their deflection inducing local heating and potentially causing separation [18, 19, 137, 71, 5, 7]. At higher flight speeds, regions of high thermal loading (e.g. vehicle nosetip, control effectors) are typically protected by ablative materials. Ablatives chemically react with the flow to absorb energy, though this comes at the expense of shape change - typically manifesting as regression of leading edges (blunting) and development of roughness patterns - which can affect the overall vehicle aerodynamics and resultant control effectiveness. The effects of increasing nosetip bluntness is relatively well studied, with papers focusing on boundary layer transition [73–79, 138] and overall aerodynamics/vehicle dynamics [139, 80, 50, 81, 50, 47], though none have investigated the effects of blunting on control effectiveness. It has been demonstrated that increases in nose bluntness increase the thickness of the entropy layer and associated low total pressure zone, and hence it is expected that increasing nose bluntness will decrease the control effectiveness of aerodynamic control surfaces. Holden [82] presents an overview of studies performed at CUBRC investigating the effect of roughness, including a brief mention of control effectiveness measurements - though details on experimental setup are sparse. In this case, surface roughness was found to thicken the boundary upstream of the control surface, thereby reducing its control effectiveness. Other studies on surface roughness [140, 141], have found that roughness affects the local shear stress distributions, altering the overall aerodynamic forces acting on the vehicle.

This paper presents results from an experimental investigation of the effect of shape change on a vehicles control effectiveness using the Oxford High Density Tunnel (HDT), a Ludwieg Tunnel. The experimental model was a 10 degree half angle cone, base diameter 150 mm, fitted with four all moving wings. Two nosetips were tested, with bluntness ratios of 1.7% and 17%, as well as 6 permutations of all moving wings. The all moving wings tested

are one sharp, nominal, wing, one blunted wing and 4 variants simulating differing levels of leading/trailing edge root burnthrough. Use of a Ludwieg tunnel for these experiments allows simulation of Mach number and Unit Reynolds number whilst "turning off" high temperature flow physics (e.g. chemical reactions, local changes of specific heat ratio, etc), thereby isolating aerodynamic effects.

The remainder of this paper is organised as follows: a description of the facility is given in Section 5.2 and a description of the experimental model, including the wing geometries used in the experiments, is given in Section 5.3. An explanation of the data reduction techniques is given in Section 5.4, and experimental results are presented in Section 5.5. Finally, conclusions are drawn in Section 5.6

5.2 Facility

All tests in this paper were performed in the Oxford High Density Tunnel (HDT), a Ludwieg tunnel located at the Oxford Thermofluids Institute, University of Oxford [121]. A schematic of the facility is given in Fig. 5.1, featuring a barrel of internal diameter 152 mm and length 17.35 m. The barrel is separated from the nozzle plenum by an upstream facing plug valve. The HDT features four operational nozzles, each with an exit diameter of 351 mm, covering the range of Mach 4 to Mach 7. The facility barrel can be heated to 550 K, and has a maximum pressure rating of 275 bar.

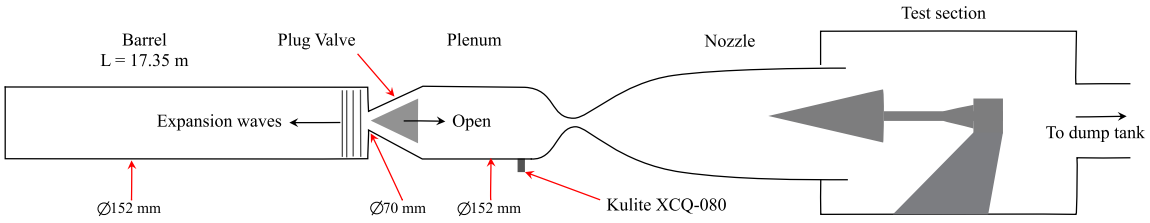

Fig. 5.1 Schematic of HDT. Adapted from [122]

The HDT is currently capable of being operated in 4 modes: 1) Ludwieg Mode, 2) Light Isentropic Compression Heating (LICH), 3) Extended Ludwieg Mode (ELM) and 4) Plenum Augmented Ludwieg Mode (PALM). PALM, a steady blowdown mode, is the most suitable for force measurements owing to its increased steady test duration, but unfortunately was still in active development and was not available in this campaign. Consequently, all testing in this paper was performed in ELM, a quasi-steady blowdown mode offering significantly more test time than standard Ludwieg Mode.

5.2.1 Instrumentation

Nozzle supply conditions were measured using sensors mounted in the facility plenum. The supply pressure was measured using a flush mounted Kulite XCQ-080 transducer, and total temperature calculated from Aspirated Thermocouple (ATC) data using the processing outlined in [122, 123]. The Kulite was amplified with a Fylde FE-H379-TA differential amplifier, and the ATC with an Adafruit AD8495 amplifier. Both supply condition sensors were recorded at 100 kHz on NI PXIE 6368 cards housed in a NI PXIe-1092 chassis (henceforth referred to as the NI DAQ).

5.2.2 Schlieren

Schlieren was recorded on a Photron MiniUX100 using a folding Z-type setup with a horizontal knife edge. The light source was a green Luminus CBT-120 LED, and 300 mm diameter, 1660 mm focal length mirrors were used. Background correction, in which the average of the pre-test wind-off frames are subtracted from the wind-on images, was used to remove non-flowfield imperfections.

5.3 Experimental Model

This section provides an overview of the experimental model used in this testing. The same baseline model was used for all testing, with shape change attained by swapping either the nosetip or the all moving wings.

5.3.1 Geometry

The experimental model consisted of a 10 degree half angle cone, approximately 150 mm base diameter, fitted with 4 all moving wings in an X configuration. Fig. 5.2 shows the experimental model installed in the test section on a two axis traverse used to position the model in pitch and yaw. The traverse has a usable motion range of ± 15 degrees in pitch and ± 5 degrees in yaw and is not able to be moved during the test.

In order to reduce root gap effects, the wings are situated on flats machined into the cone surface. These flats themselves are 3 degree expansions relative to the cone surface, chosen to give sufficient space for the full range of wing motion whilst minimising the static pressure decrease through the expansion. There are 2 options for nosetip: a nominally sharp nosetip with a leading edge radius of 1.25 mm, and a “blunt” nosetip with a 13 mm radius, giving bluntness ratios of 1.7% and 17% respectively. All cone components, with the exception

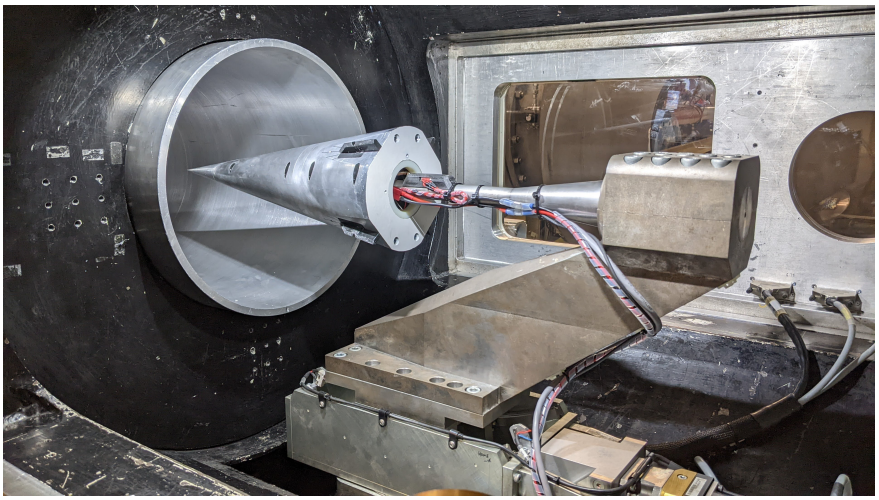

Fig. 5.2 Experimental model installed in the test section in force balance configuration

of the wings and the blunt nosetip, were manufactured from Aluminium 7075 T6, and a summary of the model properties is given in Table 5.1.

Table 5.1 Summary of model properties

Property	Unit	Value	Uncertainty
Half angle	$^\circ$	10	-
Sharp nosetip radius	mm	1.25	-
Blunt nosetip radius	mm	13	-
Base diameter	mm	148.5	± 0.2
Bluntness ratio, sharp nosetip	%	1.7	-
Bluntness ratio, blunt nosetip	%	17	-
S_{ref}	m^2	0.0173	± 0.0001
Inertia, J	$kg\,m^2$	0.0068	$\pm 8.5 \times 10^{-5}$

5.3.2 All Moving Wings

A total of 6 different wing designs were tested in these experiments, comprising of a sharp "reference" wing and 5 shape changed variants. The variants in wing design are shown in Fig. 5.3. The baseline geometry can be seen to have a length of 70 mm and pivoted at 51.5% chord. The first non-standard wing has a blunt leading edge, whilst the others feature differing levels of leading or trailing edge root burnthrough to simulate damage to the control effector in addition to the blunt leading edge. The use of blunt leading edge for the burnthrough wings was motivated by the expected vehicle shape change over the course

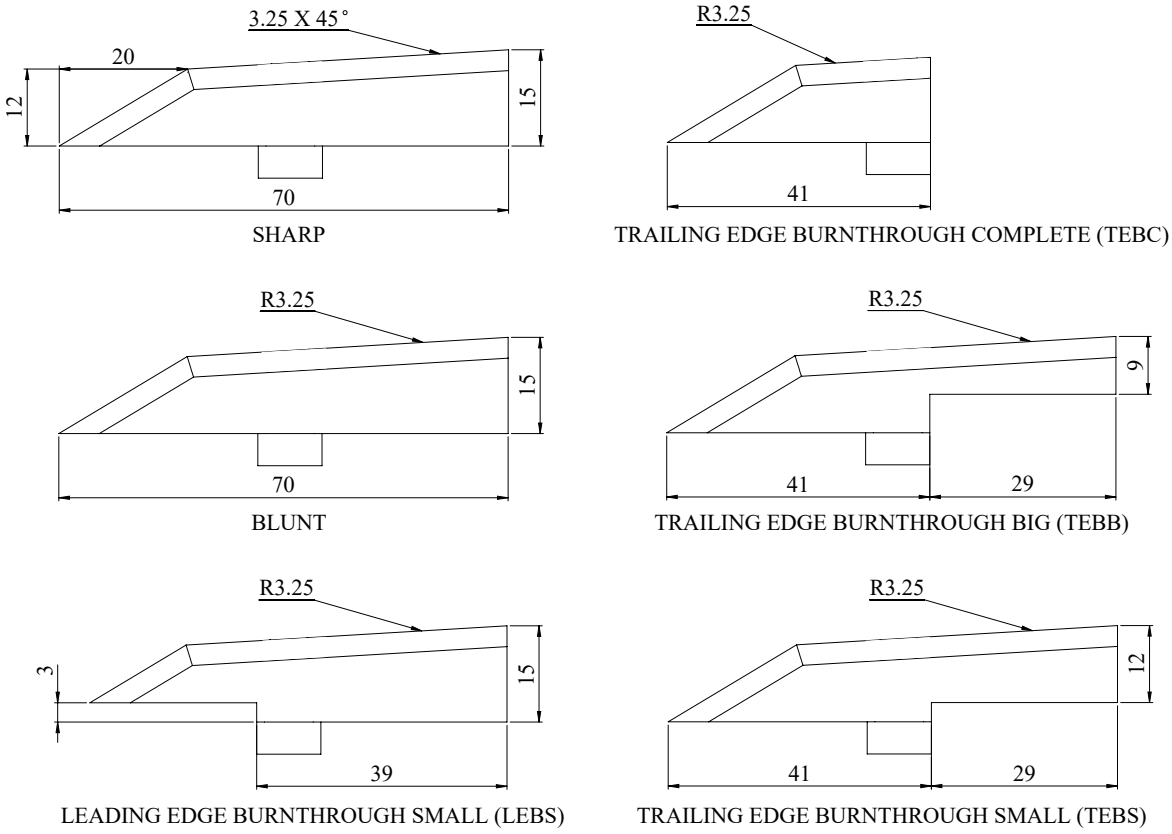

Fig. 5.3 All moving wing geometries used in this experiment. All dimensions are in millimetres

of the trajectory - at the point where the heat load on the effector has accumulated to cause burnthrough, it is highly likely that the leading edge would have already begun to recess. All burnthrough was simulated by removing a portion of the wing from the edge (leading or trailing) to the hinge point, and consequently the Leading Edge Burnthrough Small (LEBS) and Trailing Edge Burnthrough Small (TEBS) have different areas removed despite having a constant depth of burnthrough. A summary of the effective areas of each wing variant is given in Table 5.2. All wings were 3D printed on a Stratasys Objet 30 with verablack resin, and press fit onto the output shaft of the DFRobot SER0044 servo motors used for wing positioning. As discussed in Chapter 4, use of a motor to drive the wings allows for multiple wing deflections to be characterised in a single experiment. However, in all cases in this paper, the presented data arises from static experiments with static wing deflections.

5.3.3 Force Balance

The force balance used in these experiments was an ATI-Mini45, calibration type SI-145-5. A summary of its load ratings and natural frequencies are given in Table 4.3. The force balance has three sensing beams, with applied loads being measured by silicon semiconductor strain gauges arranged in six half-bridge pairs. Simple bridge completion circuity, mounted in the test section, was used so the force balance could be amplified by a Fylde FE-H379-TA differential amplifier and recorded on the NI DAQ at 100 kHz. The manufacturer provided static calibration was used after verification of its accuracy with an in-house static calibration.

5.3.4 Onboard Data Acquisition

The experimental model was fitted with two onboard DAQs: a "pressure" DAQ and a "control" DAQ, both triggered with a TTL from the NI DAQ. The pressure DAQ recorded 4 Honeywell HSCMAND015PASA5 pressure transducers at 4 kHz, recess mounted on the cone flats (approximately 14 mm upstream of wing tips - see Fig. 5.4a) and used for model alignment, as well as a 6 axis TDK ICM-42688-P IMU at 32 kHz, located on the cone centreline and used for acceleration compensation of the force balance. The control DAQ was additionally used to set the position of the wings between tests. The internal layout of the model, with instrumentation locations annotated is shown in Fig. 5.4b.

5.4 Data Reduction

This section presents an explanation of the data reduction used in this paper, detailing calculation of freestream conditions, an explanation of co-ordinate systems used, the process for isolating control effectiveness from the force measurements and finally a summary of the process used for uncertainty calculations.

Table 5.2 Summary of effective wing areas for each geometry

Wing	Sharp	Blunt	LEBS	TEBS	TEBB	TEBC
Area, mm^2	795	795	650	708	621	385
% Sharp area	100	100	82	89	78	48

Table 5.3 ATI Mini 45 specifications. Note that the natural frequencies listed are for the force balance in isolation. When installed in the model, the additional mass reduces the overall natural frequency of the system [27, 28].

	Full Scale Range	Uncertainty	Natural Frequency
Rolling Moment	5 N m	$\pm$ 0.0625 N m	5.6 kHz

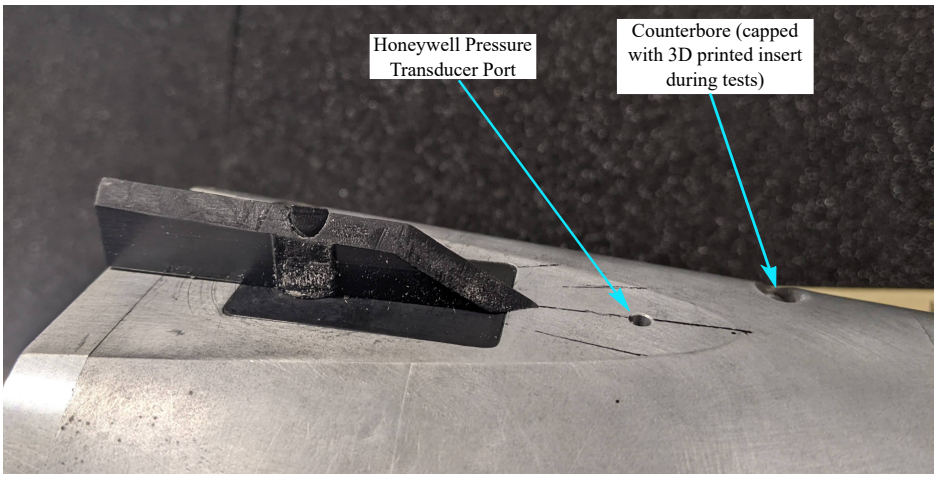

(a) Respective position of the Honeywell pressure transducer ports and the wings on the flats

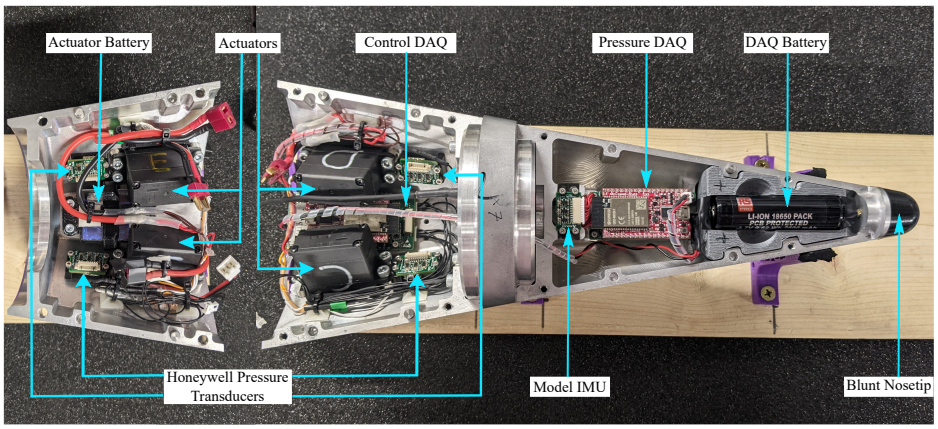

(b) Internal layout of the model

Fig. 5.4 Photo of the experimental model, showing the relative positions of the data acquisition systems, the instrumentation and the actuators.

5.4.1 Freestream Conditions

Freestream conditions were calculated assuming isentropic expansion of calorifically perfect air from measured nozzle supply pressure and calculated total temperature data. Total temperature was calculated from plenum based ATC measurements using the processing

Table 5.4 TDK ICM-42688-P IMU full scale range and uncertainties. All taken from manufacturers datasheet

	Full Scale Range	Uncertainty
Gyroscopes	$\pm 2000\,^{\circ}\,s^{-1}$	$\pm 2\,^{\circ}\,s^{-1}$

in [122, 123]. Mach number was assumed to be constant across the test, with the value taken from the measured centreline Mach Number from a Pitot rake shot at the chosen fill conditions. Viscosity was calculated using Keyes relation [130]. A summary of the input uncertainties for the supply condition calculations is given in Table 5.5.

Table 5.5 Summary of the input uncertainties to the supply condition calculations

Flow Property	P0	T0	M	
			LM	ELM
Sensor	Kulite XCQ-80	ATC	Assumed Constant	
Value	Measured	Measured	7.04	7.00
Uncertainty	$\pm$7000 Pa (0.1% FSO)	$\pm$15 K	$\pm$0.06	$\pm$0.071

5.4.2 Coordinate Systems

There are 3 primary axis systems relating to the aerodynamics of a test article in a wind tunnel test section, all of which have origins at the vehicle centre of mass[1]:

1. *Inertial/Laboratory fixed axes*: x axis is positive downstream, z axis is aligned with the gravity vector and y axis forms the right hand system.

2. *Body Axes*: This is a coordinate system that moves with the test article. The x axis lies in the plane of symmetry of the model, positive towards the nose, y axis points to starboard and the z axis forms a right handed axis system. All moments (yawing, pitching, rolling) are expressed about these axes, and the Eulerian angles (yaw ψ, pitch θ, roll ϕ) are the angles formed between these axes and the inertial axes. Rolling moment is defined as positive by the right hand screw rule about the body axis, and wing deflections are defined as positive when they act to create a positive rolling moment. Noting that all rolling moments presented in this paper are negative, wing deflections are presented as magnitudes rather than absolute values.

[1]The origin of the inertial reference frame is arbitrary, and defined at the centre of mass in this work for simplicity

3. *Wind axes*: The x axis is defined along the velocity vector of the test article relative to the fluid, the z axis lies in the plane of symmetry of the test article and the y axis forms the right handed axis system. In flight, the definition of the x axis inherently accounts for the motion of the body and the relative wind, but in a sting based experiment where the model is constrained this vector simply reduces to the freestream velocity vector. All body forces (Lift, Drag, Sideforce) are expressed in these axes.

The most significant angles in terms of the vehicle aerodynamics are the angle of attack, α, and angle of sideslip, β, which define the orientation of the body to the effective wind. For a constrained experiment where the model exhibits no translation, these angles reduce to simply the angle between the freestream velocity vector and the body x and y axes, respectively. For these tests, the body axes were aligned with the freestream velocity vector using the Honeywell pressure sensors, and so movement of the traverse from that aligned position directly affects the model angle of attack and sideslip.

The force balance and IMU's used in these experiments have their own axis systems which rotate with the body axes and so are transformed into the body axes prior to data analysis.

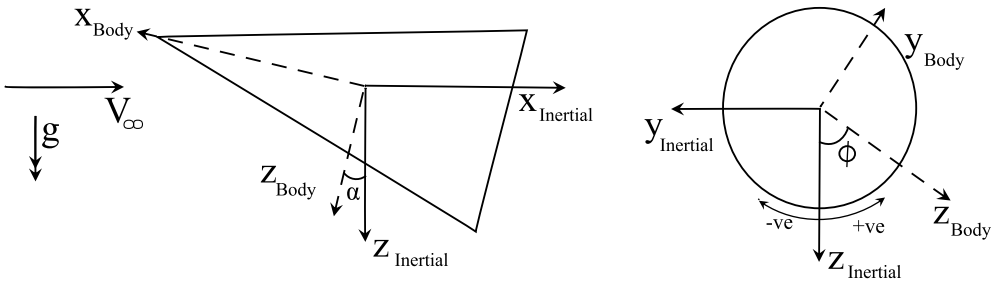

Fig. 5.5 Definition of the body (dashed lines) and inertial (solid lines) axes used in this campaign. In this figure, the freestream velocity vector is assumed to be aligned with the x axis of the inertial frame

5.4.3 Control Effectiveness

The primary measurements in this paper are of roll control effectiveness. In the same way as for the Lift and Drag, the aerodynamic rolling moment, L_{aero}, produced by a flight vehicle can be related to the rolling moment coefficient, C_l, by the dynamic pressure and a reference area as per Eq 5.1:

$$L_{aero} = qS_{ref}l_{ref}C_l \tag{5.1}$$

Where q is the dynamic pressure, S_{ref} is a reference area (for this analysis, cone base area) and l_{ref} is a reference length. The reference length for roll is typically the vehicle span, b, which will be used in all subsequent equations.

In flight dynamics, C_l is typically expressed as a first order Taylor series expansion of perturbations of non-dimensionalised flight states about an equilibrium condition. The coefficients in these equations are typically broken down into groups of static and dynamic coefficients, where static coefficients are functions of the vehicle shape and attitude, and the dynamic coefficients are functions of the time history of its motion. In this analysis, the rolling moment coefficient will be taken to have the form given by Eq 5.2, where the contributions from static aerodynamics is separated into contributions from the vehicle shape and the control effectors:

$$C_l = \underbrace{C_{l_{Body}}(M,\alpha,\beta,\phi) + C_{l_{Control}}(M,\alpha,\beta,\phi,\delta_1,...\delta_n)}_{\text{Static Coefficients}} + C_{l_{Dynamic}}(M,\dot{\alpha},\dot{\beta},\dot{\phi},\dot{\delta_1},...\dot{\delta_n}) \quad (5.2)$$

Where $C_{l_{Body}}$ is the rolling moment coefficient produced by the vehicle at that attitude with no control effector deflections, $C_{l_{Control}}$ is the control effectiveness and its dependency on α, β, and ϕ is essentially a measure of how windward the control effector is, and $C_{l_{Dynamic}}$ are the contributions from dynamic aerodynamic derivatives. For every configuration tested, a measurement of $C_{l_{Body}}$ was attained from a test with no control effector deflection, allowing $C_{l_{Control}}$ to be determined at each attitude for varying control effector deflections.

5.4.3.1 Acceleration Compensated Force Balance

Though the Mini45 is a 6 axis force balance, only the rolling moment measurements are presented in this work. Hence, this section presents an outline of the data reduction used for compensation of those signals. As the force balance and the IMU were recorded at different sample rates (100 and 32 kHz, respectively), some resampling is necessary. In this work, it was chosen to downsample both traces onto a common timebase to avoid interpolation of data points complicating the uncertainty calculations. The final point to be addressed before moving onto the explanation of the data reduction is the time alignment of the IMU and force balance data as these were recorded on different DAQs. This was achieved with a least-squares optimisation process, whereby the rolling moment coefficient was assumed constant for a set test window (i.e. rolling moment directly follows supply pressure trace) and time alignment shifted to minimise the deviations of the resultant acceleration compensated measurement from a straight line of best fit through the unfiltered/oscillatory data. This

process is not dissimilar to the processed used in Störkmann [28], though in that case the least-squares fit was used in determination of the inertia matrix of the model.

The primary data reduction equation for acceleration compensation is given by Eq. 5.3:

$$L_{AC} = L_{UC} - J * \ddot{\phi}_{measured} \tag{5.3}$$

Where L_{AC} and L_{UC} are the acceleration compensated and uncompensated rolling moment, respectively, J is the model inertia about the cone axis and $\ddot{\phi}_{measured}$ is the angular acceleration, in this case attained from differentiation of the gyroscope readings.

Hence, the process for performing acceleration compensation is as follows:

1. Transform IMU axes into body axes
2. Convert from $^{\circ}\,\mathrm{s}^{-1}$ to $\mathrm{rad}\,\mathrm{s}^{-1}$
3. Pre-smooth the angular rates with a 3ms moving average filter.
4. Downsample all force and angular rate data onto a common timebase (4 kHz).
5. Differentiate angular rates to attain angular accelerations.
6. Smooth angular acceleration data with a 2.5ms moving average filter.
7. Perform the acceleration compensation as per Eq 5.3

Where the smoothing stages are required to account for the inherently noisy differentiation process. The overall rolling moment measured by the force balance is then given by Eq. 5.4:

$$L_{AC} = L_{aero} + L_{CoG} + L_{Reaction} + L_{offset} \tag{5.4}$$

Where L_{CoG} is the rolling moment arising from displacement between the force balance sensing origin and the model centre of gravity, $L_{Reaction}$ are contributions from the reaction moments arising from conservation of angular momentum with all moving wing actuation and L_{offset} is a reported rolling moment arising from zero bias of the strain gauges. If the force balance is zeroed prior to the test, the output, L_{AC}, then reduces to L_{aero} (evaluated without the contributions from model motion), plus the reaction moments as per Eq 5.5:

$$\begin{aligned} L_{AC} = qS_{ref}b\left(C_{l_{Body}}(M,\alpha,\beta,\phi) + C_{l_{Control}}(M,\alpha,\beta,\phi,\delta_1,\ldots\delta_n) + C_{l_{Dynamic}}(M,\dot{\delta}_1,\ldots\dot{\delta}_n)\right) \\ + L_{Reaction} \end{aligned} \tag{5.5}$$

With the reaction moments and dynamic contributions vanishing for experiments with static wing deflections (assuming steady freestream conditions).

5.4.4 Uncertainties

This section presents a summary of the input uncertainties used in this paper. All uncertainties have been propagated through the data reduction techniques outlined previously using the jitter methodology [129], with a 5 point stencil and a 0.2% perturbation magnitude. The only exception is the acceleration compensation (Eq. 5.5). In this case, the compensation serves only to remove oscillations about the mean value rather than affecting the mean value itself, and consequently the presented uncertainties are those provided by the force balance manufacturer.

5.5 Experimental Results

This section presents the experimental results. It begins with a discussion of the supply conditions and model alignment, before discussing results for the nominal case, consisting of sharp nosetip and sharp wings. Finally, the effect of leading edge blunting and wing shape variations are presented.

5.5.1 Supply Conditions

All tests in this paper were performed at Mach 7 with fill conditions of 8 bar and 500 K, corresponding to a 38km altitude flight condition at one to five scale. Typical supply condition traces of the HDT operating at this condition in ELM are shown in Fig. 5.6, producing a steady decrease in supply pressure and unit Reynolds number for approximately 400 ms.

5.5.1.1 Model Alignment

There are 2 primary methods for determining the alignment of the model with the freestream velocity vector, both of which leverage its broadly axisymmetric nature: 1) Orthogonal Pressure Sensors (identical when aligned) and 2) Lift and sideforce (0 when aligned). Fig. 5.7 shows a typical set of pressures and forces measured with the model at its aligned location. It can be seen there is excellent agreement between the pressure sensors across the test, with the exception of the North East sensor for $0.15 < t < 0.25$ s. This is likely a result of this sensor having a slightly more recessed mounting due to a manufacturing defect. The lift and

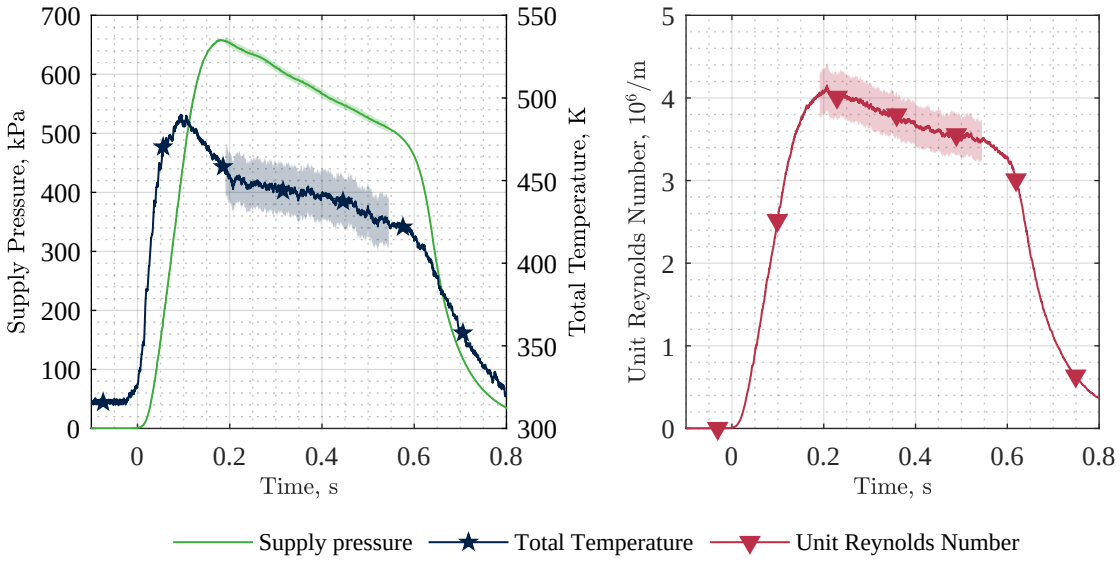

Fig. 5.6 HDT Nozzle supply conditions used in these experiments

sideforce show good agreement, both starting with oscillations about 0 N but exhibiting a slight upwards trend over the course of the tests.

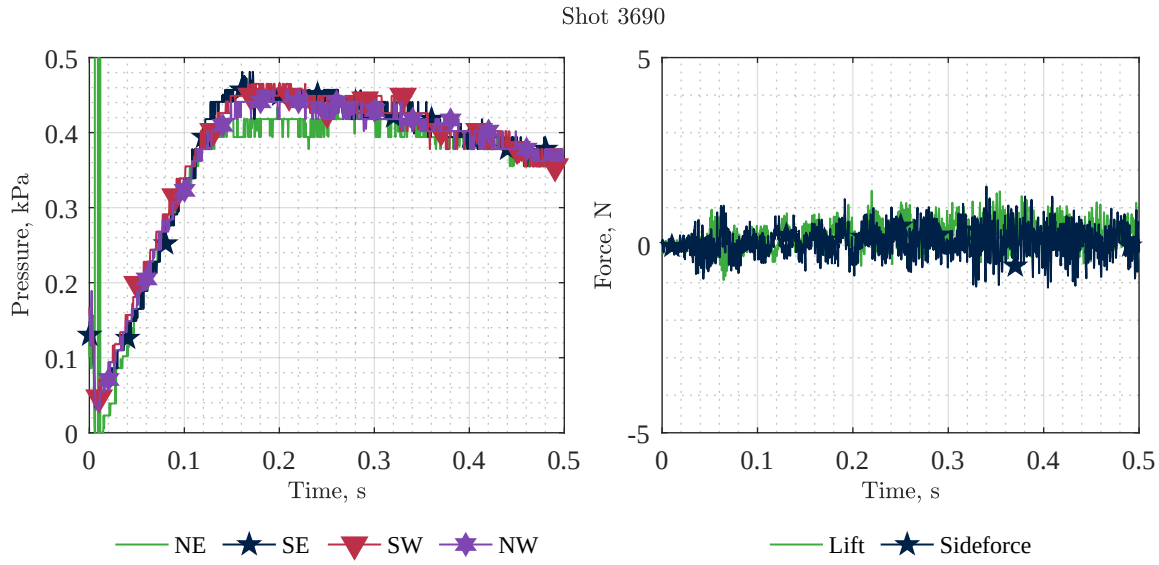

Fig. 5.7 Typical pressures and acceleration compensated forces from an “aligned” shot

5.5.1.2 Freestream uniformity

Noting the results from Oberkampf [15], where it was found that contributions to the overall uncertainty in the measurement of control effectiveness were dominated by freestream

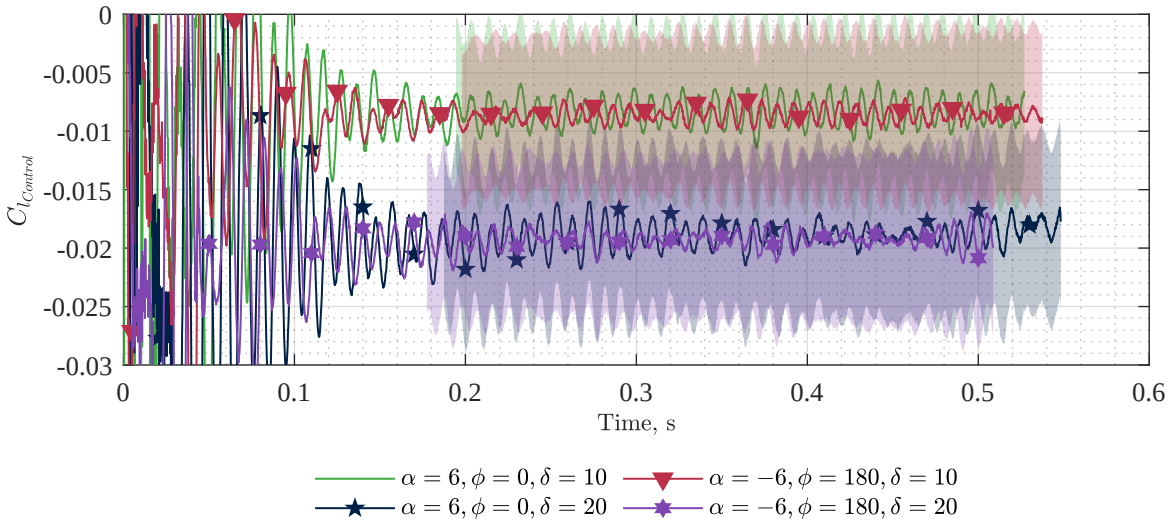

Fig. 5.8 Investigating the effect of freestream non-uniformity on measured control effectiveness

non-uniformity as opposed to instrumentation uncertainties, two sets of tests at nominally identical model attitudes but different positions were performed: one set at 6 degrees angle of attack and zero degrees roll, and another at -6 angle of attack and 180 degrees roll. The results of these tests are shown in Fig. 5.8, demonstrating excellent agreement between the two sets of tests and showing that the uncertainty in these measurements is dominated by the instrumentation and data reduction techniques as opposed to the uniformity of the freestream.

5.5.2 Nominal Case - Sharp Nose, Sharp Wings

This section presents control effectiveness measurements taken with the model in its nominal configuration - “sharp” nose and sharp wings. It presents a comparison of the control effectiveness at zero and 6 degrees angle to attack, including a breakdown of the relative contributions to overall control effectiveness from the windward and leeward control effectors at angle of attack.

Fig. 5.9 presents a comparison between the control effectiveness at zero and 6 degrees angle of attack. Firstly, it can be seen that the control effectiveness is broadly linear through the 0 to 15° wing deflection range, with a non-linear increase in control effectiveness for the 20° case for both angles of attack. The cause of this non-linear increase is currently unknown, but may be a result of boundary layer transition ahead of the wings. It can also be seen that the control effectiveness is essentially identical between the two attitudes. This is unexpected, indicating that the gain in control effectiveness for the windward wings is cancelled out by the decrease in control effectiveness for the leeward wings.

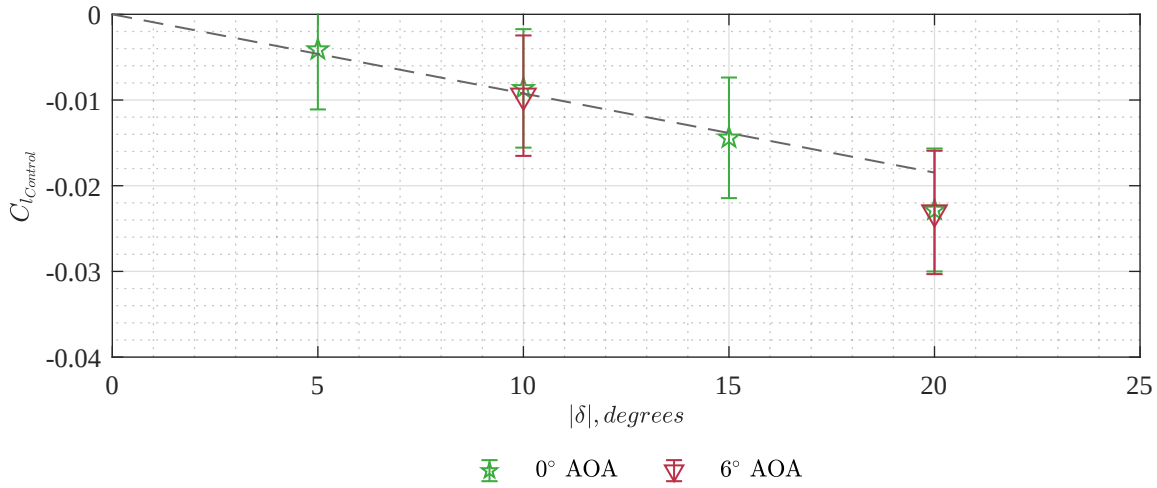

Fig. 5.9 Control effectiveness at with the cone at zero and 6 degrees angle of attack in the nominal model configuration, with a linear fit through 0 to 15 degrees wing deflection overlaid

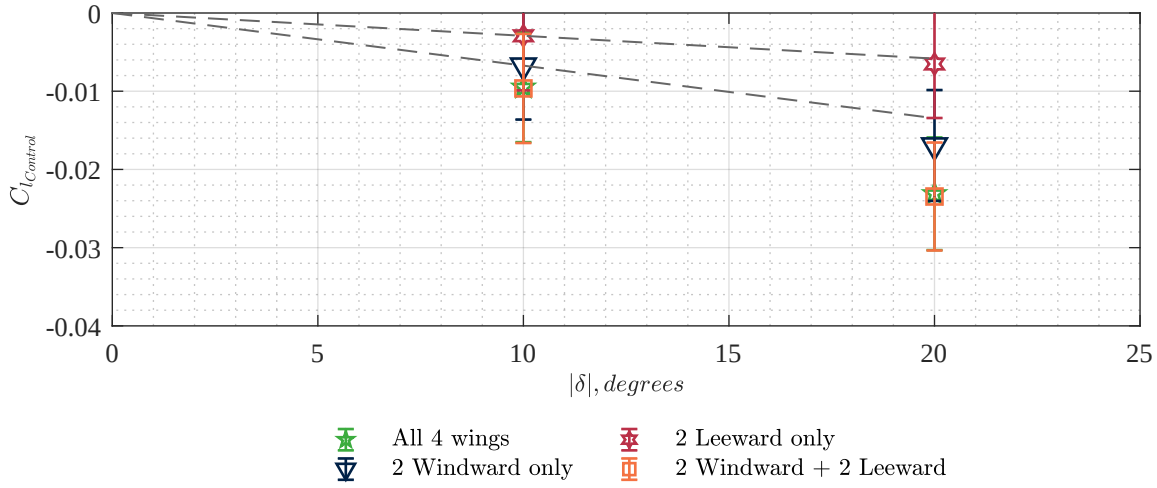

Fig. 5.10 Contributions to the overall control effectiveness from the leeward and windward control effectors at 6 degrees angle of attack. Linear fits (based only on 0 and 10 degree wing deflections) are overlaid for the windward and leeward cases only.

To explore the results of matched control effectiveness at the two attitudes, Fig. 5.10 presents results from tests where either only the 2 windward or 2 leeward control effectors were deflected. As expected, the control effectiveness is additive, with the summation of both tests being equal to the tests performed with all 4 wings deflected, demonstrating that there is no interactions between the windward and leeward wings. It can be seen that, as expected, the windward control effectors are more effective, producing approximately 70% and 74% of the overall control moment for the 10 and 20 degree wing deflection cases, respectively.

Interestingly, it can be seen that the leeward control effectiveness is broadly linear across the range of wing deflections tested, likely a result of the thickened leeward boundary layer, and the non-linearity in control effectiveness for the 20° wing deflection results from the windward control effectors. Noting that this non-linearity is also present when the cone is at zero degree angle of attack, this non-linearity likely arises form the interactions of the wing shocks with the boundary layer, as opposed being a result of the boundary layer thickness itself.

5.5.3 Blunting

This section presents experimental results from tests performed with variations of sharp and blunt leading edges for the nosetip and the all moving wings.

5.5.3.1 Zero degree Angle of Attack

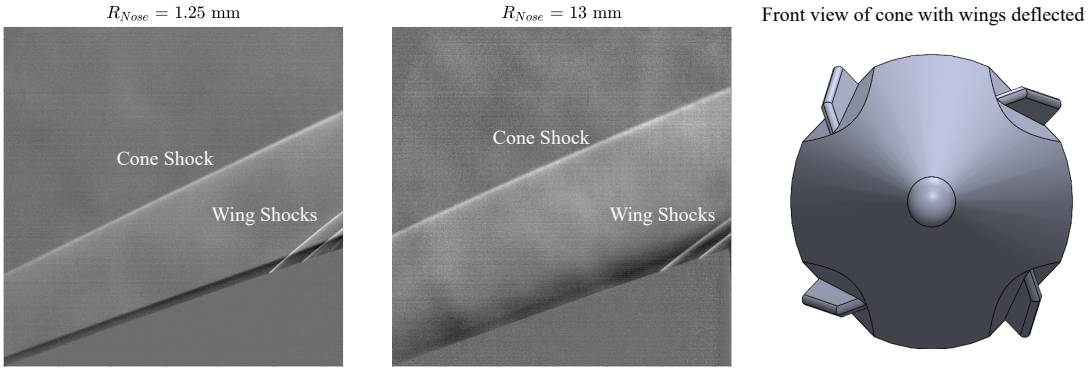

Fig. 5.11 Schlieren of the cone with “sharp” (left) and “blunt” (centre) nosetips, with a CAD generated front view of the cone (right) demostrating different azimuthal angles of wing leading edges. Imaging rear portion of cone, flow is from left to right

Fig. 5.11 presents Schlieren images of the rear of the cone averaged over the quasi-steady test period for tests with sharp and blunt nosetips and 20 degree wing deflections. Three shocks are visible: the cone shock and two shocks at the rear of the cone arising from wing deflection, at different locations due to the different azimuthal angles of the wing leading edges. It can be seen that, as expected, blunting has increased the distance from the cone surface to the cone shock and resulted in a less well defined boundary layer. The shock angles are similar for both cases, with “sharp” shock angle of approximately 13.1 degrees and 14.5 degrees for the blunt nosetip.

Fig. 5.12a presents measurements of control effectiveness at zero degrees angle of attack with permutations of nosetip and wing blunting and Fig. 5.12b presents this normalised by

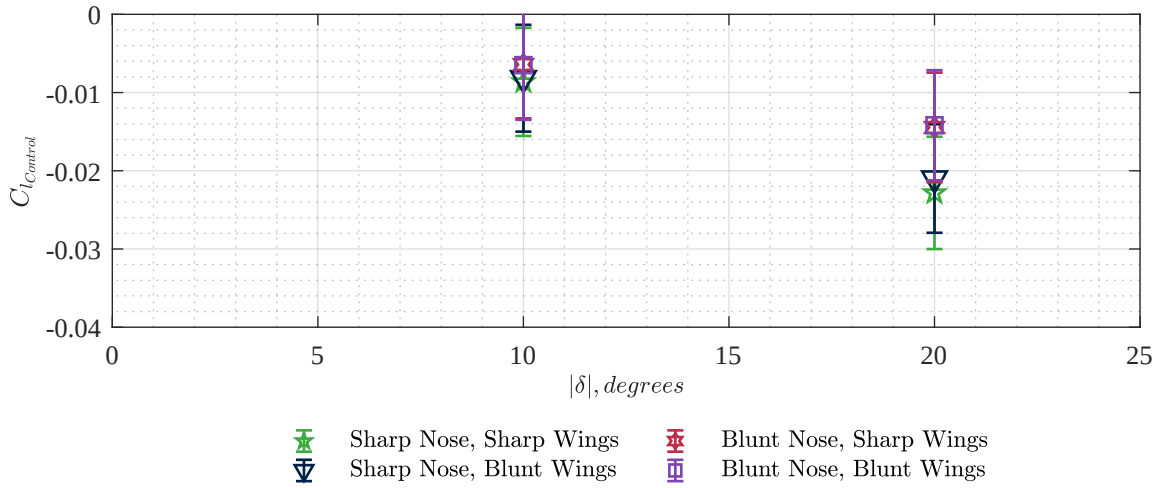

(a) Control moment coefficient

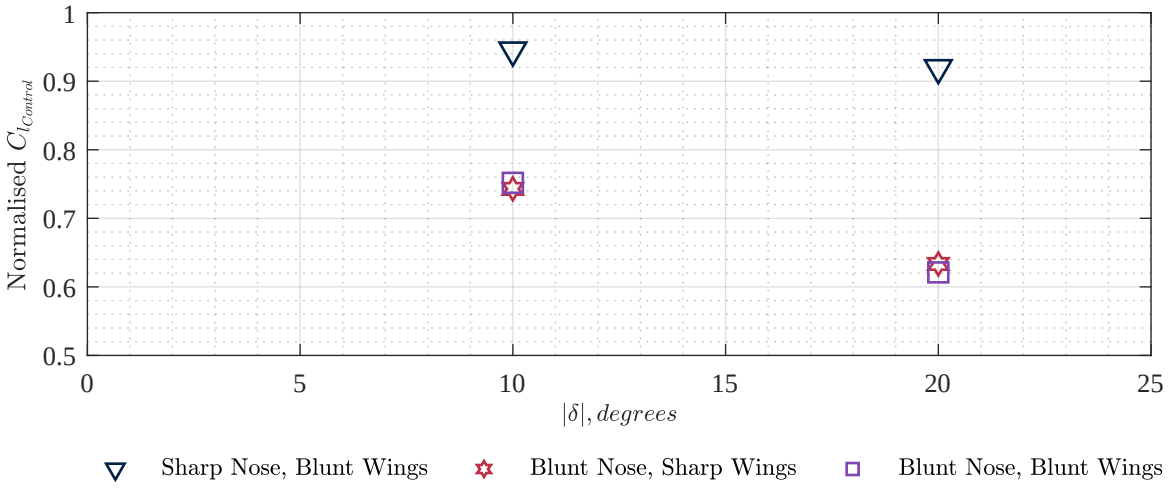

(b) Control moment coefficient normalised by nominal case (sharp nose, sharp wings)

Fig. 5.12 Bluntness variations at zero degrees angle of attack

the nominal (sharp nose, sharp wings) case. As expected, blunting of the nosetip results in a significant decrease in control effectiveness, owing to the increased region of influence of the entropy layer and associated increased thickness of the low total pressure zone close to the surface. It can be seen that for the sharp nose case, addition of blunting to the wings results in a minor reduction in control effectiveness, with reduction increasing with increasing wing deflection. However, it can also be seen that for the blunt nose case, blunting of the wing results in a negligible difference in control effectiveness.

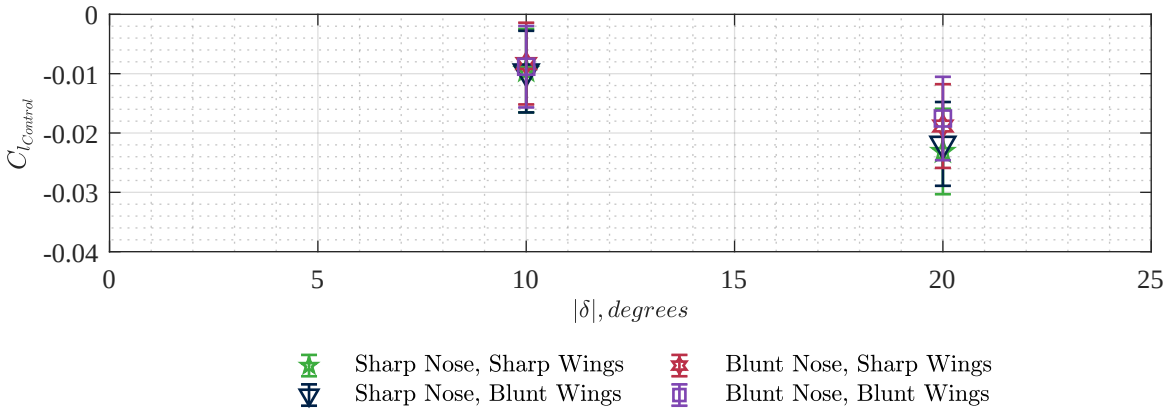

(a) Control moment coefficient

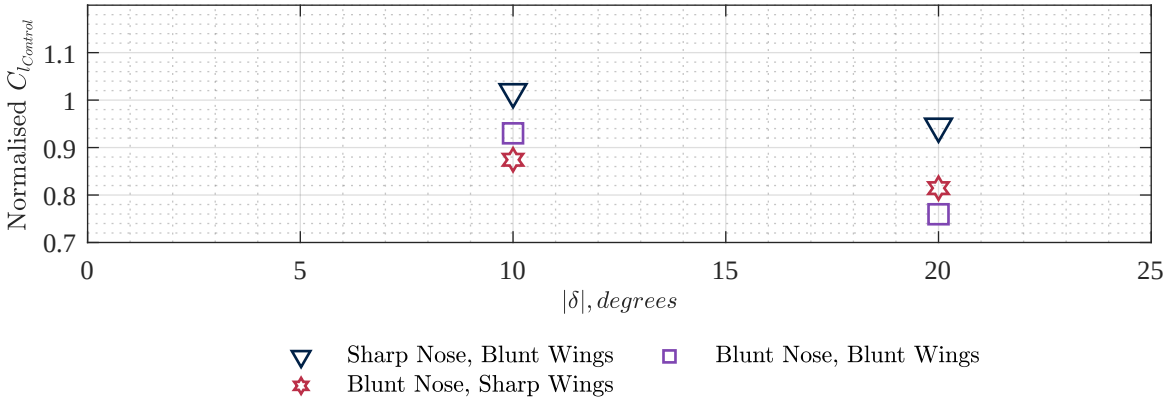

(b) Control moment coefficient normalised by data from the nominal configuration at this attitude (sharp nosetip, sharp wings, 6 degree angle of attack)

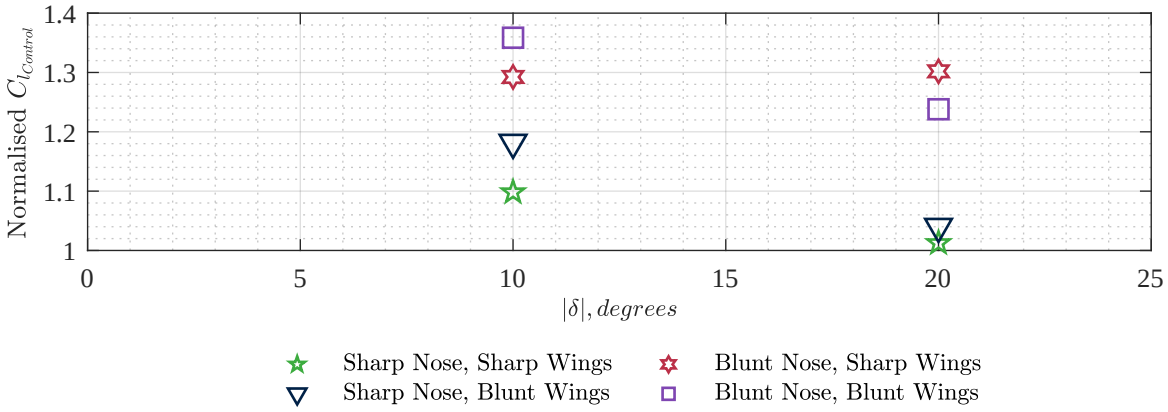

(c) Control moment coefficient normalised by data from that configuration at 0 degrees angle of attack (i.e. how control effectiveness changes with angle of attack for each configuration)

Fig. 5.13 Bluntness variations with the cone at six degrees angle of attack

5.5.3.2 Six Degree Angle of Attack

Fig. 5.13 presents data attained at 6 degrees angle of attack, with Fig. 5.13a presenting the control moment coefficient attained for each model bluntness variation, Fig. 5.13b presenting control moment coefficient normalised by the nominal data (sharp nosetip, sharp wing, 6 degree angle of attack), and Fig. 5.13c presenting control moment normalised by each configurations corresponding 0 degree angle of attack case. It can be seen from Fig. 5.13b that whilst the addition of blunting still reduced the control authority, particularly for blunting of the nosetip, this effect is reduced relative to the 0 degree angle of attack case (cf Fig. 5.12b). This is likely a result of the compression of the low total pressure zone on the windward surface. This is in agreement with the data shown in Fig. 5.13c, which demonstrates a notable increase in control effectiveness at 6 degree angle of attack for the blunt nosetip cases at both 10 and 20 degree wing deflection, with the 20 degree wing deflection demonstrating the greatest magnitude of increase.

5.5.4 Wing shape change

This section presents comparisons of the effect of leading and trailing edge burnthrough on control effectiveness at zero degree angle of attack with a blunt nosetip. Similar to the blunt leading edge of the shape change wings, the choice of blunt nosetip was motivated by the expected vehicle shape change over the course of the trajectory and when burnthrough is most likely to occur - that is, at a trajectory point where the nosetip has already begun to recess.

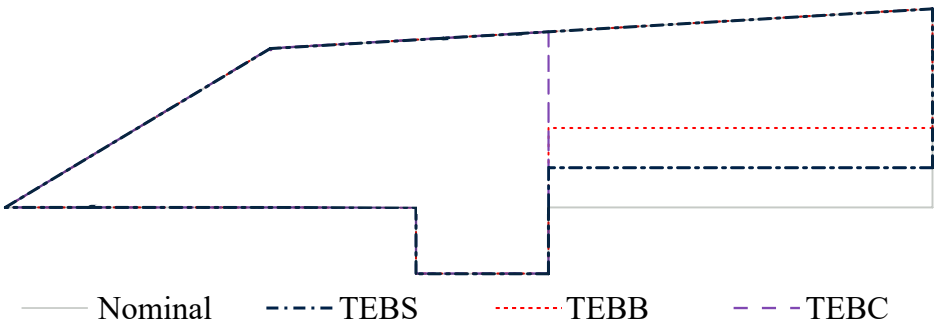

Fig. 5.14 Diagrams of the shape changed wings

Fig. 5.15 presents a comparison of the control effectiveness with varying degrees of trailing edge burnout. Unsurprisingly, the control effectiveness in all cases decreases with reducing wing area. In order to assess this relationship, Fig. 5.16 presents control effectiveness against wing area, both normalised by the blunt wing, with the dashed grey

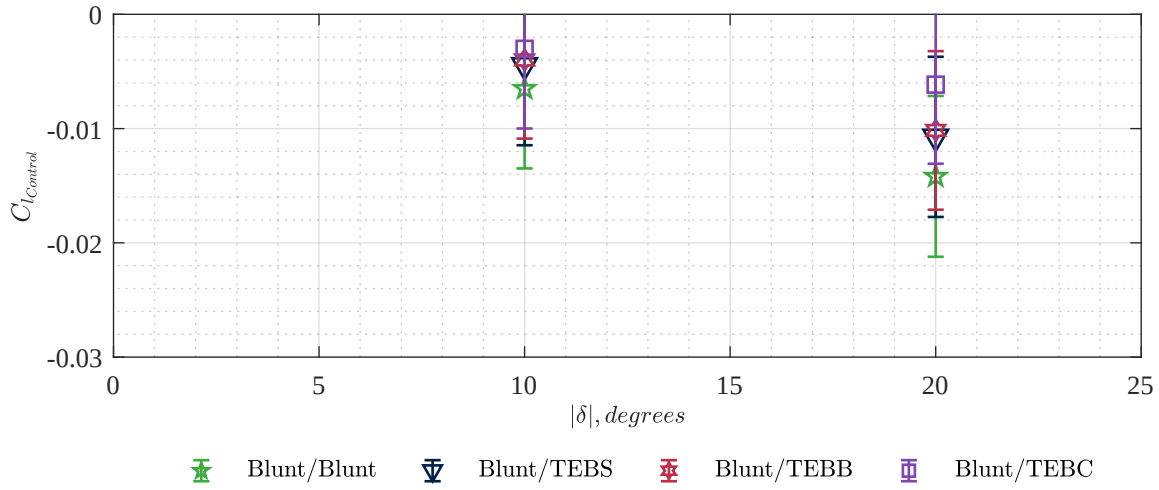

Fig. 5.15 Control Moment from tests varying the amount of trailing edge burnthrough

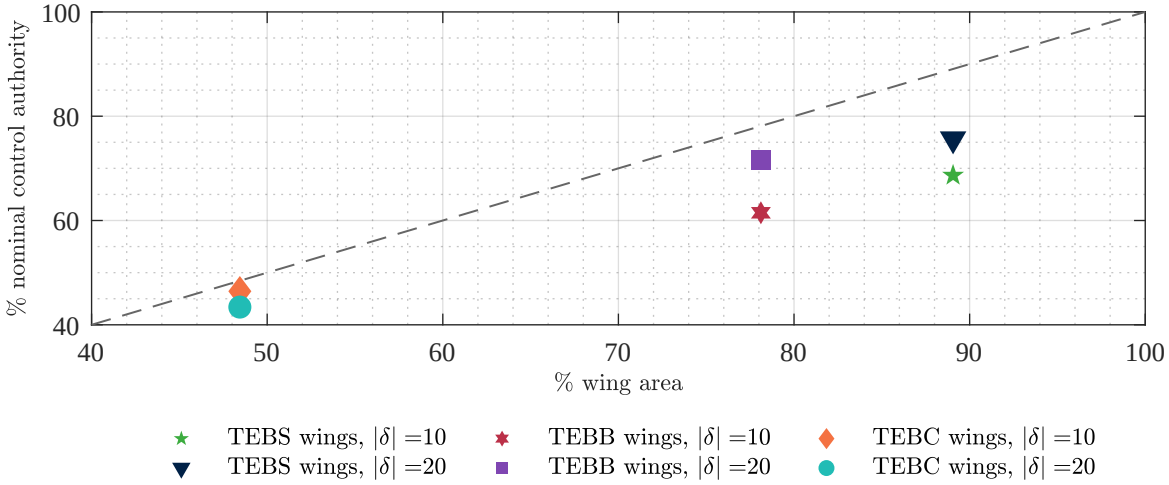

Fig. 5.16 Influence of wing area on the control effectiveness for the trailing edge burnthrough variations. The grey line presents the expected control moment if it were directly proportional to wing area

line indicating expected control effectiveness if it were simply proportional to wing area. It can be seen that in all cases, the measured control effectiveness lies beneath this line, with the TEBS wings exhibiting the greatest reduction in control authority per unit area removed. From the perspective of the total pressure distribution on the wing, there are two possible causes for deviations from the grey line: 1) Non-uniformity of total pressure distribution over the nominal wing, whereby the removed sections have an above average total pressure acting on them or 2) The removed section of wing exhibits a pressure relieving effect on the remaining wing - thereby reducing the total pressures acting on the remaining wing. Given that the portion of wing removed in the TEBS case is closest to the cone surface, within

the boundary layer and consequently unlikely to have an above average total pressure, it is most likely dominated by the latter effect. However, noting the 3D nature of the gap flow and overall flowfield, further work investigating the relative strength of these phenomena - experimentally with optical techniques such as Pressure Sensitive Paint (PSP) and Planar Laser Induced Fluorescence (PLIF), or computationally with 3D CFD - would allow for more in depth insight into the mechanisms of control effectiveness reduction.

Fig. 5.18 presents control effectiveness and Fig. 5.19 presents normalised control effectiveness and wing area for the leading vs trailing edge removal. It can be seen that, despite having a smaller area removed, the trailing edge burnthrough exhibits a greater decrease in control effectiveness relative to the nominal case than the leading edge burnthrough. In fact, it can be seen from Fig. 5.19 that the LEBS case produces a greater control moment than would be expected if control moment were directly proportional to wing area. This indicates that the change in control effectiveness is dominated by the first mechanism discussed previously (non-uniformity of total pressure distribution) and indicates that the total pressure on the portion upstream of the hinge is lower than the average total pressure acting on the wing. This may be a consequence of an interaction with the expansion onto the cone flats or simply a result of the proximity to the curved section of the blunt wing shock. Again, further investigation with 3D CFD or optical techniques would allow the 3D flowfield to be assessed in more detail and the effect of burnthrough to be better understood.

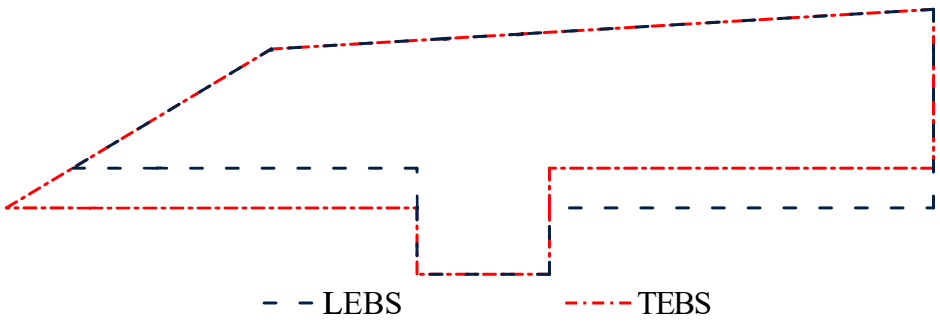

Fig. 5.17 Diagram comparing leading and trailing edge burnthrough

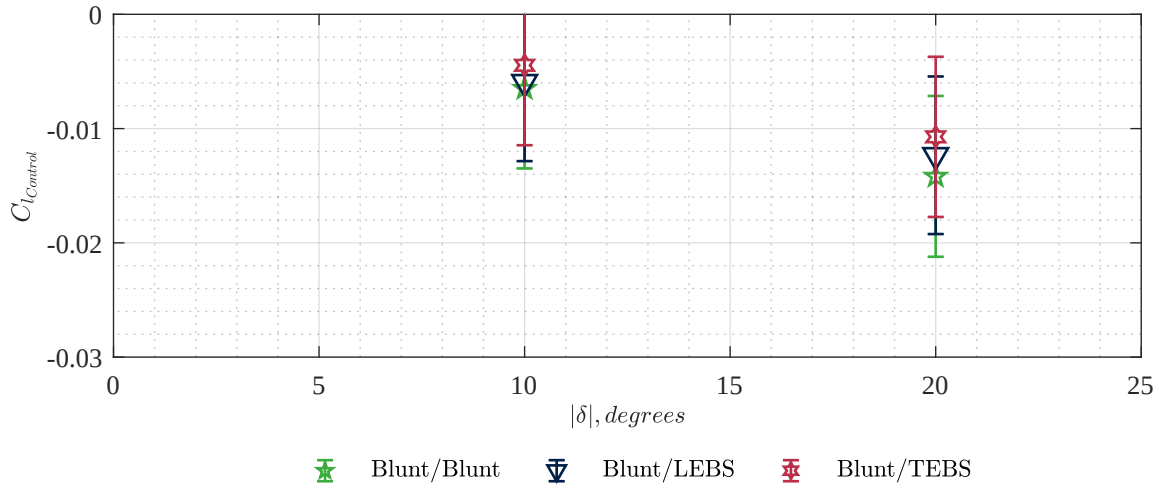

Fig. 5.18 Control Moment comparison between leading and trailing edge burnthrough

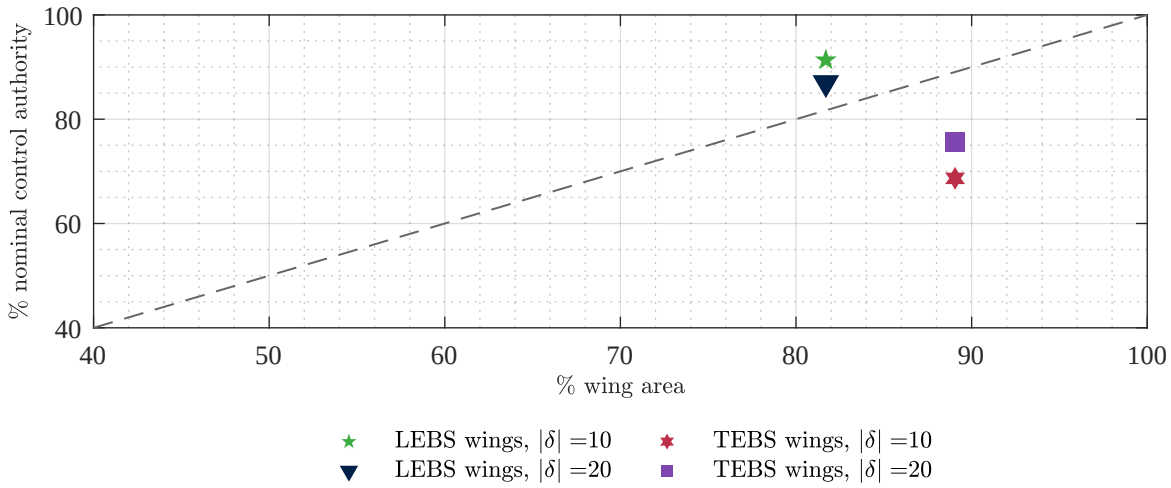

Fig. 5.19 Influence of wing area on the control effectiveness for the leading and trailing edge burnthrough variation. The grey line presents the expected control moment if it were directly proportional to wing area

5.6 Conclusions

This paper has presented experimental results investigating the effect of shape change on the roll control effectiveness provided by all moving wings on a 10 degree half angle cone in the Oxford High Density Tunnel. Two nosetips, with bluntness ratios of 1.67% and 17%, were tested, along with 6 variations of wing geometry. At zero degrees angle of attack, it was found that increased bluntness ratios decreases the control effectiveness provided by all moving wings, owing to the increased thickness of the low total pressure zone close to the cone surface. It was found that blunting of the leading edge of the all moving wing

also resulted in a reduction in control effectiveness, though this effect was negligible in comparison with the effect of nosetip blunting. Similar trends were shown at 6 degree angle of attack, though the reduction in control effectiveness resulting from leading edge blunting was reduced.

Of the 6 wing geometries, 4 all moving wing geometries were tested in conjunction with the 17% bluntness ratio nosetip, 3 simulating varying degrees of trailing edge burnthrough and another simulating the effect of leading edge burnthrough. For all of the trailing edge burnthrough cases, the control effectiveness was found to be lower than that expected if control moment were simply proportional to wing area. This was attributed to a pressure relieving effect as a consequence of adding burnthrough, whereby the total pressure distribution on the remaining wing is decreased relative to the total pressure on the non-damaged wing. In the case of leading edge burnthrough, the measured control effectiveness was greater than that expected if control effectiveness proportional to wing area, which was attributed to the total pressure distribution on the non-damaged wing, which may exhibit a region of low total pressure in the removed section as a consequence of its proximity to the curved shock produced by the blunt wing leading edge. Noting the 3D nature of the gap flow and overall flowfield, further work investigating the relative strength of these phenomena - experimentally with optical techniques such as Pressure Sensitive Paint (PSP) and Planar Laser Induced Fluorescence (PLIF), or computationally with 3D CFD - would allow for more in depth insight into the mechanisms of control effectiveness reduction for these geometries. Finally, any further experiments with this model in HDT should consider replacing the force balance used with a lower range/uncertainty sensor, as well as leverage the improvements in control effectiveness techniques demonstrated in Chapter 4 to increase both the quality and quantity of data attained.

5.7 Acknowledgements

This research was funded by DSTL. Thanks to Christopher Hambidge for operating HDT during these experiments and to Christopher Wheeler for setting up the Schlieren.

Statement of Authorship

Paper Title:

Effect of shape change on control effectiveness

Paper Status:

Unpublished and unsubmitted work written in manuscript style

Authors of the original paper:

Hillyer, J., Doherty, L.J., McGilvray, M.

Author contribution:

- **Hillyer, J.** : Lead author, conceptualisation, data curation, formal analysis, and writing.
- Doherty, L.J. : Supervision as Primary Supervisor.
- McGilvray, M. : Supervision as Principle Investigator.

Student Confirmation: **Date:** 13/01/2024

Supervisor Confirmation: **Date:** 13/01/2024

Chapter 6

Conclusion and Recommendations for Future Work

6.1 Conclusions and contributions

The research questions for this thesis were twofold: 1) how can control effectiveness studies be improved? and 2) how does shape change of the vehicle nosetip and all moving wings impact control effectiveness? This section reviews the presented work to demonstrate how these questions were answered.

The literature review in Chapter 2 identified that the biggest limitation of control effectiveness studies is the costs associated with ground testing, which imposes limitations in terms of the control effector resolution that can be characterised. This chapter proposed that the costs associated with control effectiveness studies could be reduced by improving the state-of-the-art for control effectiveness studies in Ludwieg tunnels, a cheaper alternative to the blowdown facilities typically used. The improvements identified as most significant were the ability to characterise multiple control effector deflections in a single run, and development of dynamic techniques to permit multiple attitudes to be characterised in a single test. Both of these improvements were dependent on the test time available in Ludwieg tunnels being increased.

Chapter 3 developed the theory behind and presented the commissioning of two blowdown modes in the Oxford High Density Tunnel (HDT): Extended Ludwieg Mode (ELM) and Plenum Augmented Ludwieg Mode (PALM). ELM is a quasi-steady blowdown mode, where steadiness of the facility supply condition is traded for test time. PALM is a steady blowdown mode, where the unit Reynolds number capability of the facility is traded for steady test times. ELM has been commissioned across the full range of HDT's current operating pressures,

whilst PALM has been demonstrated for 3 fill pressures: 14 bar, 30 bar and 55 bar. Test times in both modes were limited by facility unstart to at most 400 ms, greater than a factor of 10 improvement relative to Ludwieg Mode, though for the 14 and 30 bar PALM cases this came with a reduction of Unit Reynolds capability of 40% and 30%, respectively. The 55 bar PALM case demonstrated a test time of 160 ms for a 20% reduction in unit Reynolds number capability.

Chapter 4 presented work done to improve the state-of-the-art for control effectiveness studies in Ludwieg Tunnels. This was achieved using the extended test duration of the ELM to 1) investigate the effect of nozzle supply pressure rise time on natural frequency excitation and assess the suitability of a 6 Degree of Freedom Inertial Measurement Unit for acceleration compensation, 2) characterise multiple control effector deflections in a single test and 3) develop a free-to-roll model for continuous, low uncertainty, resolution of control effectiveness as a function of roll position. It is demonstrated that for Ludwieg Tunnels, addition of a plenum between the fast acting valve and the nozzle throat can reduce the magnitude of the startup loads models are subject to, and that the duration of the nozzle startup period, not the overall rise time of the facility nozzle supply trace, dictates which natural frequencies are excited. It is also demonstrated that 6 Degree of Freedom Inertial Measurement Unit's can be used for acceleration compensation, including use of differentiated gyroscope measurements for moment compensation. Excellent agreement was shown between tests performed with a constant wing deflection and those with multiple wing setpoints during the test. The free-to-roll technique leveraged the inherently low aerodynamic damping characteristic of hypersonic vehicles, in combination with low reduced angular rates, to provide a low uncertainty measurement of the static aerodynamics in isolation of dynamic phenomena. This technique was validated against force balance data at zero degrees angle of attack and has demonstrated the ability to characterise multiple roll positions in a single test at angle of attack.

Finally, Chapter 5 presented experimental results from testing of a 150 mm base diameter, 10 degree half angle cone with all moving wings in the Oxford High Density Tunnel, investigating the effect of shape change on control effectiveness. Two nosetips, with bluntness ratios of 1.7% and 17%, were tested, along with 6 variations of wing shape. At zero degrees angle of attack, it was found that increased nosetip bluntness ratio decreases the control effectiveness provided by all moving wings, owing to the increased region of influence of the entropy layer creating a low total pressure zone close to the cone surface. It was found that blunting of the leading edge of the all moving wing also resulted in a reduction in control effectiveness, though this effect was negligible in comparison with the effect of nosetip blunting. Similar trends were shown at 6 degree angle of attack, though the reduction in

control effectiveness resulting from leading edge blunting was reduced. The remaining 4 all moving wing geometries were tested in conjunction with the 17% bluntness ratio nosetip, 3 simulating varying degrees of trailing edge burnthrough and another simulating the effect of leading edge burnthrough. For all of the trailing edge burnthrough cases, the control effectiveness was found to be lower than that expected if control moment were simply proportional to wing area. This was attributed to a pressure relieving effect as a consequence of adding burnthrough, whereby the total pressure distribution on the remaining wing is decreased relative to the total pressure on the non-damaged wing. In the case of leading edge burnthrough, the measured control effectiveness was greater than that expected if control effectiveness proportional to wing area, which was attributed to the total pressure distribution on the non-damaged wing, which may exhibit a region of low total pressure in the removed section as a consequence of its proximity to the curved shock produced by the blunt wing leading edge.

6.1.1 Summary

To summarise, this thesis has:

- Commissioned two modes of operation for the Oxford High Density Tunnel - ELM and PALM - both proposed by Terry Jones [85] to provide blowdown operation. ELM has been implemented in the HDT and other similar facilities before, but this thesis presents the first time that PALM has been implemented in a Ludwieg Tunnel. Implementation of PALM allows for smaller-scale (length) facilities to potentially produce steady test times on par with or exceeding those available within large scale Ludwieg tunnels.

- Demonstrated that for force measurements in Ludwieg tunnels, it is the duration of nozzle startup period, not the overall rise time of the supply condition traces that serves to excite the natural frequencies of a force measurement system, and that addition of a plenum between the fast acting valve and the nozzle throat can reduce the magnitude of the startup loads imposed on the force balance.

- Demonstrated acceleration compensation of a Commercial-Off-The-Shelf force balance with a 6-axis MEMS IMU. Use of a MEMS IMU allows for increased flexibility in the packaging of accelerometers inside the experimental model. To the authors knowledge, this is the first time a MEMS IMU has been used for acceleration compensation.

- Performed control effectiveness measurements in a Ludwieg Tunnel with a deflection-pause methodology, allowing multiple control effector deflections to be characterised in a single run without contributions from dynamic aerodynamics.
- Developed the quasi-static technique - a technique for attaining continuous, low uncertainty, measurements of control effectiveness as a function of roll position. This technique was validated against acceleration compensated force balance measurements.
- Investigated the effect of changing nosetip bluntness on control authority, as well as the effect of varying degrees of leading and trailing edge root burnthrough of all moving wings.

6.2 Recommendations For Future Work

PALM

- Integration of PALM with the facility Programmable Logic Controller (PLC). For flexibility during mode commissioning, the PALM valves were open-loop controlled from the facility Data Acquisition system (DAQ). Integration with the facility PLC will enable closed loop control of plenum pressure, improving the repeatability and steadiness of the test flow.
- Modification of the facility plug valve:
  - Changes to the circumferential plug valve piston seals. The test condition achieved in PALM during this thesis were limited by the stiction provided by the circumferential seals on the plug valve piston. Investigation of lower stiction alternatives, such as spring energised seals, may improve the range of conditions able to be attained for a given fill condition. This should also improve the repeatability of both ELM and PALM.
  - If no suitable circumferential seals can be identified, a change in plug valve design to decouple the high pressure sealing from the area variation through the valve, such as that proposed in [105], will allow for more direct control of test condition and steadiness.
- Improvements to the vacuum infrastructure of HDT. As noted in Chapter 3, the test time attained in PALM is currently limited by the vacuum infrastructure of HDT. Improvements, such as increases to the dump tank volume, modification of the ducting

between the HDT test section and diffuser, and pressure rating of the dump tank and test section, will allow the full capability of PALM to be attained.

- Commissioning of lower Mach numbers. Though supplementary PALM data is given in Appendix A, demonstrating PALM at lower Mach numbers of 5 and 6, it is not fully commissioned at these Mach numbers. Naturally, commissioning of PALM at these lower Mach numbers will greatly expand the capability of HDT.

- Development of a single-shot total temperature probe. The fundamental assumption made with Aspirated Thermocouple processing [122, 123] is that total temperature is identical for shots performed at the same fill condition (fill pressure, fill temperature, Mach number, freestream gas), which, noting the dependency of the PALM trace to the stiction in the plug valve seals, as well as the dependency of total temperature to rate of plenum fill, may not be a valid assumption for PALM. Therefore, a total temperature probe that requires only a single shot, such as a probe based on differentially heated thin film heat transfer gauges [122, 142, 143], would be beneficial and give confidence in the calculated test conditions.

- Development of a static pressure probe. Another fundamental assumption used during all processing in this thesis is isentropic expansion through the facility nozzle. Use of a static pressure probe would allow this assumption to be validated/investigated.

Control Effectiveness Studies

- Improvements to actuators. Faster actuators, such as those developed by Van Hoffen [20], will allow for more control effector positions to be characterised in a single test.

- Development of gas bearings. In this study, the friction associated with steel bearings prevented the measurement of the roll damping coefficient. Gas bearings were commonly used in experiments in the 60's-90's, owing not only to their low friction, but also the insensitivity of friction to applied loads. Re-development of gas bearings for use in impulse facilities will allow not only for dynamic aerodynamic coefficients to be attained, but additionally for a reduction in the uncertainty of static coefficients attained using dynamic test techniques.

- Develop a methodology for determining the reaction moments resulting from actuator deflection. Knowledge of the reaction moments may allow for the static control effectiveness to be identified during periods of actuator motion.

- Extension of quasi-static technique to other degrees of freedom. In principle, the quasi-static technique should be able to be extended to the other rational degrees of freedom, though care must be taken with reduced angular rates to ensure that the dynamic effects are not influencing the measurement of static aerodynamics.
- Improvements to HDT traverse to allow motion during the test. Further improvements to force balance based control effectiveness studies can include implementing pitch-pause and yaw-pause methodologies. This will require the HDT traverse to be moveable during a test.

Shape change

- Whilst the experiments in Chapter 5 were able to measure changes in control effectiveness with blunting and wing shape change, the experimental techniques were not able to interrogate a 3D flowfield and so were of limited use in understanding the mechanisms behind the reduction in control effectiveness. Consequently, there are several recommendations for future experiments:
  - Use of a lower range force balance, with associated lower uncertainties, would allow for more confidence in the measurements of changes in control effectiveness
  - Unfortunately, the shape changed wings were obscured from the Schlieren field of view by the conical body. Future experiments should rotate the experimental model 45 degrees about the conical axis to allow Schlieren of the flowfield around the shape changed wings to be taken.
  - Use of further optical techniques, such as Pressure Sensitive Paint or Planar Laser Induced Fluorescence, would allow for the flowfield and resulting pressure distributions to be investigated further
- Use of fully viscous, 3D CFD would allow for the 3D flowfield to be further interrogated (once validated against the experimental data), and potentially offer more in depth insight into the various gap flow phenomena present.
- Increased permutations of shape change. Using the techniques developed in Chapter 4, further configurations of shape changed control effectors could be characterised. Of particular interest would be the effect of different roughness patterns, which could be applied to the model surface as well as the control effectors themselves.
- Pairing with a coupled trajectory-material solver. Coupled trajectory-material simulations allow for the shape change experienced by a vehicle over the course of a set

trajectory to be assessed. Ground testing of predicted shape-changed vehicles at discrete points on the trajectory would allow the vehicle performance and aerodynamics over the course of its trajectory to be predicted.

References

[1] Giuseppe Pezzella, Marco Marini, Marco Cicala, Antonio Vitale, Tobias Langener, and Johan Steelant. Aerodynamic characterization of hexafly scramjet propelled hypersonic vehicle. In *32nd AIAA Applied Aerodynamics Conference*, page 2844, 2014.

[2] Antonio Schettino, Giuseppe Pezzella, Marco Marini, Sara Di Benedetto, Victor F Villace, Johan Steelant, Rishabh Choudhury, Anatoly Gubanov, and Nina Voevodenko. Aerodynamic database of the hexafly-int hypersonic glider. *CEAS Space Journal*, 12:295–311, 2020.

[3] Charles E Cockrell Jr, Aaron H Auslender, Jeffrey A White, and Arthur D Dilley. Aeroheating predictions for the x-43 cowl-closed configuration at mach 7 and 10. In *40th AIAA Aerospace Sciences Conference and Exhibit*, number AIAA Paper 2002-0218, 2002.

[4] Charles Cockrell, Jr, Walter Engelund, Arthur Dilley, Robert Bittner, Tom Jentink, and Abdelkader Frendi. Integrated aero-propulsive cfd methodology for the hyper-x flight experiment. In *18th Applied Aerodynamics Conference*, page 4010, 2000.

[5] Brian R Hollis, Thomas J Horvath, Scott A Berry, H Harris Hamilton, Richard A Thompson, and Stephen J Alter. X-33 computational aeroheating predictions and comparisons with experimental data. *Journal of Spacecraft and Rockets*, 38(5):658–669, 2001.

[6] Scott D Holland, William C Woods, and Walter C Engelund. Hyper-x research vehicle experimental aerodynamics test program overview. *Journal of spacecraft and rockets*, 38(6):828–835, 2001.

[7] Kelly J Murphy, Robert J Nowak, Richard A Thompson, Brian R Hollis, and Ramadas Prabhu. X-33 hypersonic aerodynamic characteristics. *Journal of Spacecraft and Rockets*, 38(5):670–683, 2001.

[8] Patrick Gruhn and Ali Gülhan. Aerodynamic measurements of an air-breathing hypersonic vehicle at mach 3.5 to 8. *AIAA Journal*, 56(11):4282–4296, 2018.

[9] Eugene A Morelli. Flight-test experiment design for characterizing stability and control of hypersonic vehicles. *Journal of Guidance, Control, and Dynamics*, 32(3):949–959, 2009.

[10] Eugene A Morelli. Flight test maneuvers for efficient aerodynamic modeling. *Journal of aircraft*, 49(6):1857–1867, 2012.

[11] Eugene Morelli, Stephen Derry, and Mark Smith. Aerodynamic parameter estimation for the x-43a (hyper-x) from flight data. In *AIAA atmospheric flight mechanics conference and exhibit*, page 5921, 2005.

[12] RJ Stalker. Modern developments in hypersonic wind tunnels. *The Aeronautical Journal*, 110(1103):21–39, 2006.

[13] Sangdi Gu and Herbert Olivier. Capabilities and limitations of existing hypersonic facilities. *Progress in Aerospace Sciences*, 113:100607, 2020.

[14] Thino Eggers, Andreas Stamminger, Marcus Hörschgen, Wolfgang Jung, and John Turner. The hypersonic experiment shefex-aerotheromdynamic layout, vehicle development and first flight results. In *Proceedings 6th International Launcher Symposium on Launcher Technologies*, 2005.

[15] William L Oberkampf and Daniel P Aeschliman. Joint computational/experimental aerodynamics research on a hypersonic vehicle. i-experimental results. *AIAA journal*, 30(8):2000–2009, 1992.

[16] Ozer Igra and Friedrich Seiler. *Experimental methods of shock wave research*, volume 478. Springer, 2016.

[17] Dhanvada M Rao. *Hypersonic control effectiveness studies on delta wings with trailing-edge flaps*. PhD thesis, University of London, 1970.

[18] Dhanvada M Rao. Hypersonic incipient separation on delta wing with trailing-edge flap. *AIAA Journal*, 13(10):1386–1388, 1975.

[19] K Kontis. Flow control effectiveness of jets, strakes, and flares at hypersonic speeds. *Proceedings of the Institution of Mechanical Engineers, Part G: Journal of Aerospace Engineering*, 222(5):585–603, 2008.

[20] Morgan van Hoffen, David Buttsworth, and Ingo Jahn. Dynamic wind tunnel testing of an actuated canard-controlled hypersonic model. In *AIAA SCITECH 2024 Forum*, pages 2888–c1, 2024.

[21] AM Hyslop. *Force measurement techniques in short duration hypersonic facilities*. PhD thesis, University of Oxford, 2023.

[22] David R Buttsworth, Nathan Stern, and Rishabh Choudhury. A demonstration of hypersonic pitching control in the tusq hypersonic wind tunnel. In *55th AIAA Aerospace Sciences Meeting*, page 0261, 2017.

[23] Chester H Wolowicz, JS Brown Jr, and William P Gilbert. Similitude requirements and scaling relationships as applied to model testing. Technical report, 1979.

[24] Bruce Owens, Jay Brandon, Mark Croom, Mike Fremaux, Gene Heim, and Dan Vicroy. Overview of dynamic test techniques for flight dynamics research at nasa larc. In *25th AIAA aerodynamic measurement technology and ground testing conference*, page 3146, 2006.

[25] Leonard Bernstein and Ronald Charles Pankhurst. Force measurements in short duration hypersonic facilities. 1975.

[26] Daniel Simmons, William D Gothard, Nicholas J Molinaro, and Ryan J Meritt. Wind tunnel balance development for ludwieg tube facilities. In *AIAA AVIATION FORUM AND ASCEND 2024*, page 4285, 2024.

[27] C Jessen and H Grönig. A six component balance for short duration hypersonic facilities. In *New trends in Instrumentation for hypersonic research*, pages 295–305. Springer, 1993.

[28] V Storkmann, H Olivier, and H Gronig. Force measurements in hypersonic impulse facilities. *AIAA journal*, 36(3):342–348, 1998.

[29] KA Juhany and A Darji. Force measurement in a ludwieg tube tunnel. *Journal of Spacecraft and Rockets*, 44(1):88–93, 2007.

[30] LIU Yunfeng, WANG Yunpeng, YUAN Chaokai, LUO Changtong, and Zonglin Jiang. Aerodynamic force and moment measurement of 10 half-angle cone in jf12 shock tunnel. *Chinese Journal of Aeronautics*, 30(3):983–987, 2017.

[31] James F Martin and Leroy M Stevenson. *Instrumentation for force and pressure measurements in a hypersonic shock tunnel*. Number 113. Cornell Aeronautical Laboratory, Incorporated, 1962.

[32] Eric C Marineau. Force measurements in hypervelocity flows with an acceleration compensated piezoelectric balance. *Journal of spacecraft and rockets*, 48(4):697–700, 2011.

[33] Eric C Marineau, Matthew MacLean, Erik P Mundy, and Michael S Holden. Force measurements in hypervelocity flows with an acceleration compensated strain gage balance. *Journal of Spacecraft and Rockets*, 49(3):474–482, 2012.

[34] Gregory Smolinski. Proof of concept for testing acceleration compensation force balance techniques in short duration flows with a cev capsule. In *45th AIAA Aerospace Sciences Meeting and Exhibit*, page 1010, 2007.

[35] Dibesh Joshi, Pravin Vadassery, and Frank Lu. Acceleration compensation for force measurements in hypersonic shock tunnel. In *51st AIAA aerospace sciences meeting including the new horizons forum and aerospace exposition*, page 1020, 2013.

[36] George R Duryea and James F Martin. An improved piezoelectric balance for aerodynamic force. *IEEE Transactions on Aerospace and Electronic Systems*, (3):351–359, 1968.

[37] Hideyuki Tanno, Katsuhiro Itoh, Tomoyuki Komuro, Kazuo Sato, and Syuichi Ueda. Design and evaluation of strain gauge force balance with short test duration. *Transactions of the Japan Society for Aeronautical and Space Sciences*, 48(159):1–6, 2005.

[38] John W Draper, Greg Brauckmann, Franklin D Turbeville, and Sung Lee. Dynamic force reconstruction of transient flap control force experiments in a hypersonic wind tunnel. In *AIAA SCITECH 2024 Forum*, page 2661, 2024.

[39] SR Sanderson and JM Simmons. Drag balance for hypervelocity impulse facilities. *AIAA journal*, 29(12):2185–2191, 1991.

[40] David John Mee. Dynamic calibration of force balances for impulse hypersonic facilities. *Shock Waves*, 12:443–455, 2003.

[41] Luke J Doherty, Michael K Smart, and David Mee. Measurement of three-components of force on an airframe integrated scramjet at mach 10. In *20th AIAA International Space Planes and Hypersonic Systems and Technologies Conference*, page 3523, 2015.

[42] Daniel R Smith, David E Gildfind, David J Mee, Christopher M James, and Barry V Allsop. Magnetohydrodynamic drag force measurements in an expansion tunnel using a stress wave force balance. *Experiments in Fluids*, 61:1–15, 2020.

[43] Madhat M Abdel-Jawad, David J Mee, and Richard G Morgan. New calibration technique for multiple-component stress wave force balances. *Review of Scientific Instruments*, 78(6), 2007.

[44] M Abdel-Jawad, DJ Mee, RG Morgan, PA Jacobs, and JA Philpot. Transient force measurements at superorbital speeds. 2002.

[45] Luke James Doherty. An experimental investigation of an airframe integrated three-dimensional scramjet engine at a mach 10 flight condition. 2014.

[46] Otto Walchner, Frank M Sawyer, and Stephen J Koob. Dynamic stability testing in a mach-14 blowdown wind tunnel. *Journal of Spacecraft and Rockets*, 1(4):437–439, 1964.

[47] Kenneth F Stetson and Frank M Sawyer. Comparisons of aerodynamic data obtained by static and dynamic techniques. *AIAA Journal*, 17(1):103–105, 1979.

[48] OTTO WALCHNER. Laminar hypersonic roll damping derivatives for a 10 deg cone. *AIAA Journal*, 7(2):342–343, 1969.

[49] BRIAN QUINN. Blunt-cone roll-damping derivative. *AIAA Journal*, 7(1):175–177, 1969.

[50] FJ Regan and MV Krumins. Hypersonic dynamic testing of ablating models with three-degree-of-freedom gas bearings. *Journal of Spacecraft and Rockets*, 20(5):470–476, 1983.

[51] Andrew Hyslop, Luke J Doherty, Matthew McGilvray, Andrew Neely, Liam P McQuellin, James Barth, and Gerrie Mullen. Free-flight aerodynamic testing of the skylon space plane. *Journal of Spacecraft and Rockets*, 58(5):1487–1497, 2021.

[52] Andrew M Hyslop, Matthew McGilvray, and Luke J Doherty. Free-flight aerodynamic testing of a 7 degree half-angle cone. In *AIAA SCITECH 2022 Forum*, page 1324, 2022.

[53] Andrew Hyslop, Luke J Doherty, and Matthew McGilvray. Comparison of force measurement techniques in a short duration hypersonic facility. *Experiments in Fluids*, 65(2):21, 2024.

[54] Damian Friedl, J Martinez Schramm, and Klaus Hannemann. Measurements by means of optical tracking in the high enthalpy shock tunnel göttingen, heg. In *8th European Symposium on Aerothermodynamics for Space Vehicles*, pages 1–7, 2015.

[55] Klaus Hannemann, Jan Martinez Schramm, Sebastian Karl, and Stuart J Laurence. Free flight testing of a scramjet engine in a large scale shock tunnel. In *20th AIAA International Space Planes and Hypersonic Systems and Technologies Conference*, page 3608, 2015.

[56] Klaus Hannemann, Jan Martinez Schramm, Sebastian Karl, and Stuart J Laurence. Enhancement of free flight force measurement technique for scramjet engine shock tunnel testing. In *21st AIAA International Space Planes and Hypersonics Technologies Conference*, page 2235, 2017.

[57] Chris Kennell, Andrew J Neely, David R Buttsworth, Rishabh Choudhury, and Murat Tahtali. Free flight testing in hypersonic flows: Hexafly-int eftv. In *54th AIAA aerospace sciences meeting*, page 1152, 2016.

[58] Chris Kennell, Andrew J Neely, Sean B O'Byrne, and David Buttsworth. Measurement of vehicle stability coefficients in hypersonic wind tunnels. In *20th AIAA International Space Planes and Hypersonic Systems and Technologies Conference*, page 3690, 2015.

[59] Chris Kennell, Bodo Reimann, Rishabh Choudhury, David Buttsworth, and Andrew Neely. Subscale hypersonic free flight dynamics of hexafly-int eftv+ esm (multibody separation). In *7th European conference for aeronautics and space science*, 2017.

[60] Liam P McQuellin, Christopher M Kennell, Joni M Sytsma, Rishabh Choudhury, Andrew Neely, David R Buttsworth, and Todd Silvester. Investigating endo-atmospheric separation of a hypersonic flyer-sustainer using wind tunnel based free-flight. In *23rd AIAA International Space Planes and Hypersonic Systems and Technologies Conference*, 2020.

[61] Liam P McQuellin, Andrew Neely, and Gaetano Currao. Considerations for a hypersonic flight test investigating fluid-thermal-structural interactions. In *23rd AIAA International Space Planes and Hypersonic Systems and Technologies Conference*, 2020.

[62] Dániel Gábor Kovács. Experimental investigation of space debris separation in cold hypersonic flow using a free-flight measurement technique. 2024.

[63] Dániel G Kovács, Guillaume Grossir, Grigorios Dimitriadis, and Olivier Chazot. Six degrees of freedom free-flight measurement in the vki longshot wind tunnel. In *AIAA AVIATION 2023 Forum*, page 3535, 2023.

[64] Dániel Gábor Kovács, Guillaume Grossir, Grigorios Dimitriadis, and Olivier Chazot. Free-flight testing of proximal spheres and cubes in mach 14 hypersonic flow. In *Aerospace Europe Conference 2023 (EUCASS)*. EUCASS-CEAS, Brussels, Belgium, 2023.

[65] Stuart Jon Laurence, CS Butler, J Martinez Schramm, and K Hannemann. Force and moment measurements on a free-flying capsule in a shock tunnel. *Journal of Spacecraft and Rockets*, 55(2):403–414, 2018.

[66] Travis Duchene and Stuart Laurence. The aerodynamics of free-flying cylinders in high supersonic flow. In *AIAA AVIATION FORUM AND ASCEND 2024*, page 3923, 2024.

[67] Marie Tanno and Hideyuki Tanno. Aerodynamic characteristics of a free-flight scramjet vehicle in shock tunnel. *Experiments in Fluids*, 62(7):150, 2021.

[68] Hideyuki Tanno, Tomoyuki Komuro, Kazuo Sato, Katsuhiro Itoh, Masahiro Takahashi, Kazuhisa Fujita, Stuart Laurence, and Klaus Hannemann. Free-flight force measurement technique in shock tunnel. In *50th AIAA Aerospace Sciences Meeting including the New Horizons Forum and Aerospace Exposition*, page 1241, 2012.

[69] H Tanno, T Komuro, K Sato, K Fujita, and SJ Laurence. Free-flight measurement technique in the free-piston high-enthalpy shock tunnel. *Review of scientific instruments*, 85(4), 2014.

[70] Mary McWherter Walker and William L Oberkampf. Joint computational/experimental aerodynamics research on hypersonicvehicle. ii-computational results. *AIAA journal*, 30(8):2010–2016, 1992.

[71] Louis G Kaufman, L Meckler, and SA Hartofilis. An investigation of flow separation and aerodynamic controls at hypersonic speeds. *Journal of Aircraft*, 3(6):555–561, 1966.

[72] M Leroy Spearman and Dorothy O Braswell. An experimental and theoretical study of the aerodynamic characteristics of some generic missile concepts at mach numbers from 2 to 6.8. Technical report, 1994.

[73] RE Wilson. Laminar boundary-layer growth on slightly blunted cones at hypersonic speeds. *Journal of Spacecraft and Rockets*, 2(4):490–496, 1965.

[74] Clifton H Mortensen. Toward an understanding of supersonic modes in boundary-layer transition for hypersonic flow over blunt cones. *Journal of Fluid Mechanics*, 846:789–814, 2018.

[75] Matthew W Tufts and Roger L Kimmel. Analysis of windward side hypersonic boundary layer transition on blunted cones at angle of attack. In *55th AIAA Aerospace Sciences Meeting*, page 0764, 2017.

[76] K Stetson. Nosetip bluntness effects on cone frustum boundary layer transition in hypersonic flow. In *16th Fluid and Plasmadynamics Conference*, page 1763, 1983.

[77] K Stetson. Effect of bluntness and angle of attack on boundary layer transition on cones and biconic configurations. In *17th aerospace sciences meeting*, page 269, 1979.

[78] Joseph S Jewell and Roger L Kimmel. Boundary-layer stability analysis for stetsons mach 6 blunt-cone experiments. *Journal of Spacecraft and Rockets*, 54(1):258–265, 2017.

[79] Andrew Ceruzzi, Laurent M Le Page, Philipp Kerth, Benjamin A Williams, and Matthew McGilvray. Simultaneous measurements of freestream disturbances, boundary layer instabilities, and transition location on sharp and blunt cones in hypersonic flow. In *AIAA SCITECH 2024 Forum*, page 2187, 2024.

[80] Lars Eric Ericsson and J PETER REDING. Ablation effects on vehicle dynamics. *Journal of Spacecraft and Rockets*, 3(10):1476–1483, 1966.

[81] S CHANG. Effects of ablation on hypersonic aerodynamic stability characteristics. In *3rd and 4th Aerospace Sciences Meeting*, page 410, 1966.

[82] Michael S Holden. Experimental studies to examine the effects of surface roughness and blowing on sharp and blunt hypersonic vehicles. In *20th AIAA International Space Planes and Hypersonic Systems and Technologies Conference*, page 3600, 2015.

[83] Hubert Ludwieg. Tube wind tunnel: A special type of blowdown tunnel: Report presented at the 11th meeting of the wind tunnel and model testing panel, scheveningen, holland, 8-12 july 1957. AGARD, 1957.

[84] Jack Hillyer, Luke Doherty, Chris Hambidge, and Matthew McGilvray. Extension of test time in ludwieg tunnels. 2022.

[85] TV Jones, P Street, and M Westby. Recent enhancements to the dra shock tunnel. *Wind tunnels and wind tunnel test techniques*, page 30, 1992.

[86] Jeremy Moran, David R Buttsworth, and Lachlan Noller. Mach 6 and mach 7 conditions in tusq at reynolds numbers up to 30 million. In *AIAA AVIATION FORUM AND ASCEND 2024*, page 4197, 2024.

[87] Erik M Hoberg and Thomas J Juliano. Freestream characterization and condensation detection in the afosr–notre dame large mach-6 quiet tunnel. In *AIAA SCITECH 2023 Forum*, page 1458, 2023.

[88] Roger L Kimmel, Matthew P Borg, Joseph S Jewell, KIng-Yiu Lam, Rodney D Bowersox, Ravi Srinivasan, Steven Fuchs, and Thomas Mooney. Afrl ludwieg tube initial performance. In *55th AIAA Aerospace Sciences Meeting*, page 0102, 2017.

[89] Steven P Schneider and Christine E Haven. Quiet-flow ludwieg tube for high-speed transition research. *AIAA journal*, 33(4):688–693, 1995.

[90] Bryan Eric Schmidt. *On the stability of supersonic boundary layers with injection*. PhD thesis, California Institute of Technology, 2016.

[91] RA East and A Qasrawl. Long stroke isentropic free piston hypersonic wind tunnel. 1978.

[92] Zhiyuan Li, Youde Xiong, Xianxu Yuan, Jianqiang Chen, Jiaquan Zhao, and Jie Wu. A-variant design of hypersonic ludwieg tube wind tunnel. *AIAA Journal*, 60(7):3990–4005, 2022.

[93] Malte Estorf, Torsten Wolf, and Rolf Radespiel. Experimental and numerical investigations on the operation of the hypersonic ludwieg tube braunschweig. In *Fifth European Symposium on Aerothermodynamics for Space Vehicles*, volume 563, page 579, 2005.

[94] Ferry FJ Schrijer and Willem J Bannink. Description and flow assessment of the delft hypersonic ludwieg tube. *Journal of Spacecraft and Rockets*, 47(1):125–133, 2010.

[95] Young Ju Kim, Yung Hwan Byun, Soo Hyung Park, Gisu Park, and Jongkook Lee. Concept design of ludwieg tube at konkuk university. *Journal of the Korean Society for Aeronautical & Space Sciences*, 46(9):703–711, 2018.

[96] Aaron T Dufrene, Matthew G MacLean, Zakery R Carr, Ronald A Parker, and Michael S Holden. Scaled rocket testing in hypersonic flow. In *20th AIAA International Space Planes and Hypersonic Systems and Technologies Conference*, page 3550, 2015.

[97] Erich Schülein. Optical skin friction measurements in short-duration facilities. In *24th AIAA Aerodynamic Measurement Technology and Ground Testing Conference*, page 2115, 2004.

[98] Kyle P Bearden, Victor E Padilla, Lutz Taubert, and Stuart A Craig. Calibration and performance characterization of a mach 5 ludwieg tube. *Review of Scientific Instruments*, 93(8), 2022.

[99] Antonio Giovanni Schoneich and Stuart J Laurence. Development of a supersonic ludwieg-tube facility for investigating high-speed multi-phase flows. In *AIAA SCITECH 2024 Forum*, page 2756, 2024.

[100] Samuel A Maszkiewicz, Ryan S de Silva, Rowan Quintero, Stuart Laurence, and Michael Smith. Flow characterization of a newly commissioned high-temperature ludwieg tube at the university of maryland. In *AIAA AVIATION FORUM AND ASCEND 2024*, page 4199, 2024.

[101] Sebastien Wylie, Luke Doherty, and Matthew McGilvray. Commissioning of the oxford high density tunnel (hdt) for boundary layer instability measurements at mach 7. In *2018 Fluid Dynamics Conference*, page 3074, 2018.

[102] Phillip A Kreth, Mark Gragston, Kirk Davenport, and John D Schmisseur. Design and initial characterization of the utsi mach 4 ludwieg tube. In *AIAA Scitech 2021 Forum*, page 0384, 2021.

[103] Mark Gragston, Kirk Davenport, Farhan Siddiqui, Nicholas Webber, Cary D Smith, Phillip A Kreth, and John D Schmisseur. Design and initial characterization of the utsi mach 7 ludwieg tube. In *AIAA SCITECH 2023 Forum*, page 1457, 2023.

[104] Eugene NA Hoffman, Elijah J LaLonde, Angelina Andrade, Ivana Chen, Hayden A Bilbo, and Christopher S Combs. Flow characterization of the utsa hypersonic ludwieg tube. *Aerospace*, 10(5):463, 2023.

[105] Phillip Swann, David Buttsworth, Ingo H Jahn, Robert Frith, Jeremy Moran, Alister Webb, and Lachlan Noller. Reconfiguring the tusq hypersonic facility for lower mach number. In *AIAA AVIATION FORUM AND ASCEND 2024*, page 4198, 2024.

[106] Jack Hillyer, Luke Doherty, Christopher Hambidge, and Matthew McGilvray. Enhancing the test time performance of ludwieg tunnels. In *AIAA SCITECH 2024 Forum*, page 2754, 2024.

[107] Steven P Schneider. Flight data for boundary-layer transition at hypersonic and supersonic speeds. *Journal of Spacecraft and Rockets*, 36(1):8–20, 1999.

[108] Shelly Ferlemann, Charles McClinton, Ken Rock, and Randy Voland. Hyper-x mach 7 scramjet design, ground test and flight results. In *AIAA/CIRA 13th International Space Planes and Hypersonics Systems and Technologies Conference*, page 3322, 2005.

[109] Timothy Wadhams, Matthew MacLean, Michael Holden, and Scott Barry. A review of transition studies on full-scale flight vehicles at duplicated flight conditions in the lens tunnels and comparisons with prediction methods and flight measurement. In *48th AIAA Aerospace Sciences Meeting Including the New Horizons Forum and Aerospace Exposition*, page 1246, 2010.

[110] C Cockre, A Auslender, J White, and A Dilley. Aeroheating predictions for the x-43 hyper-x cowl-closed configuration at mach 7 and 10. In *40th AIAA Aerospace Sciences Meeting & Exhibit*, page 218, 2002.

[111] Frank K Lu and Dan E Marren. Principles of hypersonic test facility development. *Progress in Astronautics and Aeronautics. Volume 198*, pages 17–27, 2002.

[112] WR Davies and L Bernstein. Heat transfer and transition to turbulence in the shock-induced boundary layer on a semi-infinite flat plate. *Journal of Fluid Mechanics*, 36(1):87–112, 1969.

[113] RA East, RJ Stalker, and JP Baird. Measurements of heat transfer to a flat plate in a dissociated high-enthalpy laminar air flow. *Journal of Fluid Mechanics*, 97(4):673–699, 1980.

[114] PA Jacobs, RC Rogers, EH Weidner, and RD Bittner. Flow establishment in a generic scramjet combustor. *Journal of Propulsion and Power*, 8(4):890–899, 1992.

[115] Hubert Ludwieg, Theo Hottner, and Helmut Grauer-Carstensen. Der rohrwindkanal der aerodynamischen versuchsanstalt goettingen the ludwig-tube wind tunnel of the gottingen aerodynamic facility. *Deutsche Forschungs-und Versuchsanstalt fuer Luft-und Raumfahrt EV, Brunswick, West Germany*, 1969.

[116] Aaron T Dufrene. Extension of lens shock tunnel test times and lower mach number capability. In *53rd AIAA Aerospace Sciences Meeting*, page 2017, 2015.

[117] Holger Friehmelt, Georg Koppenwallner, and Rudolf Mueller-Eigner. Calibration and first results of a redesigned ludwieg expansion tube. In *5th International Aerospace Planes and Hypersonics Technologies Conference*, page 5001, 1993.

[118] Jie Wu and Rolf Radespiel. Tandem nozzle supersonic wind tunnel design. *International Journal of Engineering Systems Modelling and Simulation 47*, 5(1-3):8–18, 2013.

[119] J Wu and R Radespiel. Experimental investigation of a newly designed supersonic wind tunnel. *Progress in Flight Physics–Volume 7*, 7:123–144, 2015.

[120] Jie Wu and Rolf Radespiel. Damping insert materials for settling chambers of supersonic wind tunnels. *Experiments in Fluids*, 58(3):19, 2017.

[121] Matthew McGilvray, Luke J Doherty, Andrew J Neely, Robert Pearce, and Peter Ireland. The oxford high density tunnel. In *20th AIAA International Space Planes and Hypersonic Systems and Technologies Conference*, page 3548, 2015.

[122] McGilvray M Hambidge C Herman T. and Buttsworth D. Total Temperature Measurements In the Oxford High Density Tunnel. *FAR Conference, Monopoli, Italy*, 2019.

[123] Agung Widodo and David Buttsworth. Stagnation temperature in a cold hypersonic flow produced by a light free piston compression facility. *Experiments in fluids*, 54:1–12, 2013.

[124] PA Jacobs. Quasi-one-dimensional modeling of a free-piston shock tunnel. *AIAA journal*, 32(1):137–145, 1994.

[125] Peter A Jacobs. Shock tube modelling with l1d. 1998.

[126] Peter L Collen, Luke Doherty, Matthew McGilvray, Imran Naved, Rowland T Penty Geraets, Tobias A Hermann, Richard G Morgan, and David Gildfind. Commissioning of the t6 stalker tunnel. In *AIAA Scitech 2019 Forum*, page 1941, 2019.

[127] Peter Collen, Luke J Doherty, Suria D Subiah, Tamara Sopek, Ingo Jahn, David Gildfind, Rowland Penty Geraets, Rowan Gollan, Christopher Hambidge, Richard Morgan, et al. Development and commissioning of the t6 stalker tunnel. *Experiments in Fluids*, 62(11):1–24, 2021.

[128] Andreas Andrianatos. Ground testing at superorbital flight conditions in a large scale expansion tube. 2020.

[129] Hugh W Coleman and W Glenn Steele. *Experimentation, validation, and uncertainty analysis for engineers*. John Wiley & Sons, 2018.

[130] Frederick G Keyes. A summary of viscosity and heat-conduction data for he, a, h2, o2, n2, co, co2, h2o, and air. *Transactions of the American Society of Mechanical Engineers*, 73(5):589–595, 1951.

[131] Equations NACA. Tables, and charts for compressible flow. *NACA Report*, 1135, 1953.

[132] Alexander Wagner, Erich Schülein, René Petervari, Klaus Hannemann, Syed RC Ali, Adriano Cerminara, and Neil D Sandham. Combined free-stream disturbance measurements and receptivity studies in hypersonic wind tunnels by means of a slender wedge probe and direct numerical simulation. *Journal of Fluid Mechanics*, 842:495–531, 2018.

[133] John Lafferty and Joseph Norris. Measurements of fluctuating pitot pressure," tunnel noise," in the aedc hypervelocity wind tunnel no. 9. In *2007 US Air Force T&E Days*, page 1678. 2007.

[134] Curtis Peebles. *Eleven seconds into the unknown: a history of the hyper-X program*. American Institute of Aeronautics and Astronautics, 2011.

[135] Arloe W Mayne. *Roll-damping Derivative Calculations for Spinning Sharp and Blunt Cones in Supersonic and Hypersonic Flow*, volume 78. Citeseer, 1979.

[136] DK Schmidt. Problems in control system design for hypersonic vehicles. In *Automatic Control in Aerospace 1992*, pages 89–96. Elsevier, 1993.

[137] Anshuman Pandey, Katya M Casper, Russell Spillers, Melissa Soehnel, and Seth Spitzer. Hypersonic shock wave-boundary-layer interaction on the control surface of a slender cone. In *AIAA SciTech 2020 Forum*, page 0815, 2020.

[138] Andrew Ceruzzi, Laurent Le Page, Liam P McQuellin, Wesley J Condren, and Matthew McGilvray. Observations of boundary layer transition reversal on a blunt cone in hypersonic flow. In *AIAA SCITECH 2025 Forum*, page 0921, 2025.

[139] J Cleary. Effects of angle of attack and nose bluntness on the hypersonic flowover cones. In *3rd and 4th Aerospace Sciences Meeting*, page 414, 1966.

[140] David C Steuer, Christopher Hambidge, and Matthew McGilvray. A method for direct shear measurement of large scale roughened surfaces in short duration hypersonic facilities. In *AIAA SCITECH 2023 Forum*, page 2442, 2023.

[141] SA Prince, M Vannahme, and JL Stollery. Experiments on the hypersonic turbulent shock-wave/boundary-layer interaction and the effects of surface roughness. *The Aeronautical Journal*, 109(1094):177–184, 2005.

[142] David Buttsworth and Timothy Buttsworth. Accurate transient heat flux from simple treatment of surface temperature distribution in the semi-infinite case. *arXiv preprint arXiv:2412.01362*, 2024.

[143] David R Buttsworth and Terry V Jones. High bandwidth stagnation temperature measurements in a mach 6 gun tunnel flow. *Experimental thermal and fluid science*, 27(2):177–186, 2003.

Appendix A

Supplementary PALM data

This appendix presents supplementary PALM data attained at Mach numbers of 5 and 6 to demonstrate the feasibility/operability of PALM for higher values of α_ϕ (0.9 and 0.4, respectively, compared to 0.2 for the Mach 7 nozzle).

Mach 5

Fig. A.1 presents Mach 5 LM, ELM and PALM data. The data in the left hand figure presents the implementation of PALM with fresh circumferential seals on the piston. The effect of seal friction is demonstrated well by the pseudo-ELM trace. At the end of the first plateau ($t \approx 0.08$ s), there is an initial sharp decrease in supply pressure, followed by a slower decrease. This indicates that, similar to the M7 ELM data presented in the mode-to-mode comparisons in Chapter 3, piston motion consists of an initial, sharp jolt back, before a slower remaining opening - a consequence of the stiction in the seals. Even with the slower remaining opening, it can be seen that there are short plateaus (e.g. $0.14 < t < 0.16$), which demonstrates that the overall plug opening was still too fast for ELM, resulting in HDT operating in Pseudo-ELM. It can also be seen from the left hand figure in Fig. A.1, that this stiction imposes limitations on the smoothness of the ELM trace.

The right hand figure of Fig. A.1 presents a comparison of LM and PALM, demonstrating, again, a significant increase in steady test time in PALM. It can be seen that the second stage motion of PALM was slightly too slow, resulting in a steady decrease in supply pressure, albeit at a much reduced rate relative to ELM. It can also be seen that there is a significant decease in the peak supply pressure attained in PALM relative to ELM. Though this could be a result of very small values of x_{wr}, it is felt more likely that this is a result of the flow choking at the upstream (plug valve) throat, and forcing a shock to form in the plenum and

resulting in a lower peak supply pressure. Pitot pressure measurements confirm that the nozzle has started as expected and Mach 5 flow was attained.

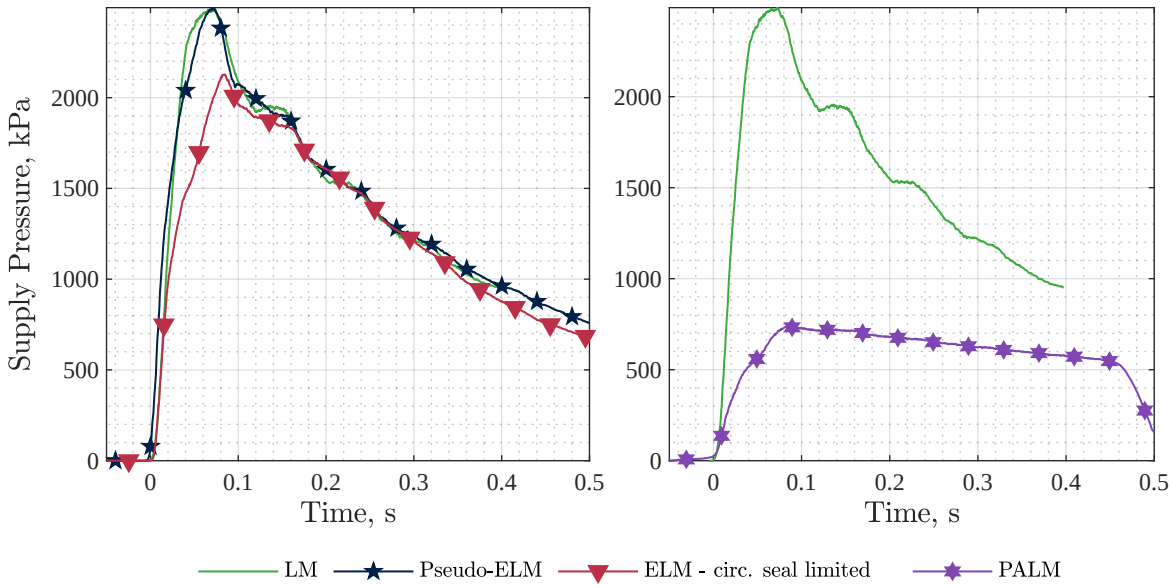

Fig. A.1 Left: Mach 5 ELM. Right: Mach 5 PALM. 3500 kPa, 500 K fill.

Mach 6

A comparison of LM and PALM at Mach 6 is presented in Fig. A.2. It can be seen that, as expected, operation in PALM produces a significantly extended test time at the expense of total pressure capability. Again, it can be seen that the second stage motion for PALM was too slow, as evidenced by the decreasing supply pressure.

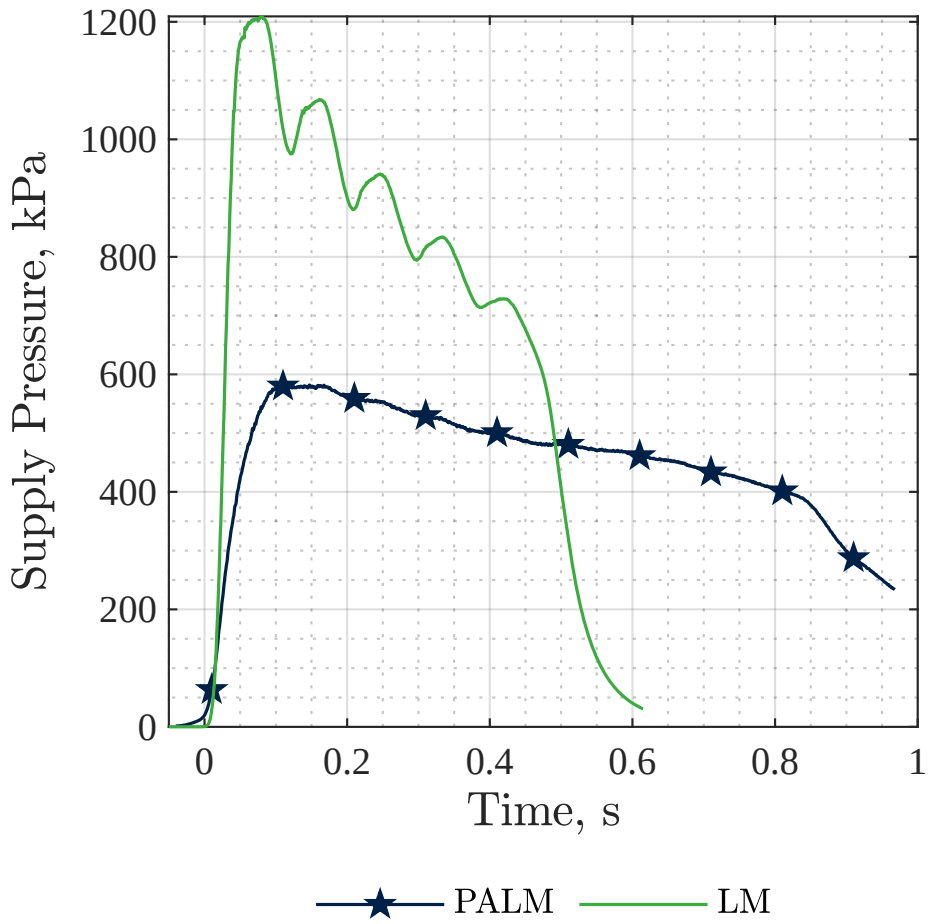

Fig. A.2 Mach 6 PALM, 1400 kPa, 500 K fill